MICROSCOPIC AND SPECTROSCOPIC STUDIES OF GROWTH AND ELECTRONIC STRUCTURE OF EPITAXIAL GRAPHENE

A Thesis
Presented to
The Academic Faculty

by

Nikhil Sharma

In Partial Fulfillment
of the Requirements for the Degree
Doctor of Philosophy in the
School of Physics

Georgia Institute of Technology
May 2009

MICROSCOPIC AND SPECTROSCOPIC STUDIES OF GROWTH AND ELECTRONIC STRUCTURE OF EPITAXIAL GRAPHENE

Approved by:

Dr. Phillip First, Advisor
School of Physics
Georgia Institute of Technology

Dr. Edward Conrad
School of Physics
Georgia Institute of Technology

Dr. Walter deHeer
School of Physics
Georgia Institute of Technology

Dr. Mei yin Chou
School of Physics
Georgia Institute of Technology

Dr. Thomas Orlando
School of Chemistry
Georgia Institute of Technology

Date Approved: March 9 2009

To my wife, Malika and my son, Shaurya

ACKNOWLEDGEMENTS

As I sit down to pen these acknowledgements, I have a sneaky suspicion that it will be an overrun like the speeches at Oscars but few and far between in the world are people as fortunate as me who genuinely have so many friends, family and guides to thank. For my Ph.D., undoubtedly the pillar of support, inspiration and encouragement throughout has been my wonderful advisor, Dr. Phillip N. First. Dr. First's amazing insights and clarity in the world of physics has been a bright, guiding light for me during this tedious but rewarding journey. It has been an honor to get an opportunity to work in his lab. Dr. First's boundless patience and impeccably-timed humor challenged me and uplifted me on numerous occasions, helping me persevere through difficult times continually learning as much as I did.

My sincere gratitude and appreciation are also definitely due, to Dr. Walt de Heer, a leader in Graphene research worldwide, who engineered the NPEG project. Also, due are thanks to Dr. Conrad for his perceptive input during the course of my Ph.D., as is my indebtedness to the Dr. Thomas Orlando and Dr. Mei Yin Chou for graciously accepting to be on my Thesis Committee. My memorable journey through this doctoral passage would have been stark and boring without the enthusiasm and intellectually charged atmosphere that the other guides like Dr. Claire Berger and my team members provided. Working at this lab enriched my life and expanded my horizons. Special thanks to Joanna Hass for being a fun lab-mate who was always game for another social outing with the team, to Greg Rutter for having the best English humor underneath that American disguise, to Lee Miller for his sheer brilliance and unmistakable passion for life and STM data acquisition software alike, to Kevin Kubista for showing me how simple deli sandwiches and delicious fishing stories can make up a wonderful life, and to Britt Torrance for his commitment and speed of learning which defies natural laws. And while not so recent, I would be remiss not thanking some former Ph.D. students like Sameh Dardona, a superb human and a brilliant scientist, Jianfei Shao, the most unassuming and generous fellow labmate and Tianbo Li for his work on STM. I can never ever forget the unflinching support of my dear friend, Se il Lee and stay indebted to him almost

equally for his good listening ear as I am for his kimchi that frequently spiced up my culinary life as a bachelor. Many thanks to Andrew Zangwill, an incredible Graduate Coordinator, without whom this Ph.D. would have been much more work and much less fun. I would also like to thank the students at Dr. deHeer's lab, especially Mike Sprinkle for stimulating discussions and furnace-grown Si-face samples, Xuebin Li, and Ming Ruan. I would like to thank Doogie at Dr Orlando's lab for his collaborative work on Raman measurements that progressed my doctoral work with more focus and data. Thanks to Sam for doing odd jobs happily in the machine shop and to Scott for his incredible support in electronics.

And long before this journey began, started my everlasting debt to my most loving and caring parents who have worked hard all their lives to provide me the best opportunities they could think of. I am also sincerely grateful to my parents-in-law for their continuing love and support, especially Papaji's belief in my ability to excel. I am also heavily indebted to my dear, dear grandma who nurtures me to this day as though I were the only first-born anywhere and to my beloved grandfather for being the first and foremost to believe in me. He taught me how to dream and his daughters, my loving aunts, my incredible brother, Vasant, my wonderful brother in-law Sunny, my Ram uncle and my dear cousins have helped me stay that course.

Last but not the least, I am sincerely thankful to my partner in everything, my wife, Malika who brings me strength, joy and unconditional love every day, ensuring that my life stays "full" of good food, good music and good company. With her and our adorable son Shaurya, in my life, this Ph.D. has a meaning beyond academics, beyond accomplishment.

Very sincerely,

Nikhil

TABLE OF CONTENTS

LIST OF TABLES

LIST OF FIGURES

ABBREVIATIONS

Abbreviation	Meaning
AES	Auger electron spectroscopy
ARPES	angle resolved photoemission spectroscopy
CNT	carbon nanotube
EG	epitaxial graphene
FEM	field emission microscopy
IR	infrared
KRIPES	k-resolved inverse photoemission spectroscopy
LDOS	local density of states
LEED	low energy electron diffraction
LT	low temperature
ML_e	monolayer equivalent
NIST	national institute of standards and technology
RF	radio frequency
RT	room temperature
STM	scanning tunneling microscopy
STS	scanning tunneling spectroscopy
TEM	transmission electron microscopy
TSP	titanium sublimation pump
UHV	ultra-high vacuum

SUMMARY

It is generally believed that the Si technology is going to hit a road block soon. Amongst all the potential candidates, graphene shows the most promise as replacement material for the aging Si technology. This has caused a tremendous stir in the scientific community. This excitement stems from the fact that graphene exhibits unique electronic properties. Physically, it is a two-dimensional network of sp_2 bonded carbon atoms. The unique symmetry of two equivalent sublattices gives rise to a linear energy dispersion for the charge carriers. As a consequence, the charge carriers behave like massless Dirac particles with a constant speed of *c/300*, where *c* is the speed of light. The sublattice symmetry gives rise to unique half-integer quantum hall effect, Klein's paradox, and weak antilocalization.

In this research work, I was able to successfully study the growth and electronic structure of EG on SiC(0001), in ultra-high vacuum and low-vacuum furnace environment. I used STM to study the growth at an atomic scale and macroscopic scale. With STM imaging, I studied the distinct properties of commonly observed interface region (layer 0), first graphene layer, and the second graphene layer. I was able to clearly resolve graphene lattice in both layer 1 and 2. High resolution imaging of the defects showed a unique scattering pattern. Raman spectroscopy measurements were done to resolve the layer dependent signatures of EG. The characteristic Raman 2D peak was found to be suppressed in layer 1, and a single Lorentzian was seen in layer 2. Ni metal islands were grown on EG by e-beam deposition. STM/ STS measurements were done to study the changes in doping and the electronic structure of EG with distance from the metal islands.

CHAPTER I

INTRODUCTION

Carbon is the sixth most abundant and perhaps the most remarkable element. It has an atomic number 8 ($1s^2 2s^2 2p^2$), and an atomic mass of 12 a.m.u. Carbon and its compounds play a major role in earth's ecosystem and sustain life forms. Carbon forms the backbone of organic chemistry due its ability to form infinite number of molecules, with equally diverse properties. Catenation is the ability of an element to form long chains because of strong covalent bonding. Carbon's catenating ability plays a key role in the field of polymer science. Carbon has a strong ability to form stable σ and π bonds with itself which is the primary reason for the diversity exhibited by its compounds. Catenation is also exhibited by other materials such as silicon. However, in Si catenation is exhibited to a limited extent, as it prefers not to form π bonds due to poor side-on overlap of the p orbitals.

Carbon catenates with three different kinds hybridization between the $2s$ and $2p$ orbitals. These are sp_3, sp_2 and sp with bond energies of 370, 680 and 890 KJ/mol respectively [59]. Amongst the three distinct flavors of hybridization, sp_2 hybridization is particularly interesting. In this hybridization, one electron in the fully filled *2s* orbital gets promoted to the *2p* orbital resulting in four half-filled orbitals. The half-filled *2s* and $2p$ orbitals combine to form three sp_2 hybridized orbitals and a non-hybridized delocalized p orbital. The three sp_2 orbitals have a trigonal planar geometry with a maximum angle of 120° between them (see Fig. 1.1(a)). The non-hybridized p orbital extends perpendicular to the plane and forms side-on covalent bond (π bond) with neighboring atoms (see Fig. 1.1(a) and (b)).

Graphene is a 2D hexagonal network of sp_2 bonded carbon atoms, and it has unique electronic and structural properties (see Sec. 1.2). Hexagonal symmetries are abundant in nature as shown in Fig. 1.1. Figure 1.1(c) shows the famous *Giant's Causeway* rock formation located in Ireland which is collection of hexagon shaped rocks stacked next to each other. Figure 1.1(d) shows hexagonal symmetry exhibited by snow flakes, which has been extensively studied by x-ray measurements. A

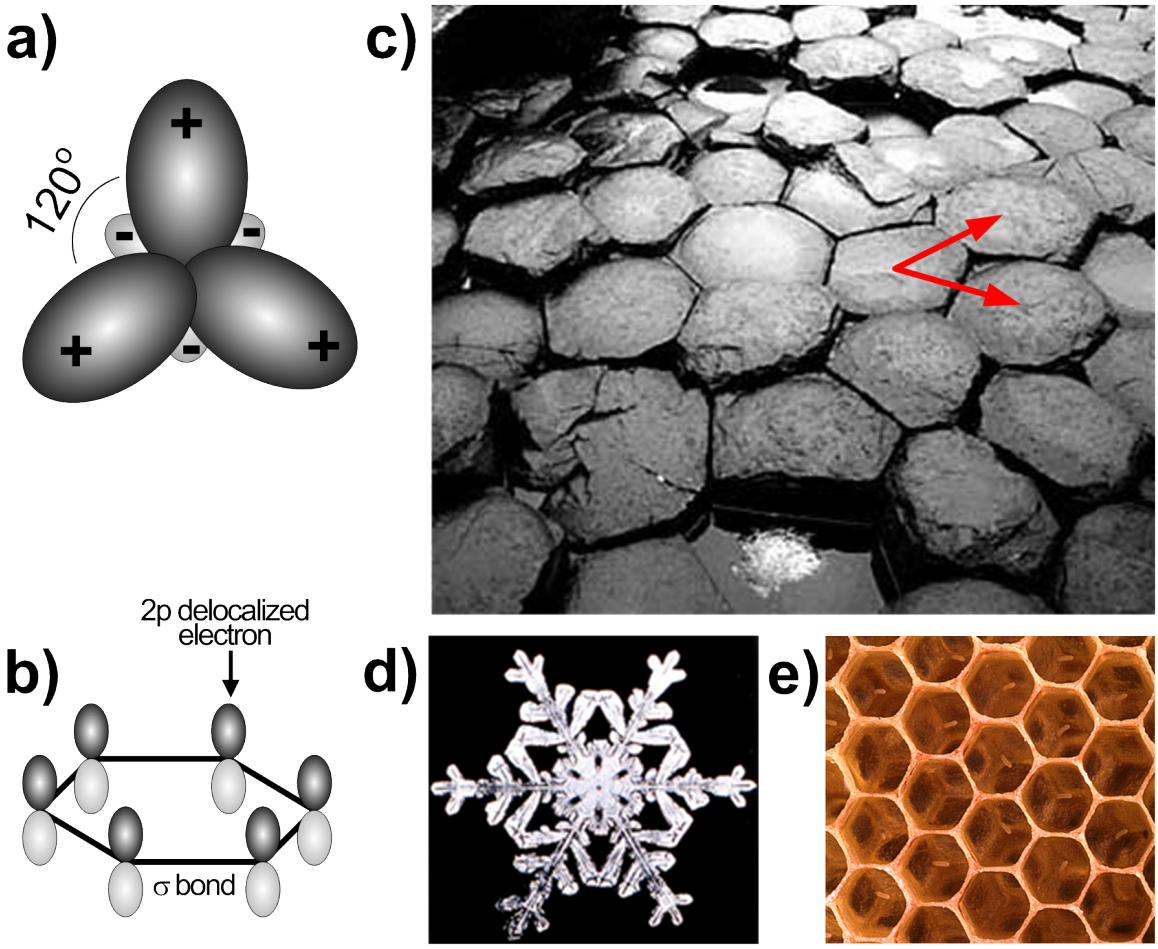

Figure 1.1: (a) Trigonal planar geometry of sp_2 hybridized orbitals involves one half-filled s and p two orbitals. The maximum angle between the orbitals is 120°. (b) Unhybridized half-filled p_z orbitals in a hexagon of C atoms. They are perpendicular to the plane and form side-on covalent bonds with other neighboring p_z orbitals. (c) *Giant's Causeway* rock formation in Ireland shows hexagonal shaped rocks. (d) Hexagonal symmetry is exhibited by snow flakes which has been verified by x-ray measurements. (e) Honeycomb network made by bees to store their supplies, also exhibits hexagonal symmetry.

honeycomb lattice constructed by bees to store their supplies also shows hexagonal symmetry which is closely related to the crystal structure of graphene. Theoretically, graphene is the most widely studied allotrope of carbon and it has in several instances served as a starting point for deriving electronic properties of other complicated materials [215].

Interestingly, graphene is popularly addressed as the "mother" of other graphitic forms [75, 76]. Other dimensionalities, fullerenes (0D), nanotubes (1D) and graphite (3D) can be derived from graphene by wrapping, rolling and stacking. Due to a strong in-plane sp_2 bonding, the graphene

fabric is probably one of the stiffest things known [121]. However, the coupling between neighboring planes is significantly weaker due to Van der Waal like interactions. Since its discovery [167], graphene has caused tremendous excitement in the scientific community and an unparalleled rush matched only by the buzz created by high temperature superconductors [24] and stem-cell research [22].

1.1 Need for a Better Material System

Semiconductor industry has done well since adapting to silicon as the main material for chip manufacturing. Moore's law has been remarkably successful since it was proposed 44 years ago [153]. According to Moore's law, number of transistors on a chip should double every two years. So far the results have been very promising, but it has been predicted that silicon technology is going to hit a road block soon.

There was a lot of excitement generated around carbon-based graphitic compounds two decades ago. At that time there was a lot of discussion about the future of carbon based science [58]. Amongst all the possible candidates, carbon nanotubes (CNT) has showed a lot of promise as a building block for ballistic electronic devices. CNTs are essentially a single sheet of graphene rolled up into a cylinder. The helicity (rolling direction) determines the electronic properties of CNTs. Both metallic and semiconducting (with varying bandgaps) [11, 42, 60] behavior can be realized with proper helicity. Semiconducting properties of CNTs are particularly useful for switching (transistor) applications. CNTs can be grown in single-walled (one graphene sheet) [145] or multiwalled configurations. Although, there are several promising reports of successful device fabrication [17, 46], CNTs is not a feasible option for mass scale production. CNTs suffer from unwieldy growth mechanisms, and unpredictable helicity during growth. Graphene on the other hand has a two-dimensional crystal structure, making it compatible with standard industry lithographic techniques.

1.2 Properties of Graphene

In this section, I will discuss some of the unique structural and electronic properties of graphene. These properties make graphene an extraordinary electronic material, and a potential candidate for the semiconductor industry.

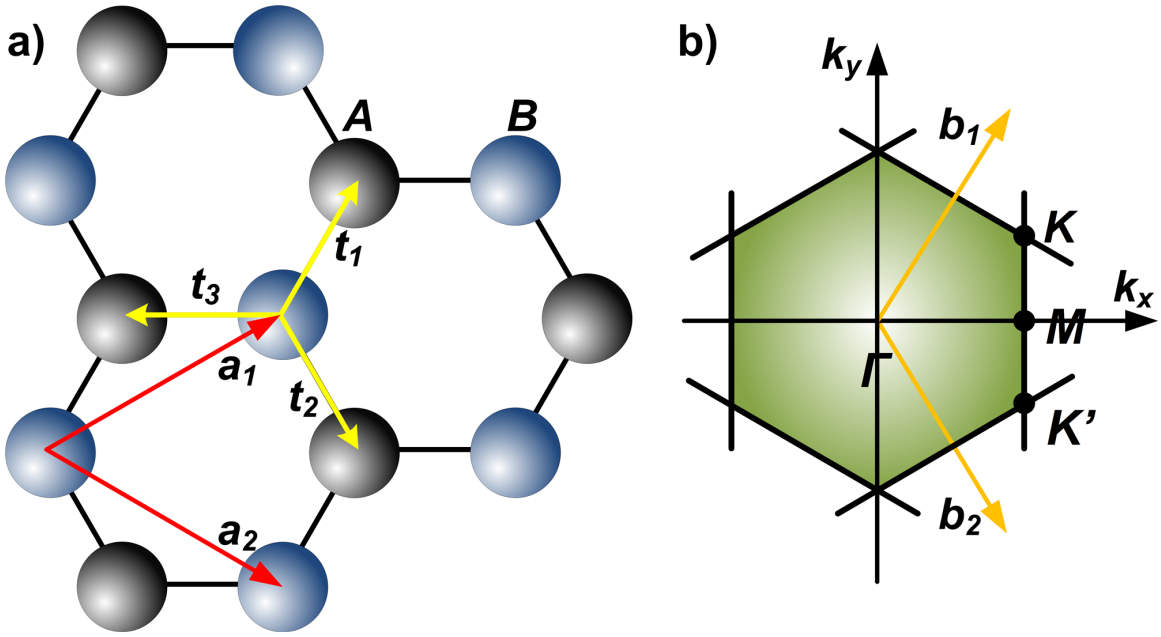

Figure 1.2: (a) Graphene hexagonal network is made up two interpenetrating sublattices *A* (black spheres) and *B* (blue spheres). $\mathbf{a_1}$ and $\mathbf{a_2}$ are lattice vectors (red arrows) of the unit cell (2.46 Å). The nearest neighbors are represented by vectors (yellow arrows) $\mathbf{t_1}$, $\mathbf{t_2}$ and $\mathbf{t_3}$. (b) The perpendicular bisectors of the reciprocal lattice vectors (orange arrows) $\mathbf{b_1}$ and $\mathbf{b_2}$ enclose the first 2D Brillouin zone (green colored region). **Γ** , **K** (**K'**) and **M** are the points high symmetry.

1.2.1 Geometry in Real and Reciprocal Space

Graphene is a hexagonal network of sp_2 bonded carbon atoms that follow trigonal planar geometry as shown in Fig. 1.2(a). Its unit cell is a triangular lattice, that has a basis of two carbon atoms. This hexagonal network is not a Bravais lattice, and can be viewed as a combination of two independent equivalent carbon sublattices A and B. The sublattices A and B, are identified as black and blue spheres in the figure (Fig. 1.2(a)). The lattice vectors $\mathbf{a_1}$ and $\mathbf{a_2}$ representing the unit cell, are shown in the figure and are given by:

$$\mathbf{a_1} = \frac{a}{2}(3,\ \sqrt{3}) \tag{1.1}$$

$$\mathbf{a_2} = \frac{a}{2}(3,\ -\sqrt{3}) \tag{1.2}$$

where, $a \approx 1.42$ Å is the distance between two neighboring carbon atoms. The size of the unit cell is $|\mathbf{a_1}|=|\mathbf{a_2}|=2.46$ Å. The vectors for nearest neighbor carbon atoms $\mathbf{t_1}$, $\mathbf{t_2}$ and $\mathbf{t_3}$ are given by:

$$\mathbf{t_1} = \frac{a}{2}(1,\ \sqrt{3}) \tag{1.3}$$

$$\mathbf{t_2} = \frac{a}{2}(1,\ -\sqrt{3}) \tag{1.4}$$

$$\mathbf{t_3} = -a(1,0)) \tag{1.5}$$

The six second nearest neighbors are located at: $\mathbf{t_1^{'}} = \pm\mathbf{a_1}$, $\mathbf{t_2^{'}} = \pm\mathbf{a_2}$, $\mathbf{t_3^{'}} = \pm(\mathbf{a_2} - \mathbf{a_1})$.

The 2D hexagonal reciprocal lattice is given by reciprocal vectors $\mathbf{b_1}$ and $\mathbf{b_2}$. Where,

$$\mathbf{b_1} = \frac{2\pi}{3a}(1,\ \sqrt{3}) \tag{1.6}$$

$$\mathbf{b_2} = \frac{2\pi}{3a}(1,\ -\sqrt{3}), \tag{1.7}$$

and they are represented by green arrows in Fig. 1.2(b). The perpendicular bisectors of the reciprocal vectors enclose the Wigner-Seitz cell (green colored) in the reciprocal space, or the first Brillouin zone (BZ). High symmetry points $\mathbf{\Gamma}$, $\mathbf{K}$ and $\mathbf{M}$ in graphene are also indicated in the Figure The $\mathbf{\Gamma}$ point is at the zone center, where $\boldsymbol{k}$=0. The six $\mathbf{K}$ points at the corner of the hexagonal BZ are of particular interest, as the electronic structure of graphene is localized at these high symmetry points. The two neighboring high symmetry $\mathbf{K}$ points, namely $\mathbf{K}$ and $\mathbf{K^{'}}$ are inequivalent (Fig. 1.3(a)). These points are given by:

$$\mathbf{K} = \left(\frac{2\pi}{3a}, \frac{2\pi}{3\sqrt{3}a}\right) \tag{1.8}$$

$$\mathbf{K^{'}} = \left(\frac{2\pi}{3a}, -\frac{2\pi}{3\sqrt{3}a}\right) \tag{1.9}$$

The $\mathbf{K}$ point is commonly referred to as Dirac point for reasons that will be discussed later. The symmetry point $\mathbf{M}$ exists on the BZ boundary midway between the $\mathbf{K}$ and $\mathbf{K^{'}}$ points.

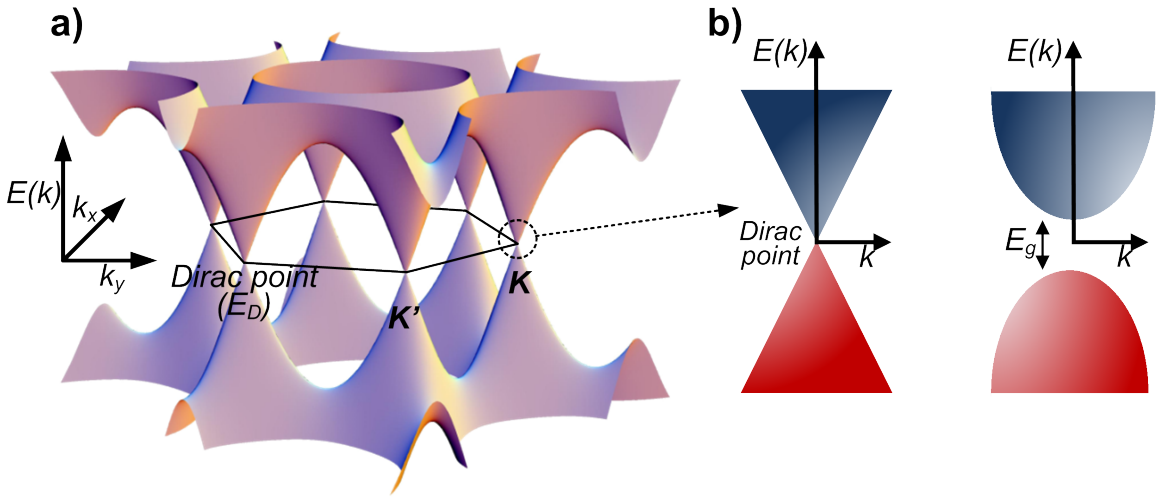

Figure 1.3: The low energy dispersion of single layer graphene. (a) The energy dispersion at the six corners of the Brillouin zone is linear for a single layer graphene. The conduction bands (π^*) and the valence bands (π) intersect at a point. This point of intersection is called the *Dirac point (E_D)* due to the nature of charge carriers, that behave as massless relativistic particles. These quasiparticles move with a constant speed of $c/300$ ms^{-1}, where, c is the speed of light. (b) A slice of the energy dispersion relation shows contrasting electronic structure of graphene as compared to traditional semiconductors. Semiconductors typically exhibit parabolic conduction and valence bands separated by an energy gap (E_g). The blue and red colored bands denote conduction and valence bands, respectively.

As mentioned previously, A and B atoms constitute two interpenetrating sublattices. The two sublattices are equivalent, which gives rise to a unique sublattice symmetry in graphene. This symmetry is the primary reason behind the unique electronic properties of graphene, and is discussed in the following sections.

1.2.2 Electronic Structure

Theoretical calculations to study the electronic structure of graphene were first carried out by Wallace [215] in 1947. This served him as a starting point to study the electronic properties of graphite. He observed unusual semi-metallic properties for the 2D crystal, which were ignored at that time, as it was believed that 2D crystals were unstable and cannot exist in nature [148]. As mentioned previously, the non hybridized p_z orbitals extend perpendicular to the trigonal planar arrangement. These delocalized p_z orbitals are responsible for the unique electronic properties exhibited by graphene.

Tight binding calculations can be applied for low energy electronic dispersion ($E(\mathbf{k})$) in graphene. The Schrödinger equation can be written as:

$$\mathbf{H}\Psi = E(\mathbf{k})\Psi \tag{1.10}$$

where, Ψ is a linear combination of the Bloch wavefunctions, $\mathbf{H}$ is the hamiltonian and E($\mathbf{k}$) represents energy eigenvalues. The Hamiltonian $\mathbf{H}$, taking into account both the nearest and the next nearest neighbor carbon atoms is given as ($\hbar$=1) [161]:

$$\mathbf{H} = -\tau \sum_{\langle i,j\rangle,\sigma} (a^{\dagger}_{\sigma,i} b_{\sigma,j} + H.C.) - \tau' \sum_{\langle\langle i,j\rangle\rangle,\sigma} (a^{\dagger}_{\sigma,i} a_{\sigma,j} + b^{\dagger}_{\sigma,i} b_{\sigma,j} + H.C.) \tag{1.11}$$

where, H.C. stands for hermitian conjugate, τ is the nearest neighbor hopping energy ($\approx 2.8\ eV$) i.e. hopping to a different sublattice, τ' is the next nearest neighbor hopping energy i.e. hopping to the same sublattice. The operator $a_{i,\sigma}(a^{\dagger}_{i,\sigma})$ annihilates (creates) and electron having spin σ ($\sigma = \uparrow, \downarrow$) on i, in sublattice A. This hamiltonian was employed by Wallace [215] to derive the energy band structure given by [161]:

$$E_{\pm}(\mathbf{k}) = \pm\tau \sqrt{3 + \zeta(\mathbf{k})} - \tau'\zeta(\mathbf{k}) \tag{1.12}$$

where,

$$\zeta(\mathbf{k}) = 2\cos(\sqrt{3}k_y) + 4\cos\left(\frac{\sqrt{3}}{2}k_y a\right)\cos\left(\frac{3}{2}k_x a\right) \tag{1.13}$$

here, the positive and the negative signs imply π and π^* bands. If τ' is zero, then the bands become symmetric.

$$E_{\pm}(\mathbf{k}) = \pm\tau \sqrt{3 + 2\cos(\sqrt{3}k_y a) + 4\cos\left(\frac{\sqrt{3}}{2}k_y a\right)\cos\left(\frac{3}{2}k_x a\right)} \tag{1.14}$$

Figure 1.3(a) shows the energy dispersion from the above equation. The zoom in at the K or the K′ point is also shown in the Figure The energy dispersion can be expanded close to point $\mathbf{k} = \mathbf{K}+\mathbf{q}$. Where, $|\mathbf{q}| \ll |\mathrm{K}|$ is given by:

$$E_{\pm}(\mathbf{q}) \approx \pm\frac{3\tau a}{2}|\mathbf{q}| + O((q/\mathbf{K})^2) \tag{1.15}$$

Ignoring the higher order terms the equation can be rewritten as:

$$E_{\pm}(\mathbf{q}) = \pm v_F|\mathbf{q}| \tag{1.16}$$

where, v_F is called the Fermi velocity and it has a fixed speed of $\simeq 1 \times 10^6\ ms^{-1}$ [215]. Two striking results emerge out of this derivation, that sets graphene apart from the other semiconductor materials. The low energy electronic dispersions in graphene do not depend on the mass of the charge carrier, in other words, the charge carriers in graphene behave like massless particles. This is similar to Dirac particle like behavior in relativity, hence the charge carriers in graphene are also known as the *Dirac particles*. It is also of interest to note that, the Fermi velocity v_F doesn't depend on the electron mass. Figure 1.3(b) illustrates these contrasting properties of graphene compared to the traditional semiconductors. The point of intersection of the π and π^* bands is called the *Dirac point*, indicated in Fig. 1.3(b). For undoped graphene the Fermi level lies at the Dirac point energy (E=0). The lower inverted cone (red colored) is filled with electrons and represents valence bands and the upper cone (blue colored) is the unfilled conduction band.

For simplification, if we consider the hamiltonian with $\tau' = 0$, then:

$$\mathbf{H} = -\tau \sum_{\langle i,j\rangle,\sigma} (a^{\dagger}_{\sigma,i} b_{\sigma,j} + H.C.) \tag{1.17}$$

The hamiltonian **H** can be rewritten in terms of the fourier transform of operators a and b. These can be expanded around points **K** and **K'** (please see Ref. [161] for detailed analysis). An alternative expression for the hamiltonian **H** is given by:

$$H = -iv_F \int dxdy \left((\Psi^{\dagger}_1(\mathbf{r})\boldsymbol{\sigma}.\nabla\Psi_1(\mathbf{r})) + ((\Psi^{\dagger}_2(\mathbf{r})\boldsymbol{\sigma}^*.\nabla\Psi_2(\mathbf{r})) \right) \tag{1.18}$$

where, $\boldsymbol{\sigma} = (\sigma_x, \sigma_y)$ and $\boldsymbol{\sigma}^* = (\sigma_x, -\sigma_y)$ are the pauli matrices. $\Psi_i = (a_i, b_i)$ where, i=1,2 and denotes point **K** and **K'** . The hamiltonian H has two components, one each for **K** and **K'**. Now around the **K** point the two component electron wavefunction is given by:

$$-iv_F\sigma.\nabla\psi(\mathbf{r}) = E\psi(\mathbf{r}) \tag{1.19}$$

where, $\psi(\mathbf{r})$ around the **K** point is:

$$\psi_{\pm,\mathbf{K}}(\mathbf{k}) = \frac{1}{\sqrt{2}}(e^{-i\theta_k/2}, \pm e^{i\theta_k/2}) \tag{1.20}$$

and $H_{\mathbf{K}} = v_F\boldsymbol{\sigma}.\mathbf{k}$. Here $\pm$ corresponds to energies for the π and the π^* band and $\theta_k = \arctan(k_x/k_y)$. Similarly for **K'**, wavefunction is given as:

$$\psi_{\pm,\mathbf{K}'}(\mathbf{k}) = \frac{1}{\sqrt{2}}(e^{i\theta_k/2}, \pm e^{-i\theta_k/2}) \tag{1.21}$$

and $H_{\mathbf{K}'} = v_F\boldsymbol{\sigma}^*.\mathbf{k}$

A few interesting properties follow from Eq. 1.20 and 1.21. The wavefunction changes sign if the phase θ is changed by 2π. This indicates a phase of π and is commonly referred as the *anomalous Berry's phase*. This a hallmark of single layer graphene and it has been experimentally observed in transport measurements [227]. This suggests that the wavefunction is a two-component spinor.

The *Dirac-like* relativistic behavior exhibited by the charge carriers in graphene leads to many interesting properties. The relationship between cyclotron mass and the electron density of states is unique in graphene, and is given by [166, 227]:

$$m^* = \frac{\sqrt{\pi}}{v_F}\sqrt{n} \tag{1.22}$$

where m^* is the cyclotron mass. In recent experiments [56, 99, 166, 227], the $\sqrt{n}$ dependence has been observed. This suggests presence of *Dirac-like* particles in graphene.

In the past, it was assumed that 2D crystals could not exist in nature. It was shown that the thermal fluctuations alone could destroy the long range order in 2D crystals [118, 148], rendering them unstable. In graphene there exists out-of-plane phonon modes that can causes ripples in graphene topology. These can be controlled to a certain degree by supporting graphene on a substrate, thereby preventing crumpling. Meyer *et al* [149] studied free suspended graphene sheets in vacuum supported only at the edges. Using transmission electron microscopy (TEM), they observed intrinsic deformations in the graphene lattice that can reach upto 10 Å.

1.2.2.1 Klein Paradox in Graphene

Electrostatic potentials due to disorder are responsible for scattering in a material. The disorder could be due to atomic scale defects, corrugation in the film, species adsorbed on the surface of

the material, and an interaction with the substrate. It is known that in quantum electrodynamics the relativistic particles are insensitive to external electrostatic potentials due to *Klein paradox* [107]. Charge carriers in graphene have an unusual *Dirac-like* behavior. These fermions under certain conditions are immune to scattering and localization effects observed in ordinary electrons. They can travel upto distances of micron scale without scattering [167].

In quantum mechanics, a particle like electron incident on a potential barrier of height greater then its kinetic energy, transmits through the barrier with a finite probability. The transmission probability decreases with an increase in barrier height in the non-relativistic processes. In relativistic quantum processes, an electron starts penetrating through the barrier when its rest energy (mc^2) becomes less than half the potential barrier height. Traditionally, in a non relativistic process , the transmission probability increases with an increase in the barrier height becoming perfectly transparent for very high barriers. This effect has been explained by generation of positron states in the high barrier [77]. This barrier is attractive for positrons and repulsive for electrons. The energy states of both the electrons and the positrons align at the interface, leading to wavefunction matching, which results in a high transmission probability. This effect has not been observed experimentally thereby creating a paradoxical situation.

As mentioned previously, graphene electrons and holes states are connected via sublattice symmetry, which requires the quasi-particle wavefunctions to have two components that include contributions of both the sublattices. The spin component, *pseudospin* represents different sublattices in graphene. This situation is similar to spinor wavefunctions in quantum electrodynamics (QED). Due to the above mentioned similarities, relativistic phenomenon can be experimentally observed in graphene. Katsnelson *et al* [104] theoretically calculated the transmission probability, given by:

$$T(\phi) \simeq \frac{cos^2\phi}{1 - cos^2(Dq_x)sin^2\phi} \tag{1.23}$$

where, D is the barrier width, $\phi = \arctan(k_y/k_x)$ and

$$q_x = \sqrt{(V_0 - E)^2/(v_F^2) - k_y^2}. \tag{1.24}$$

v_F is the Fermi velocity, V_0 is the barrier height and E is the energy of the incident electron. The derivation assumes a square potential barrier.

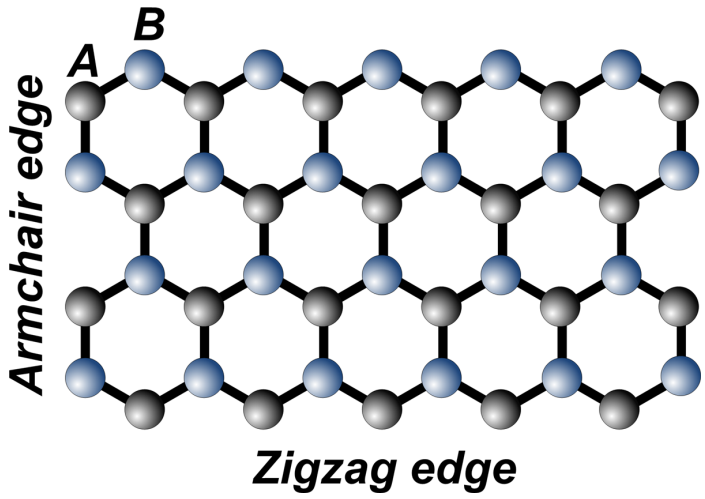

Figure 1.4: (a) The two possible edge termination of graphene lattice, namely: zigzag (horizontal direction) and armchair (vertical direction). Armchair edge consists of carbon atoms from both sublattice and the zigzag edge consists of carbon atoms from the same sublattice. Different electronic properties are seen for the two terminations [158].

1.2.2.2 Trigonal Warping

At the **K** valley, the electrons (holes) have an energy vp (-vp), where **p** is the momentum. The chirality for electrons and holes in this valley is therefore $\boldsymbol{\sigma}\mathbf{p}/p = 1$ and $\boldsymbol{\sigma}\mathbf{p}/p = -1$ respectively. The chirality however is reversed in case of valley $\mathbf{K}'$, $\boldsymbol{\sigma}\mathbf{p}/p = -1$ for electrons and $\boldsymbol{\sigma}\mathbf{p}/p = 1$ for holes. The dispersion in graphene is dependent on the direction in the momentum space, due to the quadratic term in Eq. 1.15. This introduces some anisotropy in the graphene electronic spectrum, and causes a small *trigonal warping* (three fold symmetric). This breaks the valley symmetry in graphene, the strength of which depends on the degree of warping [144].

It is known that due to sublattice symmetry (**A** and **B**) and chiral nature of electrons, scattering processes are unable to backscatter the charge carriers [12]. Trigonal warping suppresses this anti-localization [144] which can lead to small back-scattering in graphene. As a consequence, conventional weak localization may be restored. Traditionally absence of back scattering has been linked to weak anti-localization [12].

1.2.2.3 Graphene Ribbons

The graphene lattice can have two kinds of edge termination, zigzag and the armchair configuration. Figure 1.4(a) shows the zigzag and the armchair terminations along the carbons A and B of the two

equivalent sublattices. Zigzag edge only has carbon atoms from a single sublattice due to which localized electronic states appear along the zigzag edge [158, 159]. The energy dispersion in the direction of the zigzag edge is flat, and therefore a sharp maximum is observed in the density of states at the Fermi energy. An armchair edge, however, has carbon atoms from both the sublattices. As a result, this configuration does not yield localized states and behaves as an infinite graphene lattice.

Confinement of particles causes the appearance of discrete quantized energy levels. This is analogous to the particle in a box problem in quantum mechanics [78]. Theoretical calculations by Son *et al* [199], suggest quantization of the energy levels due to confinement in graphene. The energy separation between the quantized levels depends on the width of the graphene ribbon.

1.3 Methods of Production

Unique extraordinary electronic properties of graphene, have prompted the scientific community to explore and develop methods to produce graphene. Perhaps, the most ingenious method that is believed to have started the graphene rush is mechanical exfoliation of graphene [166, 167, 227]. This process involves peeling graphene layers off the bulk graphite crystal using an adhesive tape. Different flavors of graphite, for example highly oriented pyrolytic graphite (HOPG), Kish graphite or other naturally occurring graphite are used as a source. In this method, an adhesive tape is placed on the bulk graphite and pressed down to ensure good contact. Topmost layers of graphite are then peeled away in a certain manner to ensure high yield. The material on the tape is transferred to 300 nm SiO_2 grown on top of degenerately doped Si, by rubbing against it. The 300 nm thick SiO_2 creates a subtle optical effect [7, 40, 74, 157], making it easier to locate and identify graphene flakes with an optical microscope. Although this method is crude and it is tedious to accurately identify single-layer graphene in a sea of thicker flakes, it has been very successful in creating samples for table top experiments. Graphene flakes identified by virtue of this optical effect are further confirmed by their Raman spectroscopy [68].

Graphene samples prepared by this method suffer from intrinsic drawbacks. Giant corrugations have been reported in these flakes at smaller lateral distances [97, 226]. These corrugations were previously believed to be due to intrinsic corrugation of the graphene itself [149, 150]. These

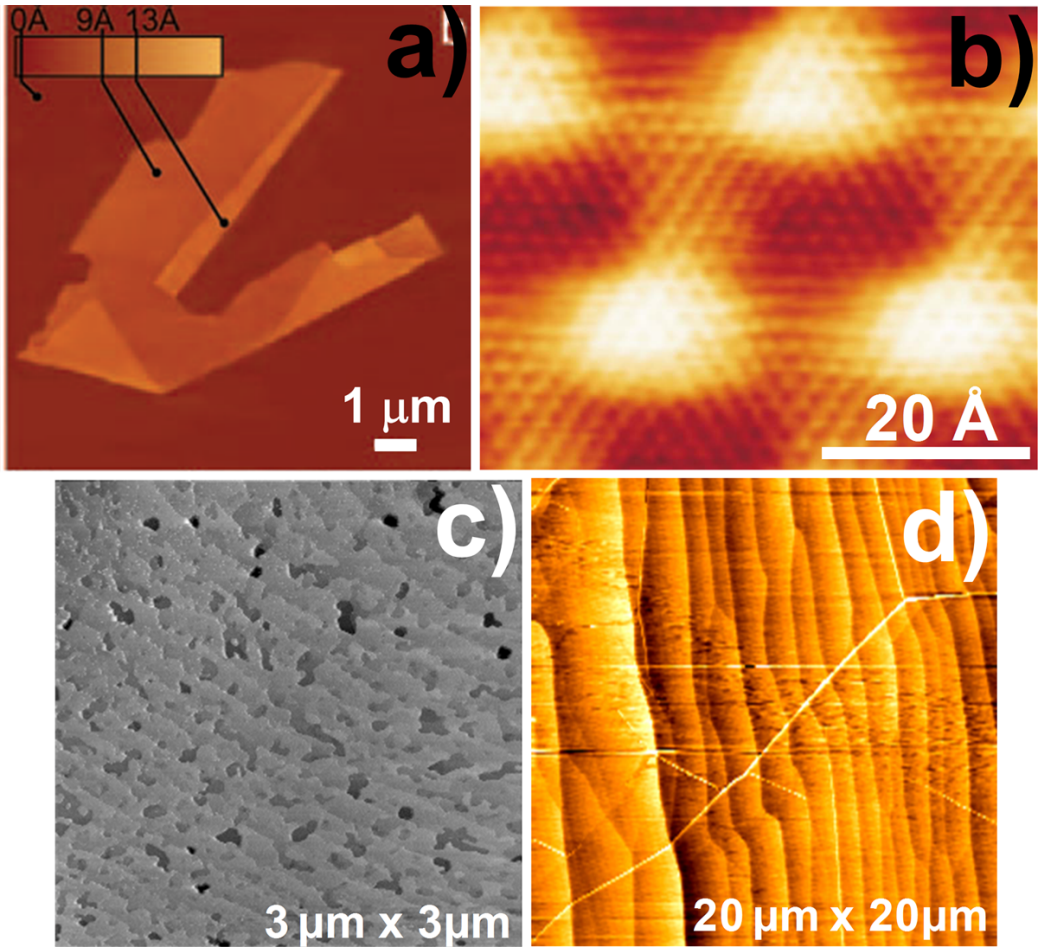

Figure 1.5: Different graphene production methods. (a) Mechanically exfoliated graphene on SiO_2 laying on heavily doped Si. Single layer graphene is identified by a subtle optical effect on 300 nm SiO_2. The figure is taken from reference [168]. (b) High resolution STM image (50 Å × 40 Å) of graphene on Ru(0001) showing 25 × 25 supercell (-0.07 V, 1 nA). The figure is taken from reference [134]. (c) A large STM image (3 μm × 3 μm) on the Si-face showing a topography dominated by SiC steps and large scale roughness (3 V, 100 pA). The sample is 2.3 ML thick. (d) STM survey scan (20 μm × 20 μm) of EG on the C-face showing large graphene terraces and puckers in the graphene film (3 V, 100 pA).

corrugations were also believed to be responsible for absence of low field magnetoresistance in graphene on SiO_2 [155]. However measurements done by Ishigami *et al* [97], suggest that graphene on SiO_2 conforms partially to the underlying SiO_2, that has giant surface roughness. There are also charge fluctuations in the underlying SiO_2 substrate. The graphene flakes produced by mechanical exfoliation are ~10-100 μm size, making it unviable wafer scale production method required for the semiconductor industry.

Following the work of Novesolov *et al* [167], other mechanical exfoliation methods have been developed. One such production method is based on intercalation and ultrasonic treatment of graphite to isolate graphene flakes [221]. This method employs ultrasonic treatment of graphite in water, which produces graphene flakes. This process of delamination can be dramatically enhanced by intercalation of bromine from a Br_2 saturated water solution. This method, however, suffers from low yield and small sized flakes.

Growth of high quality graphene films has also been demonstrated on transition metals. The first successful report of layered graphene growth was published in 1983 by Rosei *et al* [193]. In this method, Ni(111) substrates were exposed to 10^{-5} to 10^{-6} Torr of CO during high temperature ultra-high vacuum (UHV) cleaning. Graphitic growth on other metal carbides (WC, HfC, TaC and TiC) has also been reported [9, 10, 98]. In these reports a shift in graphene bonds was observed, which was related to the expansion in the graphene lattice. These shifts were previously believed to be consequence of charge transfer from the substrate. Nagashima *et al* found that the chemical shift is due to rehybridization of substrate and graphene bonds [156]. Recently single layer graphene films have been reported on Ru(0001) [177, 206]. Fig. (b) shows an STM image of graphene on Ru(0001) with a *Moiŕe* pattern. The *Moiŕe* pattern seen in these films [134] has been explained [216] by buckling of the graphene films due to an alternating weak and strong interaction with Ru. This strong interaction may result in band gap opening and charge transfer from metals [216].

High quality graphene films can be grown epitaxially on SiC crystals, a potential route towards wafer-scale production. In this method, hexagonal SiC samples are annealed under UHV conditions to temperatures above 1200 $^{\circ}C$. Under such conditions, Si desorbs form the sample and carbon atoms that are left behind naturally form graphene films that are in registry with the underlying substrate. Depending on ambient conditions and the final annealing temperature, several graphene layers can be grown on SiC. Graphene growth has been demonstrated on both the Si- (0001) and C-$(000\bar{1})$ terminated faces of hexagonal bipolar SiC crystal. In this thesis work, growth and electronic structure of graphene films on the Si-face of SiC crystal has been investigated with various surface science techniques that will be discussed in detail in Chapter. 3.

CHAPTER II

EXPERIMENTAL TECHNIQUES

In this thesis research, a lot of different surface science techniques were used in conjunction with one another. The primary techniques used in this work are STM, STS, LEED, AES and Raman Spectroscopy that will be discussed in detail in the following sections. All ultra-high vacuum (UHV) growth of the epitaxial graphene, and most of the characterization was done in a home-brewed room temperature (RT) system [189]. The Raman measurements were done via Reinshaw spectrometer RM 1000 at the materials science and engineering department at Georgia Institute of Technology. The RT system (see Fig. 2.1) has a base pressure of $\sim 1\times10^{-10}$ Torr. It is equipped with an ion pump, turbo mechanical pump, diaphragm pump, titanium sublimation pump (TSP) for maintenance of UHV environment. The various surface science mounted on the chamber are low energy electron diffraction (LEED), Auger electron spectroscope(AES), scanning tunneling microscope (STM) and field emission microscope (FEM). Sample preparation and cleaning is done by an electron-beam heater mounted on a sample manipulator which is capable of motion in three translational directions, and one rotational direction. STM tips are cleaned by an electron-beam heater. The chamber is also equipped with a sputtering gun and two material (Ni and C) deposition setups.

2.1 Scanning Tunneling Microscope

STM remains an extraordinary tool even 27 years after it was invented by Rohrer and Binnig in 1982 [30, 32]. They were awarded the Nobel prize for its invention in 1986. It has been a powerful tool to extract both atomically resolved topographic and electronic information. In this technique, a sharp metal probe is brought within a distance of a few angstrom to the sample of interest, and a voltage bias is applied between them. If the tip and the sample are close enough, a tunneling current is obtained through the vacuum gap. Figure 2.2 shows a sharp metal probe in close proximity of the sample with a voltage bias between them. The observed tunneling current depends on the magnitude of the bias voltage (V), distance between the tip (d) and the sample, and the local density of states of both the tip and the sample under investigation. In our room temperature system, the tunneling

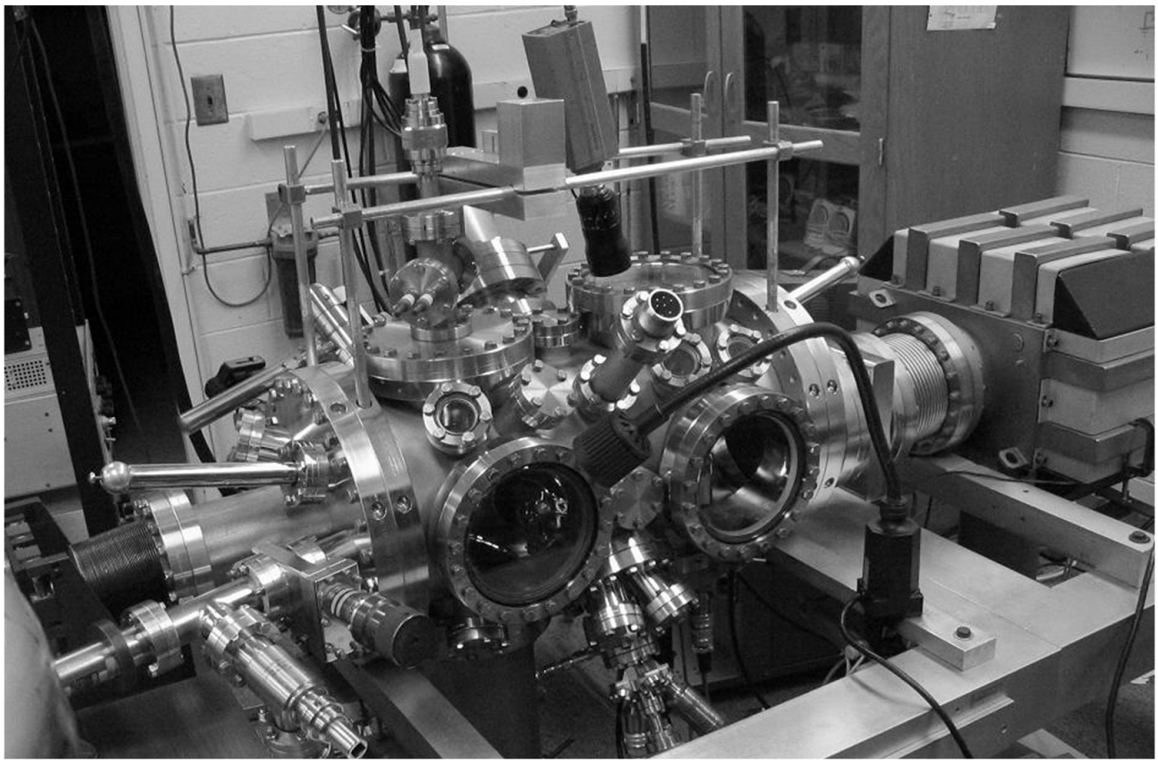

Figure 2.1: An image of the room temperature system. The system has a base pressure of 1×10^{-10} Torr. The system is equipped with various surface science techniques, namely: scanning tunneling microscopy, Auger electron spectroscopy, low energy electron diffraction, field emission microscopy and more. Ultra-high vacuum is maintained by titanium sublimation pump (TSP) and an ion pump, in addition to a diaphragm pump and turbo molecular pump for sample transfers. The reader is referred to Ph.D. thesis work of Paul Quesenberry [189] for more details.

current is amplified by a factor of 10^8 by a current to voltage convertor, mounted on the STM stage itself [189]. The reader is referred to the Ph.D. thesis work of Paul Quesenberry [189] for details about the working and construction of our home-built scanning tunneling microscope.

In STM, both the tip and the sample are made up of conducting materials. All data reported in this thesis work was acquired by chemically etched tungsten tips, which are cleaned *in situ* by e-beam bombardment. Our samples are held at virtual ground and the bias voltage is applied to the tip. However, the sample bias voltages are reported in the thesis. In principle, a negative bias voltage probes the filled states and a positive bias voltage probes the empty states of epitaxial graphene (EG). In the energy range that we deal with, the tip (metal) DOS of states does not vary much and can be treated as a constant. Therefore, only the sample LDOS plays an important role. Clean surfaces and tips are required for STM measurements as impurities can modify the electronic properties of

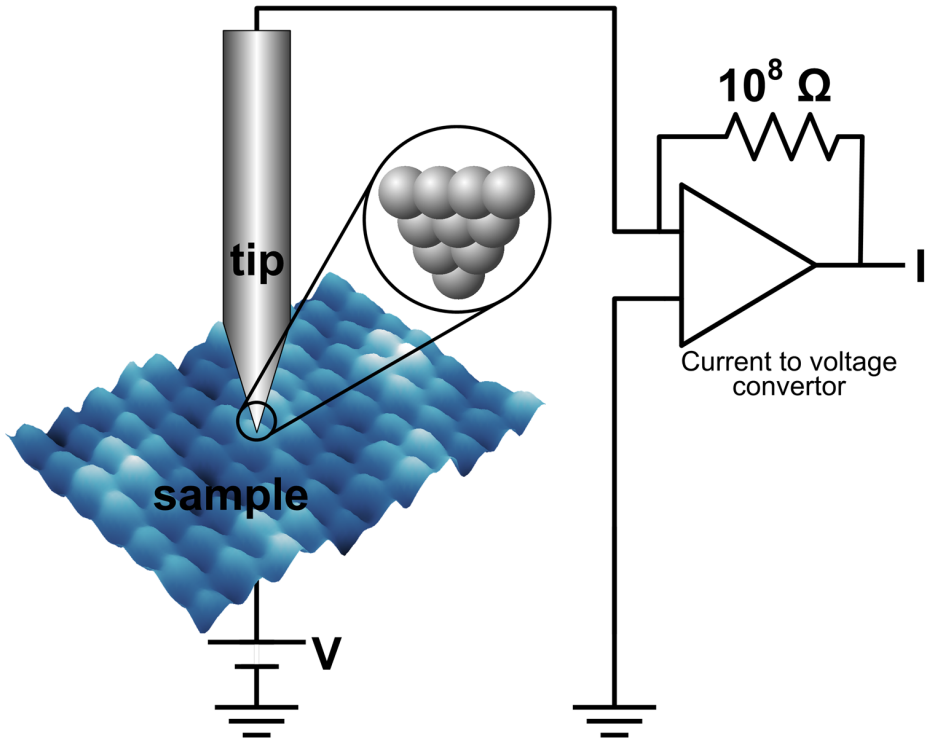

Figure 2.2: A scanning tunneling microscope is based on the principle of quantum mechanical tunneling. A sharp tip (zoom in) is brought close to the sample and a voltage bias is applied between them. A tunneling current is observed which depends on the voltage bias (V), distance between the tip and sample and the density of states (DOS) of both the tip and the sample. The tunneling current in the room temperature system gets amplified by a factor of 10^8 with an internal current to voltage convertor [189].

the sample. Typically, after the sample preparation, STM based measurements are done under UHV conditions.

2.1.1 Theory and Working

STM is based on the principle of quantum mechanical tunneling, which classically is a forbidden process. The potential barrier V_B for simplification is replaced by its average value (a constant) in the barrier (square potential barrier). An analytic solution for the tunneling current can be derived by solving the Schrödinger's equation of the quantum mechanical problem. One dimensional Schrödinger equation for the problem can be written as:

$$-\frac{\hbar^2}{2m}\frac{\partial^2\psi(z)}{\partial^2 z} + V_B\psi(z) = E\psi(z) \tag{2.1}$$

where, E is the energy of the incident electron, $\hbar$ is the Planck's constant and since $E < V_B$, $\psi(z)$ is a decaying wavefunction in the barrier is given by:

$$\psi(z) = \psi(0)e^{\pm\kappa z} \tag{2.2}$$

where,

$$\kappa = \frac{\sqrt{2m(v_B - E)}}{\hbar} \tag{2.3}$$

is the decay constant. The tunneling current based on this simple model is given by:

$$I \propto e^{-2\kappa d} \tag{2.4}$$

It immediately follows from the above expression that, the tunneling current is very sensitive to the distance between the tip and the sample. Work function of most of the metals used for preparing tips, lies between 4-5 eV this gives us, $\kappa \sim 1$ Å^{-1}. This suggests that for every 1 Å change in the separation, the tunneling current changes by an order of magnitude.

An analytic solution to the tunneling problem was first proposed by Bardeen [21]. He applied time-dependent perturbation theory (Fermi's golden rule) to estimate the rate at which electrons cross the tunneling barrier. A tunneling matrix $\boldsymbol{M}$, can be obtained by solving the Schrödinger equation on either side of the barrier for wavefunctions ψ_μ and ψ_ν. The matrix $\boldsymbol{M}$ is a result of a small overlap between the two wavefunctions. This analytic treatment was later extended to STM by Tersoff [207] by asumming ψ_μ and ψ_ν as tip and the sample wavefunctions, respectively. The tunnel matrix element $\boldsymbol{M}$ is given by:

$$\mathbf{M}_{\mu\nu} = \frac{\hbar^2}{2m}\int d\mathbf{S}.(\psi_\mu^*\nabla\psi_\nu - \psi_\nu\nabla\psi_\mu^*). \tag{2.5}$$

In general, the Fermi's golden rule is given by:

$$R_{if} = \frac{2\pi}{\hbar}|\mathbf{M}_{if}|^2\rho_f \tag{2.6}$$

where, R is the transition probability and ρ_f is the density of final states.

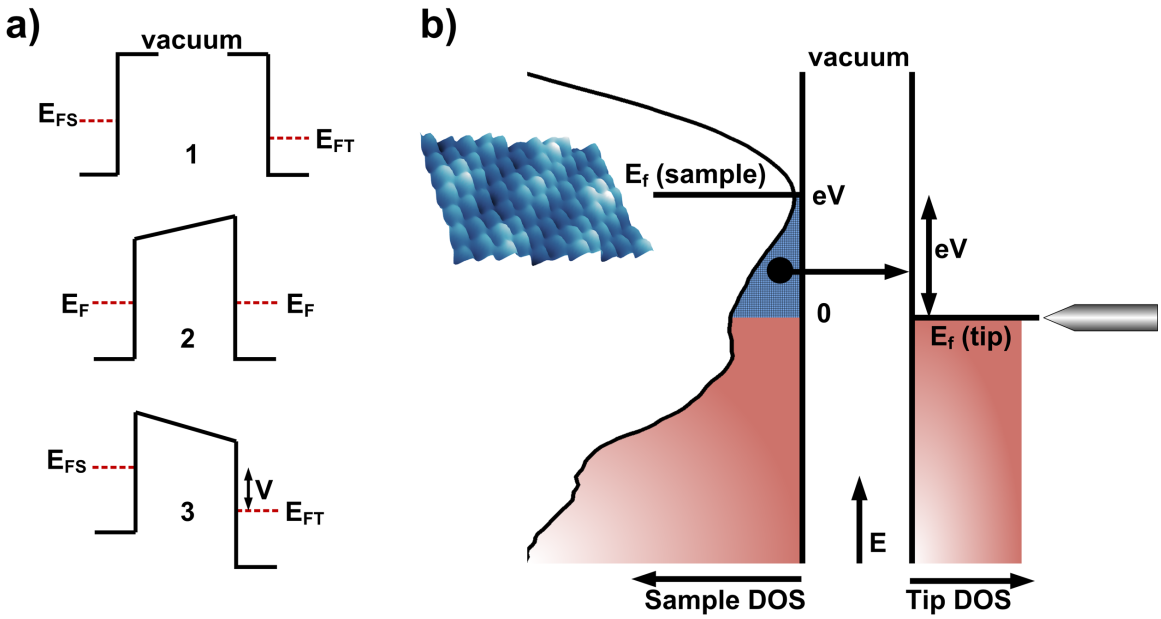

Figure 2.3: Process of vacuum tunneling. (a1) Two conducting materials of different work function (E_{FS} and E_{FT}) have no interaction when they are far apart from each other. (a2) When the two materials are allowed to come close, an equilibrium is established by alignment of the Fermi level. (a3) A voltage -V applied to the sample raises its Fermi level by an amount eV with respect to the Fermi level of the tip. (b) A voltage bias of -V enables the electrons in filled states of graphene to tunnel into empty states of the tip. The window for electron tunneling process is eV between the two Fermi levels.

In Fig. 2.3(b), a negative voltage -V is applied to the sample which effectively raises the Fermi level of the sample by eV with respect to the fermi level of the tip. The total tunneling current from the tip to the sample is given by:

$$I \approx \frac{4\pi e}{\hbar} \int_0^{eV} |\mathbf{M}|^2 \rho_s(\varepsilon)\rho_t(\varepsilon + eV)d\varepsilon \tag{2.7}$$

where, ρ_s and ρ_t are the tip and sample local density of states. Now, according to Wentzel Kramers Brillouin (WKB) approximation, potential barrier is assumed to be square barrier. Therefore, a simplified tunnel matrix element is given by:

$$|\mathbf{M}|^2 = e^{-2\int_0^d \sqrt{\frac{2mV_B}{\hbar^2}}dx} \tag{2.8}$$

where, V_B and d are the square barrier height and width respectively.

In our experiments, almost all of the data has been acquired with tungsten tips, which is believed

to have flat density of states near its Fermi surface. The tip density of states ρ_t can be treated as a constant and taken out of the integral sign. The equation for the tunneling current then simplifies to

$$I \approx \frac{4\pi e}{\hbar} e^{-\frac{2d}{\hbar}\sqrt{2mV_B}} \rho_t(0) \int_0^{eV} \rho_s(\varepsilon) d\varepsilon \tag{2.9}$$

where, V_B, the height of the barrier is a combination of tip and sample work functions. A higher value of V_B makes the tunneling current more sensitive to the separation d and gives better resolution.

2.1.2 Scanning modes in STM

There are two different ways to scan on a sample. They are referred as the *constant current* and *constant height* mode.

In *constant current* mode, the tip is scanned across the sample with the tunneling current kept constant at the desired locations. This is done by changing the tip sample separation. The separation (z) and any spectroscopic information is recorded. A constant current is maintained by enabling a feedback loop, that keeps the tunneling current constant.

In *constant height* mode, the tip is scanned across the sample with the separation (z) between the tip and the sample, held constant, and the feedback loop is disabled. The value of the tunneling current (I_t) and any spectroscopic information is recorded at each pre-determined location.

Although, *constant height* mode is a faster mode, *constant current* mode is more popular and is effective for samples that have a rough texture. All STM data in this work has been acquired in the constant current mode. This is done by scanning the tip on the sample at a predetermined value of tunneling current (I_t) and bias voltage (V).

2.1.3 Topographic Imaging

Topographic imaging is the most popular STM mode used by research groups. Typically in this mode a voltage bias (-V) is applied to the sample and the tip is held at virtual ground. The tip is scanned across the sample by applying appropriate voltages to the x and y piezos. A feedback loop is enabled that keeps the the tunneling current constant. At the heart of feedback loop is a logarithmal amplifier that generates an error voltage if any deviations are observed in the tunneling

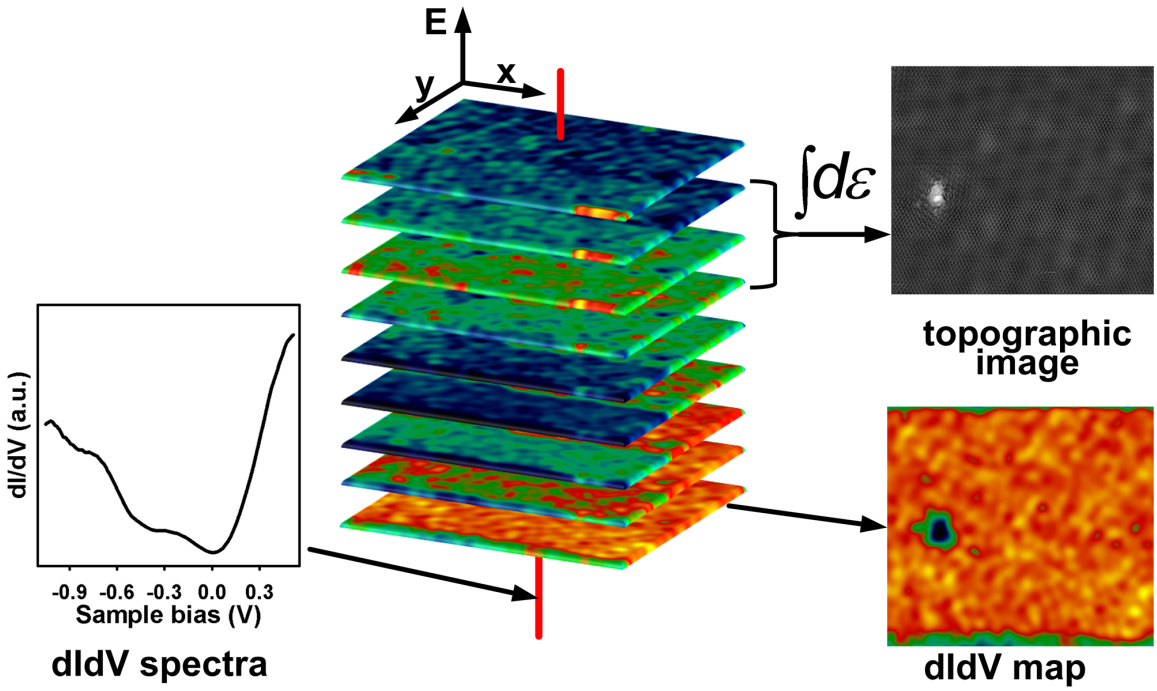

Figure 2.4: Figure illustrating some of the common applications of STM. In topographic imaging mode, a tip rastered across a biased sample (-*V*) generates a height map which is proportional to the integrated DOS below the sample fermi level. The *dI/dV* or the differential conductance spectra (red line) is related to the local density of states. Atomically resolved *dIdV* maps are generated by taking spectra at all the imaging locations.

current (see Fig. 2.3(b)). This error voltage is then applied to the z piezo, that controls the separation between the tip and the sample. This error voltage maps the "height" (topography) of the sample and is recorded at every pixel location. The height map (see Eq. 2.9), is the charge density from the region within eV, between the two fermi levels (see Fig. 2.3(b)). This is the primary reason why topographic imaging in semiconductors and semimetals is bias dependent.

A negative bias voltage (-*V*) (see Fig. 2.3(b)) allows the electrons in graphene filled states to tunnel into the empty metal states. In general, by varying both the magnitude and the sign of the bias voltage, bias dependent topographic maps can be generated. It is important to note that if the bias voltage is too high, then our square barrier approximation breaks down.

2.1.4 Scanning Tunneling Spectroscopy

STM has a unique ability to measure atomically resolved local density of states (*LDOS*) which sets it apart from other local probing techniques. As mentioned in the previous section, topographic

height measurement in the imaging mode, is proportional to the integrated density of states below and above the sample and tip Fermi levels respectively (see Fig. 2.4), for a bias voltage -V applied to the sample. Mathematically,

$$I \propto \int_0^{eV} \rho_s(\varepsilon) d\varepsilon \tag{2.10}$$

DOS is typically measured by employing lock-in techniques. A small modulation voltage dV (few mV, ~1 kHz), is applied to the bias voltage (V) and the resulting modulation in current (dI) is recorded. Thus, DOS at a particular bias voltage is given by:

$$\frac{dI}{dV} \propto DOS(V) \tag{2.11}$$

In our RT system, *LDOS* or conductance information is generated by first acquiring a current-voltage (*IV*) spectra. This is done by disabling the feedback loop and keeping the distance between the tip and the sample fixed at a predetermined value. Spectra is recorded by varying the voltage bias and recording the tunneling current. The *dI/dV* spectra is generated by doing a numerical derivative of *IV* spectra. In STM, one can precisely control the location (*x,y*) where the *IV* spectra is to be taken. The DOS measurement as a function of bias voltage is more commonly known as *scanning tunneling spectroscopy* [202]. Resolution of the spectroscopic data is limited by the thermal broadening effects at finite temperatures. At room temperature, i.e. 300 K thermal broadening is given by $k_BT \approx 0.026$ eV. Where, k_BT is the Boltzman constant (1.38×10^{-23} J/K). Therefore the tip and the sample distribution spread is ≈0.052 eV, and total energy deviation is ≈0.1 eV. In order to avoid the smearing of features in DOS spectra, measurements are preferably done at low temperature (LT) of 4 K or 77 K.

The scanning tunneling spectroscopy can also be used to generate atomically resolved *differential conductance maps*, also called *DOS* or *dIdV* maps. Typically, LT STM is used to generate high resolution maps, where spectra is acquired at every imaging location. The acquisition time for *dIdV* maps is significantly greater than the topographic imaging. Because of this, thermal drift at room temperature can adversely effect the measurements. Therefore, instead of acquiring spectra at every point (fine 1×1 grid), bigger grids (5 X 5) are typically used for room temperature conditions. Time

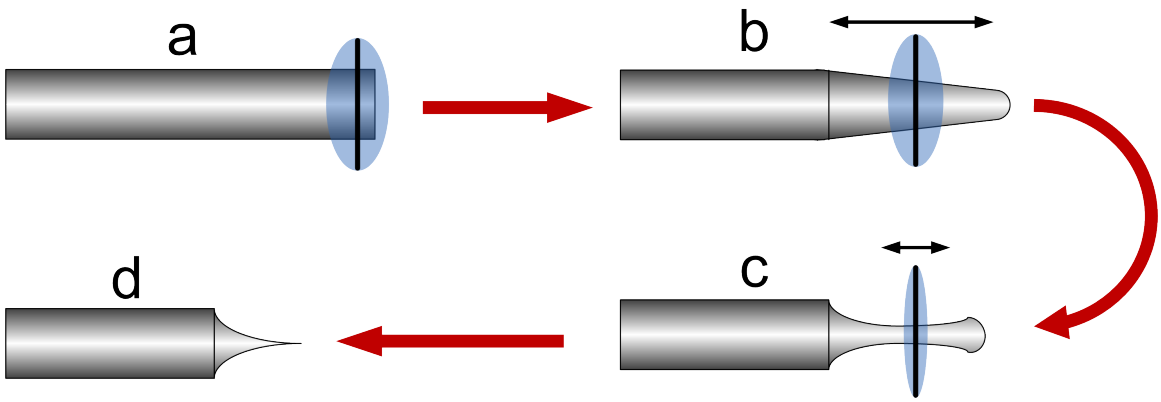

Figure 2.5: Illustration of the process to prepare chemically etched tungsten (W) probe tips. (a) The tip is displaced back and forth between 0.1 M KOH solution, and a voltage (see text for values) is applied between them for electro chemical etching. (b) The process is continued at a lower voltage with a thinner KOH bubble for local etching. (c) At this stage a neck formation takes place and the end breaks off, leaving behind a sharp tip as shown in (d).

spent during the acquisition can also be reduced to a great extent by doing faster spectroscopy. This is done by acquiring a lesser number of data samples (for averaging) per grid location and by cutting back on the time delays between different sample sets. This is also done by cutting down the time delays between data points within the same sample set. Another useful measurement commonly known as a *linecut*, is done by acquiring spectra at discrete points along a straight line.

2.1.5 STM tip preparation

All data in this work has been acquired by tungsten probe tips. Both poly (100) and single (111) crystal tungsten was used to prepare STM probes. For preparation, a thin tungsten wire is spot welded to thicker tungsten shank for easy mount on the STM tip assembly. This is followed by chemical etching methodology of Melmed [147]. The end of the tips are electrochemically etched in the 0.1 M KOH (potassium hydroxide) solution (see Fig. 2.5). A fresh tip is prepared by etching away the end of the tungsten wire. This is done by an initial etch at a fast rate (V_{DC}=4 V). After this, a thin neck is created by moving the tip back and forth between the bubble (V_{DC}=2 V). This is followed by slow etching ($V_{DC} \leq$ 1 V) where the end of the tip falls off leaving behind a sharp tip. The same procedure can be followed for resharpening, the tips. The following electrochemistry [18] governs the tungsten etching process.

CATHODE: $6H_2O + 6e^- \rightarrow 3H_2(g) + 6OH^-$

ANODE: $W(s) + 8OH^- \rightarrow WO_4^{2-} + 4H_2O + 6e^-$

COMPLETE : $W(s) + 2OH^- + 2H_2O \rightarrow WO_4^{2-} + 3H_2(g)$

In the above reaction, H_2 gas and WO_4^{2-} ions are released at cathode and anode respectively. After preparation, these freshly prepared tips are rinsed with ethanol and distilled water. These are then transferred in the chamber via the load-lock transfer arm for further preparation. Inside the chamber, the tips annealed by electron bombardment for removal of oxide layers. To check the shape and the sharpness of the tips, they are kept in front of phosphor screen. The collector screen is kept at high positive bias (2-5 kV) and a negative bias is applied to the tip. This negative bias is slowly ramped up till a pattern is observed. The lower the negative bias, the sharper are the tips you get.

Sharpness of the tip plays an important role in the resolution. A simple estimate assuming a parabolic tip done by Binnig *et al* [30], gives a resolution of 50 Å for a tip having 1000 Å radius.

2.2 Low energy electron diffraction

Since its invention in 1927, LEED[54, 200] has become a popular technique for quick characterization of ordered surfaces. It has been successfully applied for determination of unit-cell size, shape, structure and symmetry in materials. Low energy electrons are surface sensitive[1]. They have a small mean free path(5 Å), as they interact strongly with matter. This along with strong elastic backscattering from the ion cores ensures very small contribution from successive layers. The diffracted beams project a reciprocal map of the surface on to a phosphor screen (Ewalds sphere). The room temperature surface science chamber is equipped with Reverse View LEED Optics, manufactured by Princeton Research Instruments (PRI) model RVL 8-120, which is used in conjunction with PRI LEED electronics model 11-020. The LEED setup is shown in Fig. 2.6.

2.2.1 Construction and working

The LEED setup can be classified into three main components, namely: the electron gun, the detector and control system, and the electronics. The electron gun consists of a thoriated iridium

[1] An electron having an energy 100 eV has a De Broglie wavelength of 1.22 Å.

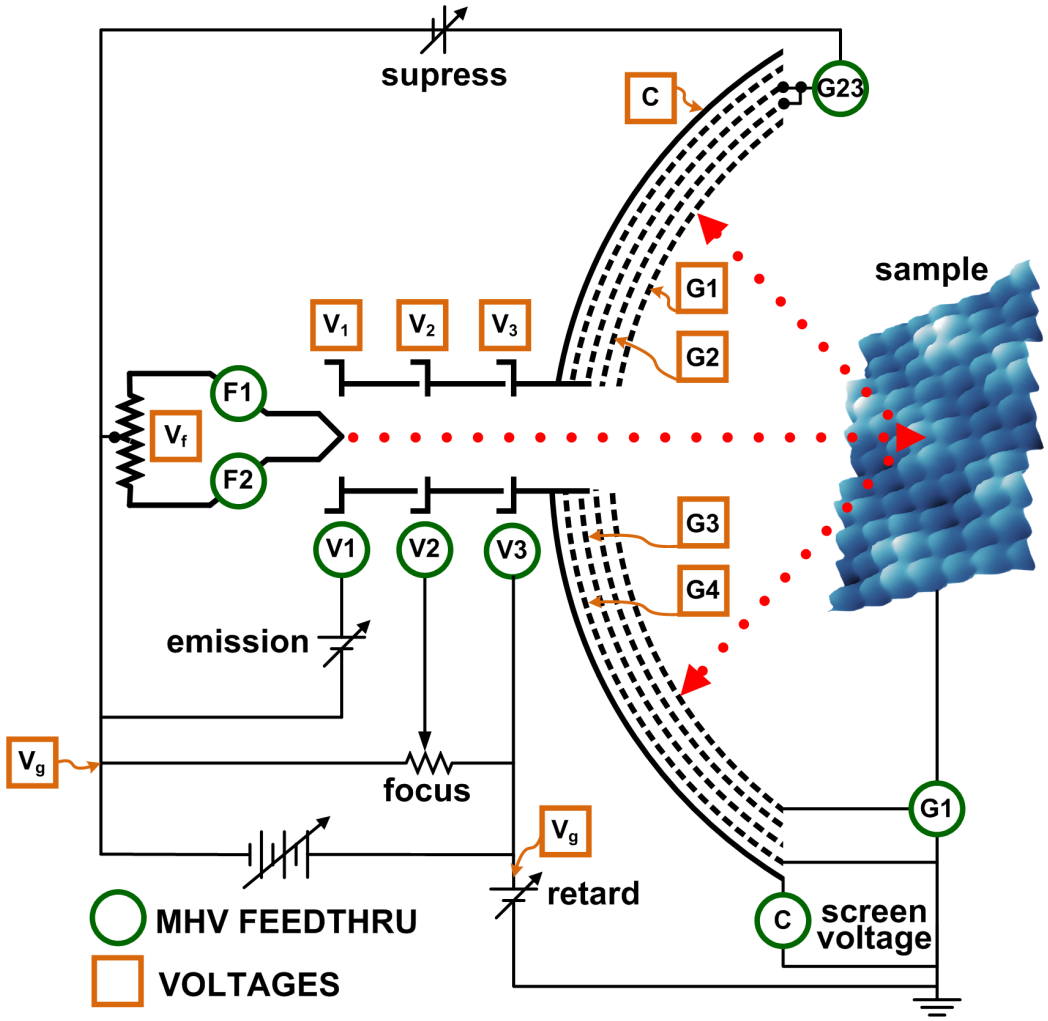

Figure 2.6: The diagram of the reverse view LEED optics princeton research instruments model RVL 8-120. The diagram is a reproduction of the figure in the instruction manual [3]. The setup consists of four hemishperical grids (*G1-G4*), electron gun (*F1* and *F2*) and optically transparent (SnO_2) collector screen. Grid G1 is grounded, G2 and G3 are suppressing grids for high pass filtering and G4 is the shield between the collector and suppressor grids.

(extremely resistent to burnouts) filament in an optically tight enclosure to eliminate optical interference from the filament. The filament connections are brought out through *F1* and *F2*. The detector and the control system has four hemispherical grids(*G1-G4*) along with a hemispherical glass collector (*C*) screen. Each of these grids have a hole for the electron beam. Under normal usage, grid *G1* is grounded by using an MHV shorting connector. The grids *G2* and *G3* are called suppressor grids and are tied together for superior high pass filtering capability. The grid *G4* is permanently grounded, and acts as a shield between the suppressor grids and the collector. The

collector screen is a biased at a potential of 2-5 kV. It is uniformly coated with optically transparent SnO_2, a phosphorescent material. The LEED electronics provides current to the filament and voltages to the grid and the collector screen.

The desired sample is placed at the common center of curvature of the grids perpendicular to the monoenergetic electron beam with variable energy (0-300 keV, typically). The typical beam size is 0.5 mm. The electrons get backscattered (elastically and inelastically) from the sample and emerge as diffracted beams in different directions with various intensities depending on the energy of the original beam. The beams traverse the distance between the sample and the grounded grid *G1* and pass thorough grids *G2* and *G3*. Voltages are applied to *G2* and *G3* in a manner that only the diffracted electrons having sufficient energy are allowed to pass through the grids, on to the grounded grid *G4*. In other words, the grid acts as a high pass filter that only allows the elastically backscattered electrons to pass. This double grid setup is a powerful method for contrast adjustment in LEED. These electrons get accelerated onto the collector screen by a high positive potential. A LEED pattern is observed on the LEED screen due to *phosphorescence* as the electrons strike the screen. The (00) pattern can be observed by tilting the sample.

2.2.2 Some remarks

There are experimental limitations on the coherence (10-20 *nm*) of the electron beam. Kinematic scattering theory assumes a single scattering event similar to the x-ray diffraction theory. A more complete multiple scattering theory takes into account multiple scattering events in the sample before the diffracted beam is projected to the screen. For advanced analysis a more sophisticated dynamical scattering theory is commonly utilized. Although multiple scattering theory is more applicable to LEED, kinematic scattering theory can be successfully applied for determination of unit-cell size, shape, superstructures, domains and symmetry determination. Slightly more involved analysis can provide qualitative information pertaining to domain size (spot size) and point defects density (background intensity). Multiple scattering theory, however, can be applied for unit cell determination. The advancement in the field of multiple scattering theories took place in 1960s with development of sophisticated programs and simultaneous development in both theoretical and

experimental fields. Essential components of the multiple scattering theory consist of ion core scattering, multiple scattering, inelastic scattering and temperature effects. There are achieving complex atomic form factors at work in electron scaterring. Multiple scattering events are first treated in the same layer and then for certain penetration depth. First, intensity vs energy information is extracted experimentally for LEED diffraction spots. Then these are compared with dynamical theory plots. This method is repeated a number of times for different presumed structure as an input for the dynamical theory until a minimum reliability factor (R) is obtained. Pendry R factor is the most commonly used reliability factor. A structure having R less than 0.2 is considered reliable. This methodology can predict structure with a 0.01 Å accuracy. This technique has played an instrumental role in providing structural and sample quality information during different stages of graphitization.

2.3 Auger electron spectroscopy

Auger electron spectroscopy (AES) is a useful surface science technique for detection and qualitative measure of chemical species present in a sample. The technique was developed in 1960s and named after Pierre Auger, a French physicist who discovered the process in 1925 while working with x-rays and a Wilson's cloud chamber [16]. The technique is based on Auger radiationless process. In this process an impinging electron beam doubly ionizes the atom by removing a core level electron, which may result in decay of the atom to a lower energy state by electronic transition. This transition releases energy which is transmitted to an ejected Auger electron. Figure 2.7(a) illustrates the KL_1L_3 Auger process. A high energy electron beam removes an electron from the core K shell leaving the parent atom in an excited state. Electronic rearrangement results into decay of an electron from L_1 shell to the K shell and the transition energy gets transferred to an electron in another shell L_3 which gets ejected from the atom. The ejected Auger electron is detected by energy analyzer and has kinetic energy characteristics of the parent atom.

2.3.1 Instrumentation

A typical Auger electron spectroscopy system consists of an electron gun for excitation and an energy analyzer for detection of the Auger electron peaks housed in an ultra-high vacuum. Our Auger electron spectroscopy setup consists of a single pass cylindrical mirror analyzer (CMA) PHI

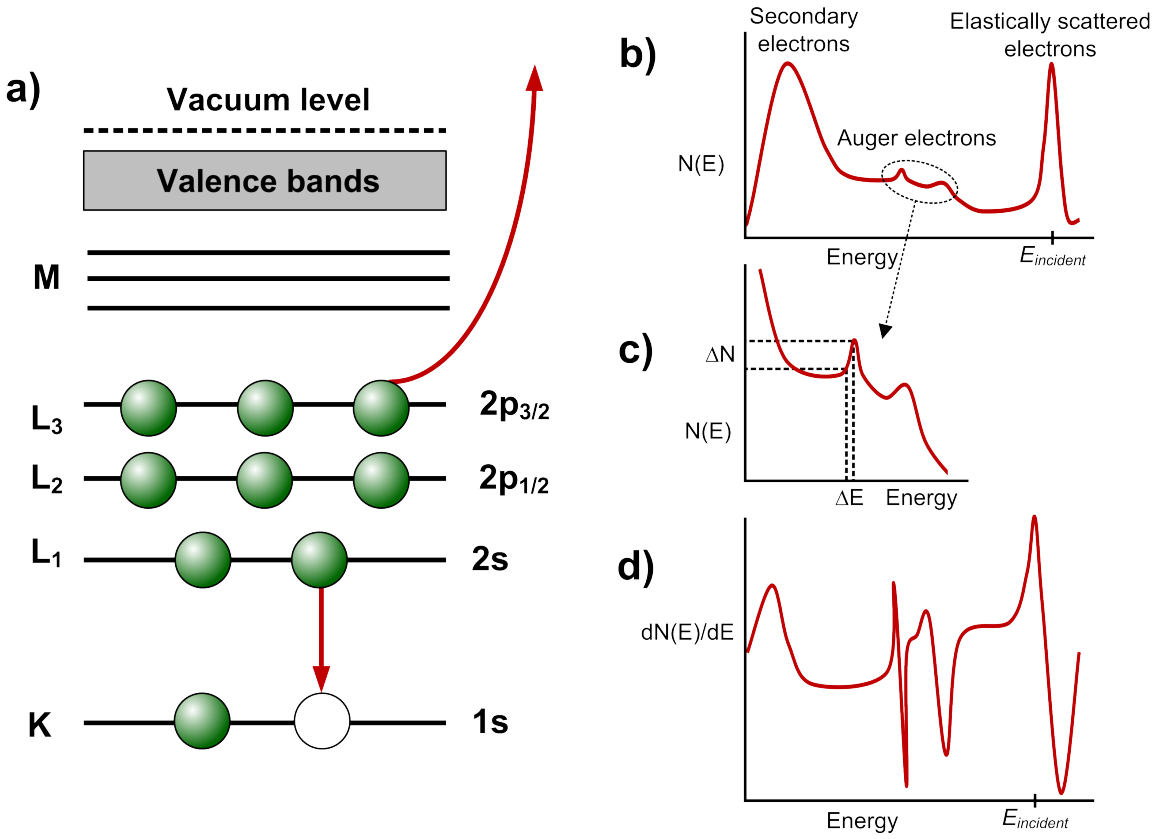

Figure 2.7: (a) An illustration depicting the typical KLL Auger process. A core (K) electron is removed by an impinging electron beam to be replaced by an electron from high energy state ($L1$). The released transition energy is transferred to an ejected Auger electron. (b) An example plot ($N(E)$ and incident energy E) demonstrating Auger peaks buried in a background of secondary and elastically scattered electrons. (c) Magnified plot of the region circled in (b). (d) Plot of d(N)/dE vs E showing enhancement in Auger peaks.

model 10-155, electron gun control PHI model 11-010, Auger system control PHI model 11-500 A, lock-in amplifier princeton applied research model 520 and a high voltage tennelec power supply make up our Auger electron spectroscopic setup (see Fig. 2.8 for a detailed schematic). Although, the retarded field analyzer (RFA) typically found in LEED setup has a larger solid angle for the detection of electrons it suffers from poor signal to noise ratio as it collects electrons above a certain energy unlike cylindrical mirror analyzer which does it for a certain energy range. The sensitivity of the Auger spectroscopy is influenced by the incident beam current and energy, transition probability of the Auger process involved and the collection efficiency of the analyzer. In order to get best focussing of the electrons CMA uses a takeoff angle of 42°(±3°) from surface normal. The CMA

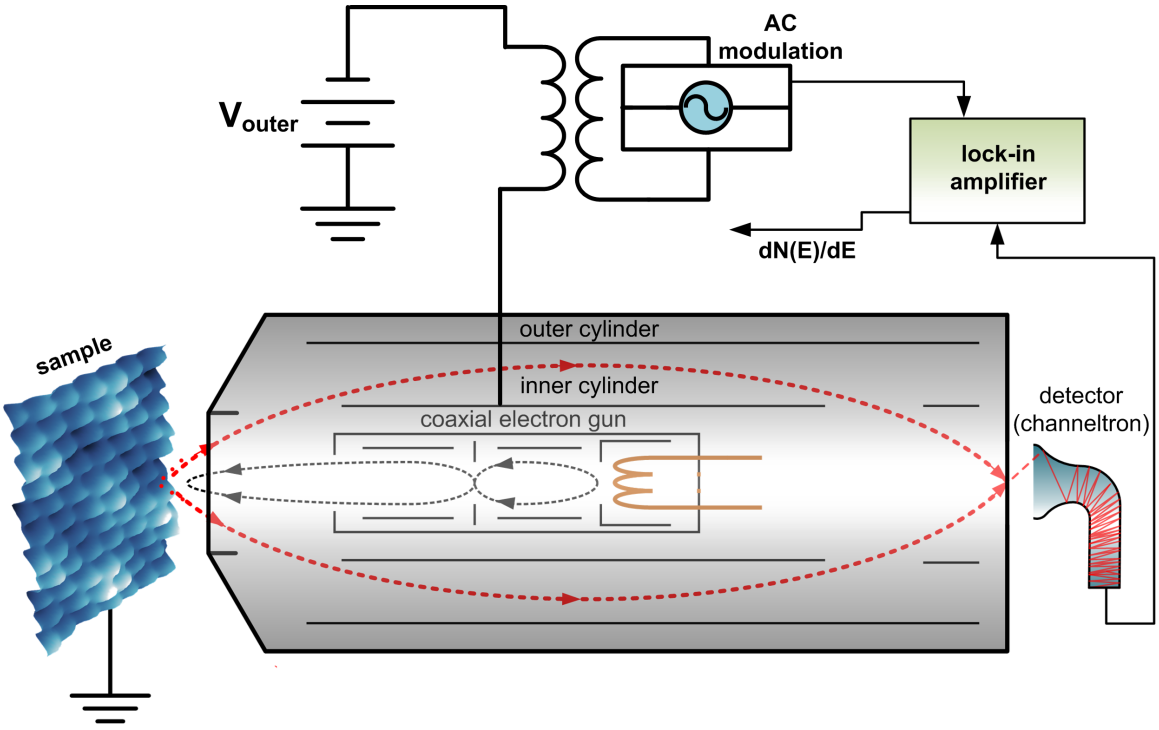

Figure 2.8: Schematic of the single pass CMA with electron gun and energy analyzer. Inner cylinder is kept at ground potential and a negative potential is applied to the outer cylinder. A take off angle of 42° from the sample is used for best focussing of electrons. Auger peak detection is done by Lock-in techniques.

is made up of two coaxial cylinders. The sample and the detector lie on the common axis of the two cylinders. A negative bias (V) is applied to the outer potential (radius r_2) and the inner cylinder (radius r_1) is kept at a ground potential. The potential difference between the two cylinders is given as,

$$V = \frac{E.ln(r_2/r_1)}{1.31e} \tag{2.12}$$

where e is the electron charge. Only the electrons that have energy E are deflected by the outer cylinder and focussed on the detector. The distance between the source and the focus is $6.1r_1$.

2.3.2 Modulation Technique

Auger electron peaks detected by the energy analyzer are superimposed on a large background. The detection process is greatly simplified by differentiation of electron energy distribution $N(E)$. The electronic differentation ($\frac{dN(E)}{dE}$) is accomplished with lock-in detection technique. This is realized

by superimposing a small a.c. voltage on the energy selecting voltage and detecting the output of the electron multiplier synchronously by a lock-in amplifier. Figure 2.7(b) shows the direct Auger spectra consisting of secondary, Auger and elastically-scattered electrons peaks. The relatively large background contribution is addressed by adding a small amplitude high frequency (10 kHz) voltage to the signal as illustrated in Fig. 2.7c. The Auger peaks are sharp compared to the background and electronic differentiation greatly enhances the S/N ratio as depicted in Fig. 2.7(d). The position of the elastically scattered electrons is marked in the Figures. 2.7(b) and 2.7(d).

This method is employed for average thickness determination of the epitaxial graphene. The Si and the C Auger peaks evolve as a function of thickness. A model based on the scattering cross-section and the relative intensity of the Si and C peaks is used for thickness estimation [55]. Carbon in the interface is also counted towards thickness in this model. This contribution has been estimated as 0.8-1 ML_e by x-ray reflectivity measurements [92] and is subtracted from the estimated average auger thickness. Sample Characterization and thickness estimation is described in detail in Sec. 3.2.

2.4 Raman Spectroscopy

Raman spectroscopy technique is based a subtle inelastic scattering of photons discovered by CV Raman in 1928 for which he won Nobel prize in 1930. The results were published [190] under the title *"A new type of secondary radiation"* . Raman employed mercury arc lamp as the optical source and monitored scattering of light from variety of different amorphous and crystalline sources. Development of this technique to be sold as a commercial package took a long time due to relatively slow advancement in the field of optics and signal detection. The field really took of after development and availability of lasers as a commercial package. At present there are a number of advance flavors of Raman experimental techniques such as surface enhanced Raman spectroscopy (SERS), hyper Raman, resonance Raman spectroscopy, spontaneous Raman spectroscopy, optical tweezer Raman spectroscopy (OTRS), stimulated Raman spectroscopy, spatially offset Raman spectroscopy (SORS), coherent antistokes Raman spectroscopy (CARS), Raman optical activity. These different techniques driven towards specific measurements.

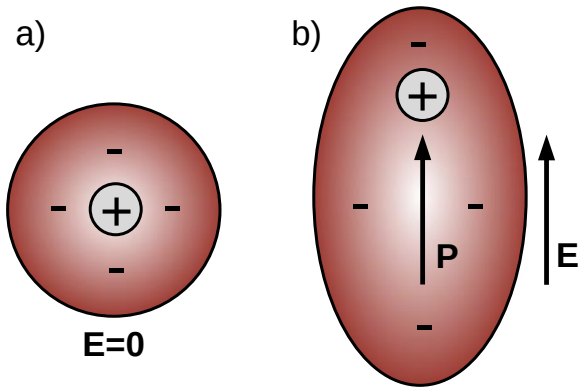

Figure 2.9: Polarization of an atom in an external electric field. (a) Electron cloud is uniformly distributed around the positively charged nucleus in the absence of external electric field. (b) Distortion of the electron cloud under an external electric field (E). The induced dipole moment P is proportional to the external electric field.

2.4.1 Theory of Raman Spectroscopy

In Raman scattering a small fraction (1 in 10^{6-7}) of the impinging photons from the light source (lasers etc.) inelastically scatter due to interaction with phonons of the vibrations in the lattice. This results in the energy of the photons being red- or blue-shifted. This Raman shift provides us information related to different phonon modes in the lattice. In red-shift mode, more commonly referred to as the Stokes shift the photon looses its energy to the lattice after the inelastic scattering process. On the other hand the photon gains energy in the blue-shift mode, commonly known as the anti-Stokes shift.

In Raman scattering process the inelastically scattered photons of the light are collected collected over a range of frequencies. This enables one to observe various phonon modes in the lattice. The scattering process is dominated by the Rayleigh scattering. An analytic expression for the scattered light can be obtained by employing classical electromagnetic theory. This will help us better understand the light-matter interaction and its relevance to the scattering process. Incident light(propagating EM wave) interacts with the atom in the lattice and induces an oscillating dipole moment p in the atoms (see Fig. 2.9).The dipole p of the material is related to the electric field E of the incident light by polarizability α (Equation xxx) which characterizes the polarization of an individual atom or molecule. The total polarizability α is the sum of the electronic (α_e), ionic (α_i) and dipolar (α_d) polar (Equation. 2.14) contribution.

$$p = \alpha E \tag{2.13}$$

$$\alpha = \alpha_e + \alpha_i + \alpha_d \tag{2.14}$$

Where,

$$E_i = E_o(\omega_i t) \tag{2.15}$$

In crystal lattice the atoms are constantly vibrating in and out of their equilibrium position due to thermal excitation. We can therefore expand the polarizability (α) using Taylor expansion series.

$$\alpha = \alpha + \left(\frac{\partial \alpha}{\partial Q_j}\right) Q_j + \left(\frac{\partial^2 \alpha}{\partial Q_j \partial Q_k}\right) Q_j Q_k + ... \tag{2.16}$$

Where Q_j are the normal vibrational modes of the lattice. We will retain only the first order term from the above expression. On assuming harmonic motion, the lattice vibrates at a certain phonon frequency.

$$Q_j = Q_j^o \cos(\omega_j t) \tag{2.17}$$

Where ω_j is the frequency of the j^{th} vibrational mode.

Combining Equation (2.1),(2.3)-(2.4) and retaining the first two terms of the polarizability expression.

$$E_f = \alpha_o E_o \cos(\omega_j t) + E_o Q_j^o \frac{\partial \alpha}{\partial Q_j} \left(\frac{\cos(\omega_i + \omega_j)t + \cos(\omega_i - \omega j)t}{2}\right) \tag{2.18}$$

Equation xxx represents an expression for the scattered light E_f that consists of Rayleigh and Raman scattering terms. The first term is the elastic or the Rayleigh scattering contribution. It is oscillating with the same frequency as the incident radiation. The next two terms $(\omega_i + \omega_j)$, $(\omega_i - \omega_j)$ represent the *anti-Stokes* and the *Stokes* Raman shift respectively. They represent the coupling of the incident light with the first resonance Raman mode of the lattice. Raman scattered photons energy shift depends on the vibrational state under study. In crystals only the phonons with a change in

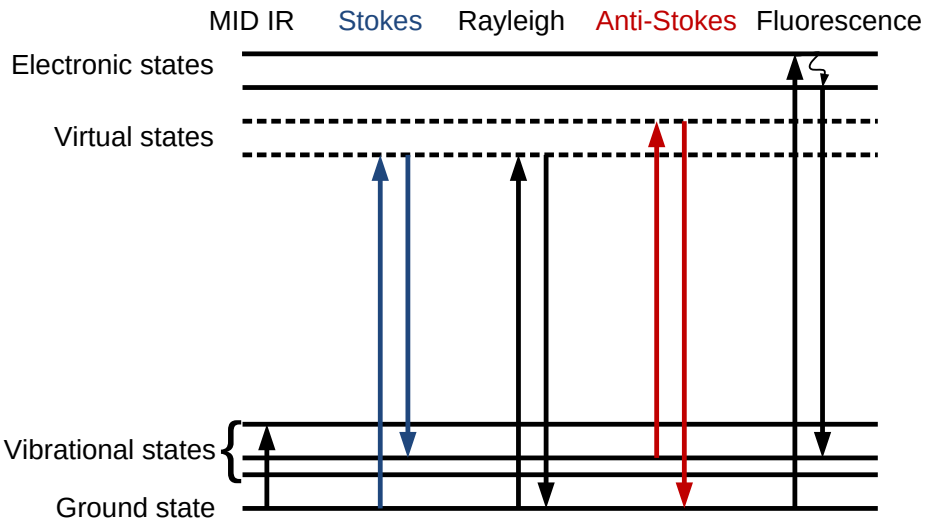

Figure 2.10: Illustration of different energy transition processes. Raman scattering can occur as Stokes or Anti-Stokes process.

polarizability are Raman active i.e. $\left(\frac{\partial \alpha}{\partial x}\right)_{eq} \neq 0$ where, eq is the equilibrium position and x is the normal coordinate. In graphene carbon-carbon double bonds with delocalized electrons are strong Raman scatterers. In the presence of an external electric field the electron cloud cover is easily distorted. The bending and stretching of bonds greatly modifies the electron distribution thereby inducing a substantial change in the polarizability α.

2.4.2 Instrumentation

The first Raman instrument was developed in 1928 [190]. In the experimental setup sunlight was passed through a telescope to obtain high intensity light source. This was then passed through a monochromatic filter and the human eye was the detector. Raman instrumentation has evolved a lot since the first experiments. First it was the use of mercury arc lamps and later the field really took off with the development of lasers, computers, rayleigh filters and detectors (like CCD's). These improvements enables one to obtain spectra relatively quickly with greatly enhanced signal to noise ratio with reliability.A dispersive raman setup has been successfully used in studying graphite based system because of its ability to select optimal wavelength to get best Raman information. Figure 2.11 shows essential components of a typical dispersive Raman setup. These are an optical microscope, Rayleigh filter, CCD detector, slit, excitation laser, spatial filter and diffraction gratings.

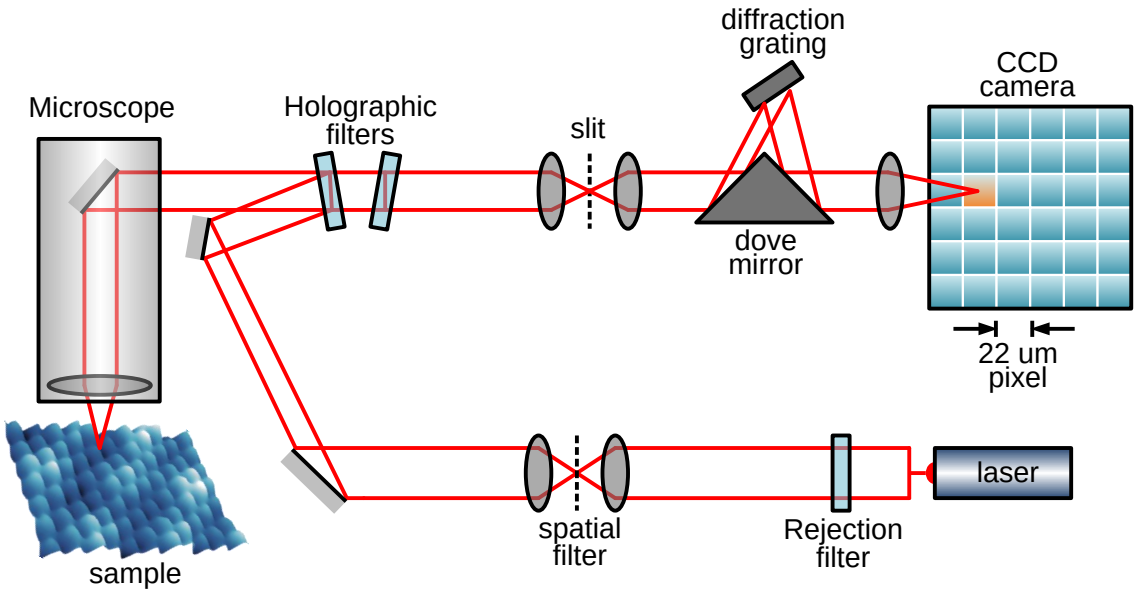

Figure 2.11: A schematic of a typical Raman spectrometer. The setup mainly consists of an optical microscope, Rayleigh filter, CCD detector, slit, excitation laser, spatial filter and diffraction gratings.

A monochromatic light beam is generated by the laser cavity. The power of the light beam is controlled by the rejection filter. Power of the incoming light plays an important role as it is directly related to counts and the signal-to-noise ratio of the Raman spectra. This beam is then focussed with spatial filters which removes higher order spatial modes. The focussed beam is then directed towards the microscope which has an objective lens for focussing the light on the sample. After scattering the inelastic and the elastic radiations are captured by the objective. Raman scattering process is nearly a million times less intense than the elastic Rayleigh scattering. This elastically scattered component is removed by holographic filters. This is followed by slit lenses setup that consists of a pre-slit lens, adjustable lens and a post-slit lens. The pre-slit lens focuses the image on the adjustable lens that determines the resolution of the Raman system. The Raman is then collimated by the post-slit lens and passed through the diffraction grating which resolves discrete wavelengths. The signal is then collected via a CCD camera. The spectral resolution of the setup is governed by the slit width and is a product of slit width and the dispersion.

CCD detectors are made up of photosensitive material and acts as a shift register to hold and transport analog signals controlled by external clock signals. The photoactive region is an epitaxially grown doped (p^{+}) Si on p^{++} doped substrate. The CCD cameras used in Raman setups have a typical

Figure 2.12: Reinshaw RF1000 Raman spectrometer at School of Materials Science and Engineering, Georgia Tech.

size of 22 μm. CCD's have a high quantum efficiency i.e. the ability to convert incident photons into photoelectrons. The allows usage of low power settings and provides high signal-to-noise ratio. The dispersed beam has vertical spread across horizontal line of pixels. These are summed/binned to integrate each signal. Finite size of the CCD has an impact on the spectral range/resolution. The size of image, focussed on the CCD can be proportional to the slit width. The resolution of the spectra can be improved by decreasing the slit width which makes the focussed image on the CCD smaller.

CHAPTER III

GROWTH IN ULTRA HIGH VACUUM

In this chapter I will discuss graphene growth on the 6H-SiC(0001) under UHV conditions. In this thesis research more than 50 different H_2 etched SiC(0001) samples were graphitized under UHV environment. Almost all of the samples were characterized by Auger electron spectroscopy (AES) and low energy electron diffraction (LEED) and more than half were studied with scanning tunneling microscopy (STM) after graphitization. The samples were grown under varying conditions of temperature, pressure and annealing time.

3.1 Sample Preparation

In this section graphene growth is investigated for the samples grown on the Si- face of the bipolar SiC crystal in ultra-high vacuum (UHV). The 6H-SiC polytype was purchased from Cree, Inc. [6] for graphene growth. The 3" wafer was diced into smaller samples of size 3 mm $\times$ 4 *mm* at the clean room facilities of Microelectronics Research Center (MiRC) at Georgia Tech. The 6H-SiC samples are doped *n*-type with a resistivity of 0.05 Ω-cm, in order to have sufficient conductivity for STM measurements. The wafer in its native form has a lot of defects and scratches (~10 nm deep) due to mechanical polishing (see Fig. 3.1(a)). This not an ideal template for graphene growth. It has been shown that the H_2 etching process can remove scratches from SiC surface [36, 48, 61, 85, 86, 174, 223, 224]. Prior to H_2 etching the samples are ultrasonically cleansed in sequential baths of ethanol and acetone for 10-15 minute each. The SiC samples are then heated in a home built RF furnace in an atmosphere of 5% H_2 and 95% Ar to 1300-1650 °C . Figure 3.1 shows the changes in the morphology of SiC from H_2 etching process at different temperatures. The process ends with an array of atomically flat terraces (see Fig. 3.1(d)) separated by 7.5 or 15 Å steps corresponding to half unit cell and unit cell height of 6H-SiC. The width of the terraces is determined by the miscut angle of the wafer. Although H_2 etched samples provide an ideal template for graphene growth there is an intrinsic problem of oxides on the sample after transfer through atmosphere [26, 27]. These can typically be removed by heating the samples under UHV environment to 1000-1100 °C.

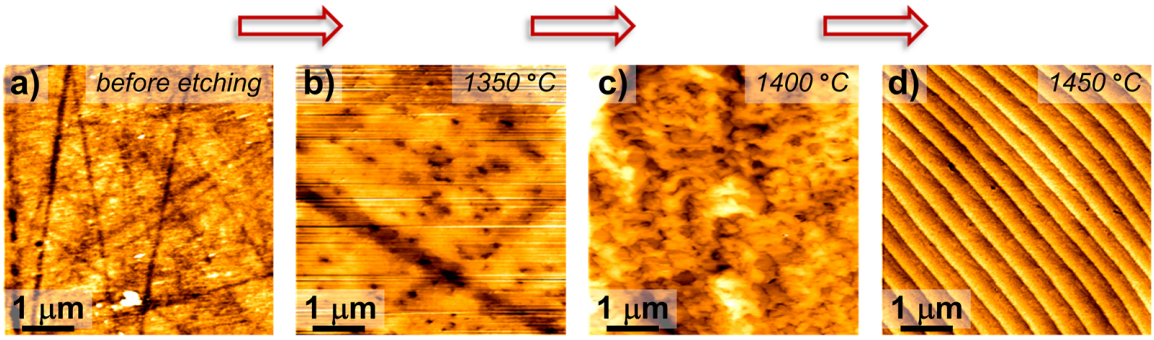

Figure 3.1: AFM images of progression of the surface morphology as a function of temperature during the H_2 etching process of 6H-SiC. (a) 5 $\mu m \times 5$ μm AFM image showing scratches on the SiC wafer due to polishing process of the manufacturer. (b) and (c) show smoother topography during the H_2 process at 1350 and 1400 °C, respectively. (d) A stepped (7.5 or 15 Å) array of SiC terraces after H_2 etching. Terrace width is determined by the miscut of the wafer.

The Si-face is identified by cutting away a small piece of SiC from the bottom left corner with a diamond scribe prior to H_2 etching.

These samples are mounted on a molybdenum sample holder (see Fig. 3.2(a)) with a hole in the center for direct exposure to the electron-beam heater. Figure 3.2(a) shows a SiC sample supported by tantalum tabs at the bottom (A) and secured with spot welded tabs (B) at two diagonally opposite corners. The samples are transferred into the RT system via a load-lock setup that can accommodate two samples and four STM tips. This section is pumped down to a pressure of $< 1 \times 10^{-8}$ Torr with a turbomolecular pump. At this stage, the load-lock valve is opened, and the samples along with the tips are transferred into the chamber by an magnetically coupled translation stage. *In situ* manipulation of the samples and the tips is done via customized wobble sticks located at two opposite ends of the chamber (load-lock/STM) . The jaws of the wobble stick lock around the ball shaped end (C) of the molybdenum sample holder. The sample is next transferred either to the sample manipulator (see Fig. 3.2(b)), or the sample parking carousel. The sample manipulator is capable of motion in the three translational directions, and one rotational direction. An electron beam heater is mounted at the end of the manipulator for sample preparation and thermal cleaning. A hole in the center (D) and the conical shield (E)(see Fig. 3.2(b)) ensures that majority of the electrons are collected by the sample.

Samples placed on the manipulator are graphitized by heating them to a temperature above

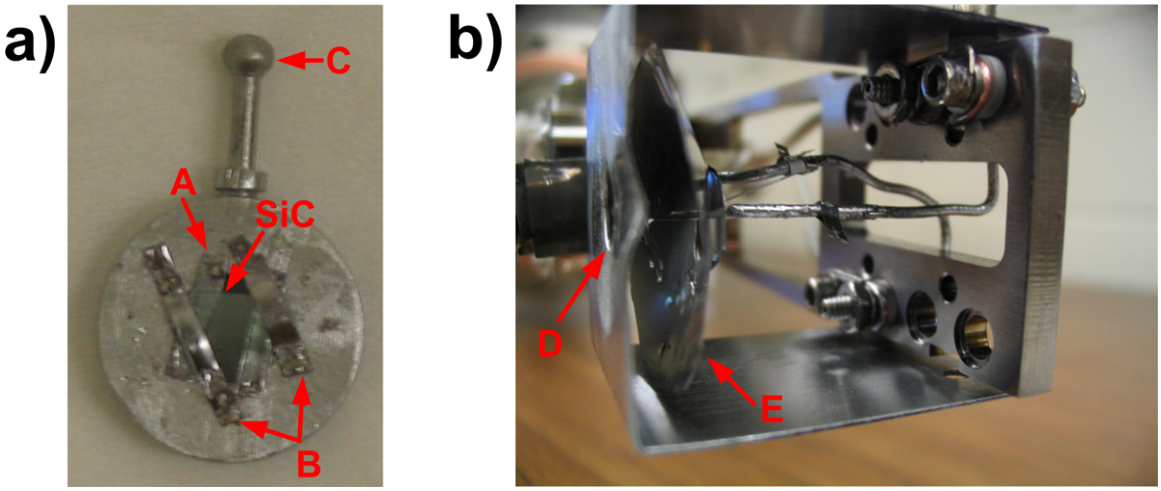

Figure 3.2: (a) Sample is mounted on molybdenum sample holder with tantalum tabs. The ball shaped end is useful for *in situ* manipulation of the sample with a wobble stick. (b) Electron beam equipped sample manipulator (end view).

1250 °C by electron bombardment. The temperatures are slowly ramped up to the desired final temperature in steps. Temperatures are held constant at predetermined values corresponding to different phases (discussed in Sec. 3.2) for approximately 5 minutes. Graphene films begin to form near 1250 °C. Under UHV conditions, at such temperatures the Si desorbs leaving behind C atoms that rearrange naturally to form graphene films. The thickness of the graphene films is varied by changing the final annealing temperature and (to a lesser degree) time. The final annealing temperature is kept below 1450 °C to prevent formation of a eutectic between the SiC and Mo sample holder. A Thermionics power supply generates the necessary filament current and the high voltage. The power settings during operation depend on the desired temperature during the graphitization process. The filament (W, 0.008") was typically operated at 4.5-5.2 A and the high-voltage between the filament and the sample was varied from 0.3-0.75 kV to achieve the desired emission current and total power. Temperature is measured via an optical pyrometer at the corner of the sample above the tantalum tab.

3.2 Thickness Measurement and Initial Characterization

Prior to graphitization, the H_2-etched SiC samples are characterized by Auger electron spectroscopy (AES) and low energy electron diffraction (LEED). The H_2-etched SiC samples have a natural buildup of oxide on the surface although faint SiC ($\sqrt{3}\times\sqrt{3}$)R30° LEED spots were seen on most

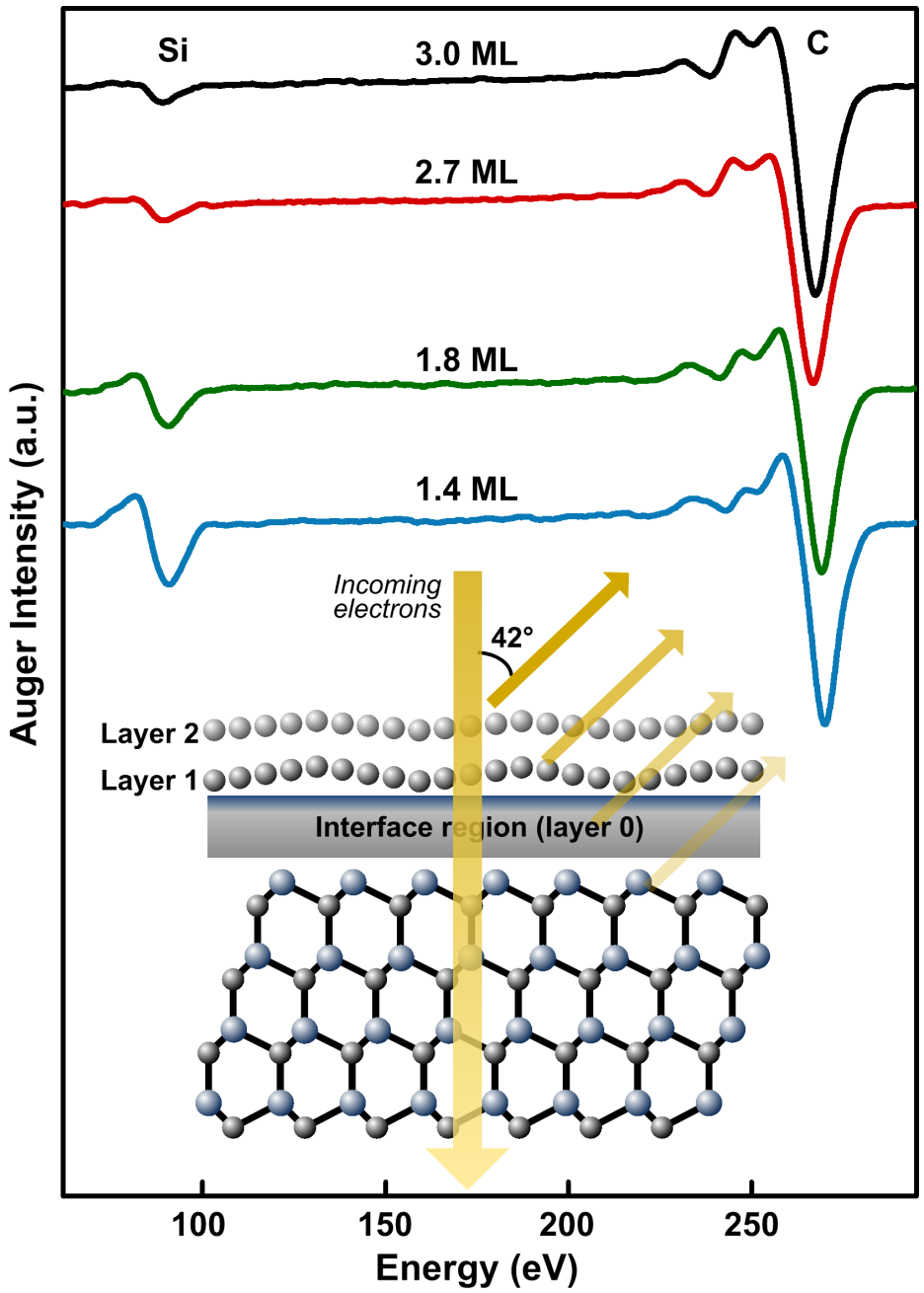

Figure 3.3: Auger spectra of four different thickness (see Fig.) samples. Changes in the spectral shape and intensity are seen for C(1s) and the Si(2p) as a function of thickness. Inset shows our present understanding of the EG/SiC(0001) material system along with our Auger attenuation model. In this system, an interface exists sandwiched between overlying graphene layers and the SiC substrate.

of the samples prior to heating. Starke *et al* [201] suggested that this monolayer coverage of oxide layer exists as Si_2O_3 on SiC(0001). In my experiments the oxide layer was found to be stable upto

1050 °C, which was confirmed by AES.

Initial characterization of the samples after graphitization is done via AES and LEED. Figure 3.3 shows the Auger spectra for four different thickness EG/SiC(0001) samples and a schematic of our present understanding of this system, to be discussed further in Chapter. 5 Changes are observed in the shapes of the Auger spectra, and in the relative intensities of the Si(2p) and C(1s) features as a function of annealing temperature. The Si and C peaks are observed at 92 and 272 eV, respectively. The effective thickness of the EG film is estimated using an attenuation model of the Si:C Auger intensities [55, 127]. The model incorporates only depth-dependent changes in the density of C and Si atoms; it is insensitive to details of the in-plane atomic arrangements at any depth. Several studies suggest that the interface could be carbon rich [63, 92, 100, 229] with silicon adatoms [92, 197]. Consequently, the model overestimates the EG thickness since the carbon in the interface region contributes to the overall thickness (~1 ML_e). The film thicknesses reported in this thesis are graphene-equivalent monolayers (ML_e) that include the contribution from the interface layer, which will be shown to contain 0.8-1 ML_e of carbon (Chapter. 6).

LEED is routinely used as tool for quick characterization of EG/SiC(0001) samples. The quality of the sample is gauged by the sharpness of the LEED spots and the background diffuse. Figure 3.4(b) shows a LEED pattern of a 2.7 ML_e sample. In addition to the graphene (green arrows) and SiC spots (red arrows), $(6\sqrt{3}\times 6\sqrt{3})R30^\circ$ diffraction spots are indicated in the image by blue arrows. Also evident in this figure is the epitaxial registry of the graphene lattice relative to underlying SiC substrate. There exists several commensurate SiC unit cell structures with different rotations relative to the graphene lattice [70, 126, 176, 191, 210]. On $(6\sqrt{3}\times 6\sqrt{3})R30^\circ$ commensurate unit cell, graphene lattice can overlay with 30° and ±2.2° rotations relative to SiC$[10\bar{1}0]$ direction with a strain of 0.15% [90]. In my experiments EG on Si-face the $6\sqrt{3}$ reconstruction was always found to exhibit a rotation of 30° relative to the $[10\bar{1}0]$ direction of SiC, in agreement with previous work [70, 176, 210].

Temperature (°C)	Reconstruction (with respect to SiC)	Si flux	Reference
-	(1 × 1)	-	[100, 127, 176]
950-1150	($\sqrt{3}\times\sqrt{3}$)R30°	Both	[71, 102, 125]
~850	(2 $\sqrt{3}\times$6 $\sqrt{3}$)R30°	Yes	[125]
~850	(3×3)	Yes	[71, 102, 125]
~850	(7×7)	Yes	[125]
>1150	(6 $\sqrt{3}\times$6 $\sqrt{3}$)R30°	Both	[71, 210]
>1150	(5×5)	Both	[191]

Table 3.1: Various reconstructed phases (in Wood's notation) observed on SiC(0001) prior to graphitization.

3.3 Surface Reconstructions of SiC(0001)

SiC goes thorough several different reconstruction phases prior to graphitization (Table. 3.1 for a list of SiC reconstructions). The graphitization of hexagonal SiC crystals was first studied by vanBommel *et al* [210] in 1975. They investigated the reconstruction phases of SiC from 250-1500 °C with LEED and AES. They found a carbon rich surface on SiC with varying reconstructions phases between 1000 and 1500 °C. Starting with a ($\sqrt{3}\times\sqrt{3}$)R30° at 250 °C they observed (6 $\sqrt{3}\times$6 $\sqrt{3}$)R30° reconstruction at 800 °C and graphite spots (1×1) at 1500 °C. They also observed a transition of the C peak in the Auger spectra from carbide-like to graphite-like at temperatures above 800 °C.

In several studies that followed vanBommel's work, external Si flux was used to compensate for the Si depleted environment created during SiC annealing. Prior to an exposure to the Si beam, ($\sqrt{3}\times\sqrt{3}$)R30° reconstruction is seen [71, 102, 125] on heating the samples to temperatures above 900 °C. This surface reconstruction is believed to be Si depleted [125]. A Si flux deposition at 850 °C results in a Si-rich (3×3) reconstruction, which has been observed in LEED [102] and STM [125] measurements. Li *et al* [125] found several other intermediate phases with STM that were not observed in LEED studies. They found that on depositing Si at 850 °C the ($\sqrt{3}\times\sqrt{3}$)R30° reconstruction changes from (2×2) to (2 $\sqrt{3}\times$6 $\sqrt{3}$)R30° reconstruction. This reconstruction transforms to (3×3) with more Si deposition. On further depositing Si, a (7×7) Si-rich reconstruction phase is observed.

On heating the samples to temperatures above 1100 °C, ($\sqrt{3}\times\sqrt{3}$)R30° and (6 $\sqrt{3}\times$6 $\sqrt{3}$)R30°

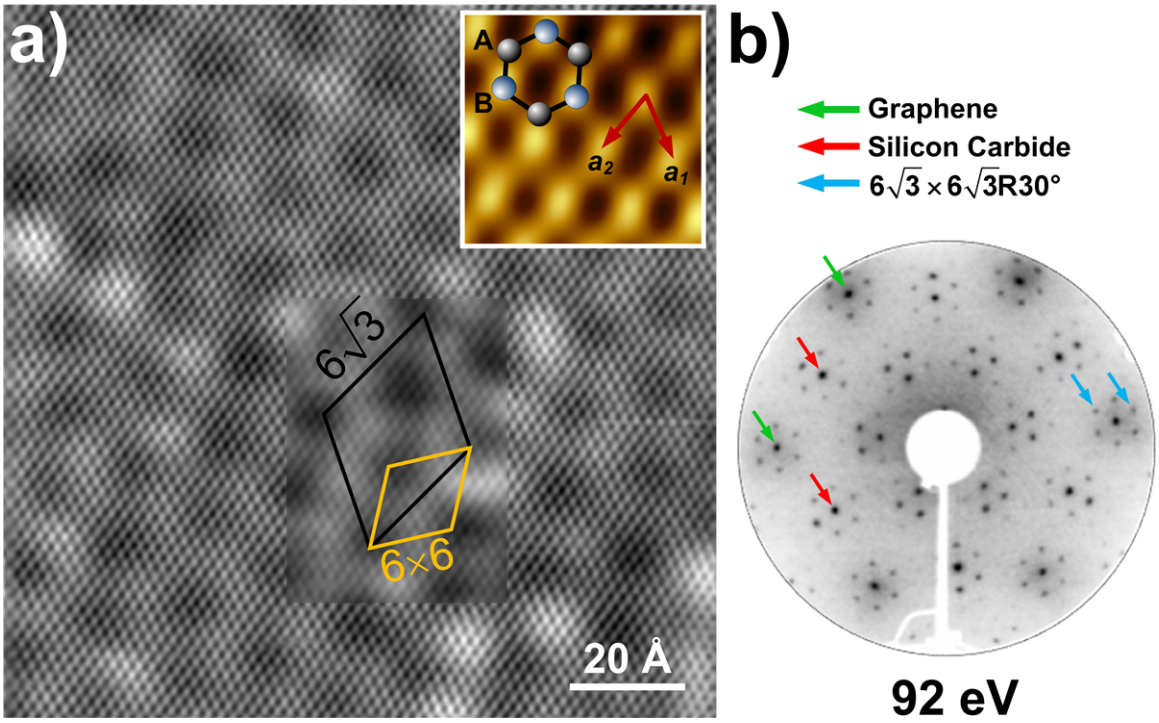

Figure 3.4: Terminology in epitaxial graphene. (a) High resolution (120 Å × 120 Å) image showing layer 2 graphene rotated 30° relative to SiC(00$\bar{1}$0) (0.3 V, 100 pA). The bigger period of (6 $\sqrt{3}$×6 $\sqrt{3}$)R30°(white diamond) is due to graphene lattice blanketing over interfacial features. The quasi period of (6×6) is represented by yellow diamond. Inset shows the trigonal lattice with every other atom represented by graphene lattice vectors *a1* and *a2*. The hexagon represents approximately the location of A and B atoms. (b) Grayscale LEED image of the sample at 92 eV showing SiC (red arrows), graphene (green arrows) and (6 $\sqrt{3}$×6 $\sqrt{3}$)R30° (blue arrows) spots.

phases coexist in the form of a mixed reconstruction. The ($\sqrt{3}$× $\sqrt{3}$)R30° are seen upto 1150 °C with LEED, after which only the (6 $\sqrt{3}$×6 $\sqrt{3}$)R30° phase is seen. In my experiments, in the absence of Si flux I have observed ($\sqrt{3}$× $\sqrt{3}$)R30° and (6 $\sqrt{3}$×6 $\sqrt{3}$)R30° reconstruction phases prior to graphitization at temperatures similar to the ones listed aboves.

3.4 Graphene Terminology

Figure 3.4(b) shows a high resolution image of layer-2 (layer 2 in Fig. 3.3) epitaxial graphene. Along with graphene which is imaged as a trigonal lattice, a bigger period of (6×6) periodicity (yellow diamond) is observed superimposed on the lattice. This is due to the draping of the graphene lattice over the interfacial features (see Chapter. 5). However, the true reconstruction unit cell is (6 $\sqrt{3}$×6 $\sqrt{3}$) as can be shown in the LEED pattern of Fig. 3.4(b). The LEED reciprocal space map

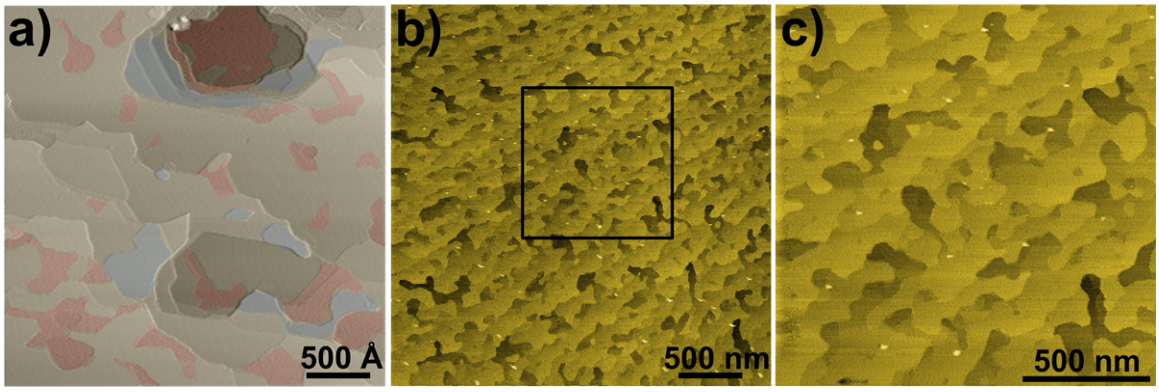

Figure 3.5: EG growth on SiC(0001) under UHV environment. (a) 3000 Å × 3000 Å image of a UHV grown EG on SiC(0001) showing a topography dominated by SiC steps, smaller domains and pits extending to the substrate (-3 V, 100 pA). Layers 0 (red), 1 (yellow) and 2 (blue) are identified based on roughness (b) 1.2 ML_e sample prepared by flash-annealing to 1200 for 10s. The 3 μm × 3 μm shows high density of pits at early stages of growth (-3 V, 100 pA).(c) 1.5 μm × 1.5 μm magnified image of black boxed region in (b) (-3 V, 100 pA).

taken at 92 eV shows the graphene (green arrows), SiC (red arrows) and 6 $\sqrt{3}$ (blue arrows) satellite spots. Previously 6 $\sqrt{3}$ superperiod was believed to be caused by a Moiŕe effect [71]. The (6×6) quasi unit cell (yellow diamond) is often used to address the superperiod seen in the EG lattice. Inset in Fig. 3.4(a) shows the trigonal lattice where every other atom is imaged. The hexagon represents the location of the A (grey) and the B (blue) atoms. The graphene lattice vectors are represented by $\overrightarrow{a_1}$ and $\overrightarrow{a_2}$.

3.5 Growth in UHV

Epitaxial growth of graphene films on SiC(0001) has been experimentally investigated [45, 71, 100, 135, 176, 210] for decades. The density of carbon atoms in three SiC bilayers is 3.67×10^{15} atoms/cm^2 compared to 3.8×10^{15} atoms/cm^2 in a graphene layer. Therefore, ~3.14 SiC bilayers produces enough carbon atoms for the formation of graphene honeycomb lattice. Heating SiC(0001) in UHV environment to temperatures above 1200 °C results in desorption of Si atoms from the surface. This creates a carbon rich environment and at such elevated temperatures diffusing species can nucleate effectively at the low energy sites, but the details of this process are unknown. Graphene has been shown to grow on both Si- and C-face of SiC. However, there are some fundamental differences in the growth process due to difference in stacking of Si and the C atoms on the two faces.

On the Si-face graphene growth is considerably slower compared to the C-face and mostly depends on the annealing temperature. On the other hand growth on the C-face is a function of both the annealing temperature and time.

Figure 3.5(a) shows a 3000 Å × 3000 Å topograph of a typical UHV grown sample on SiC(0001). The sample is 2.5 ML_e thick. The topography is dominated by SiC steps, smaller domains with complex geometrical structures, and deep pits. Even though the topmost graphene layer always appears continuous in high resolution STM imaging, substrate steps apparently seed many transitions in graphene layer thickness. As seen previously (Fig. 3.1), H_2 etching process results in an array of large (~1-2 μm) regularly spaced terraces. However, a substantial amount of SiC roughening takes place during the growth as evident in the image and terraces are observed to be much smaller. In Fig. 3.5(a) different layers can be identified based on roughness, namely: layer 0 (red), layer 1 (yellow) and layer 2 (blue). This roughness is due to the blanketing effect of the graphene lattice over the interface states seen in layer 0, and it decreases with subsequent layers. The electronic and structural properties of these layers along with some other unique properties are discussed in detail in Chapter 5.

Pit formation in the SiC substrate takes place in the early stages of graphene growth [87], which creates a high density of steps where graphene may nucleate. Figure 3.5(b) shows a large 3 μm × 3 μm survey scan of a 1.2 ML_e sample with a high density of pits. The sample was prepared by flash-annealing to 1200 °C for 10 s. As mentioned previously, the Auger attenuation model counts the carbon in the interface (~1 ML_e) towards thickness. Therefore the sample has nearly 0.2 ML_e coverage of layer 1 and is mostly covered by layer 0 ($(6\sqrt{3}\times 6\sqrt{3})R30^\circ$ reconstructed SiC). It has been suggested that growth starts locally at random locations on the step edges and the terraces remain intact [87]. Similar behavior can also be observed in Fig. 3.5(c) which is a magnified image (1.5 μm × 1.5 μm) of the region enclosed by the black box in Fig. 3.5(b). It is possible that as the growth progresses at random locations, there are non-uniformities in $(6\sqrt{3}\times 6\sqrt{3})R30^\circ$ films. If the growth is continued then the steps below will start decaying, leading to pit formation. Island-like features are also observed in Fig. 3.5(c) which suggests that carbon can diffuse freely on the terraces. Some particle like features can also be seen in the image. Their origin and role during the graphene growth could not be established. Hannon *et al* [87] studied graphene growth on SiC(0001) with low

energy electron microscopy (LEEM). They found that pit formation takes place at low temperatures (~1140 °C) during the growth. They discovered two primary factors that lead to formation of pits, which are: (1) The relative stability of the interface layer in a SiC environment, and (2) The SiC steps get pinned at the interface layer domains. The decomposition of the SiC surface takes place at the steps which causes the steps to retract around the interface layer. They also found that on annealing the sample to a higher temperature (~1200 °C) graphene nucleates in these pits due to a high density of steps.

During the growth the Si released at the interface can either diffuse out laterally or through the graphene films to the vacuum [132]. In my STM measurements I have identified locations that could potentially act as a "venting" site for Si. Fig. 3.6(a) shows a 1050 Å × 1050 Å a region of layer 0 (bottom right) in the middle of a layer 1 terrace. The sample has a low coverage with a thickness of 1.8 ML_e. On careful inspection (see inset), it can be observed that a "tear" (white arrow) runs through the graphene, passing through the region of layer 0. This suggests a possible growth mechanism where individual graphene sheets come together to form bigger films at elevated temperatures. Such regions of discontinuity in the middle of the terraces were not seen on the thicker samples that were annealed to higher temperatures (>1300 °C). These voids of layer 0 could act as venting sites for the Si released at the interface during growth. The carbon that remains behind could connect to the larger graphene sheets, thereby closing the gap at elevated temperatures. Figure 3.6(b) shows a high resolution magnified image (230 Å × 200 Å) of the layer 0/layer 1 region in (a) (red arrow). In layer 0, trigonal features are observed (green circle), which are thought to be due to pyramidal "tetramers" of Si or C/Si (see Chapter 5). Furthermore, in this empty states image acquired at +1 V, layer 1 does not image as a honeycomb lattice. At high bias (see Chapter 5), graphene becomes transparent and interfacial features (orange circle) similar to the ones observed in layer 0 are seen. This electronic effect is due to partial hybridization of SiC dangling bonds with graphene bands [197].

Another potentially interesting region in (a) (blue arrow) is magnified and shown in Fig. 3.6(c). A (5×5) reconstruction (black diamond) is observed within this island. This reconstruction exists in the form of cluster-like species with varying number of atoms. In my STM studies, I have observed a small fractional coverage of the (5×5) reconstruction occurring alongside ($6\sqrt{3}\times 6\sqrt{3}$)R30°. The

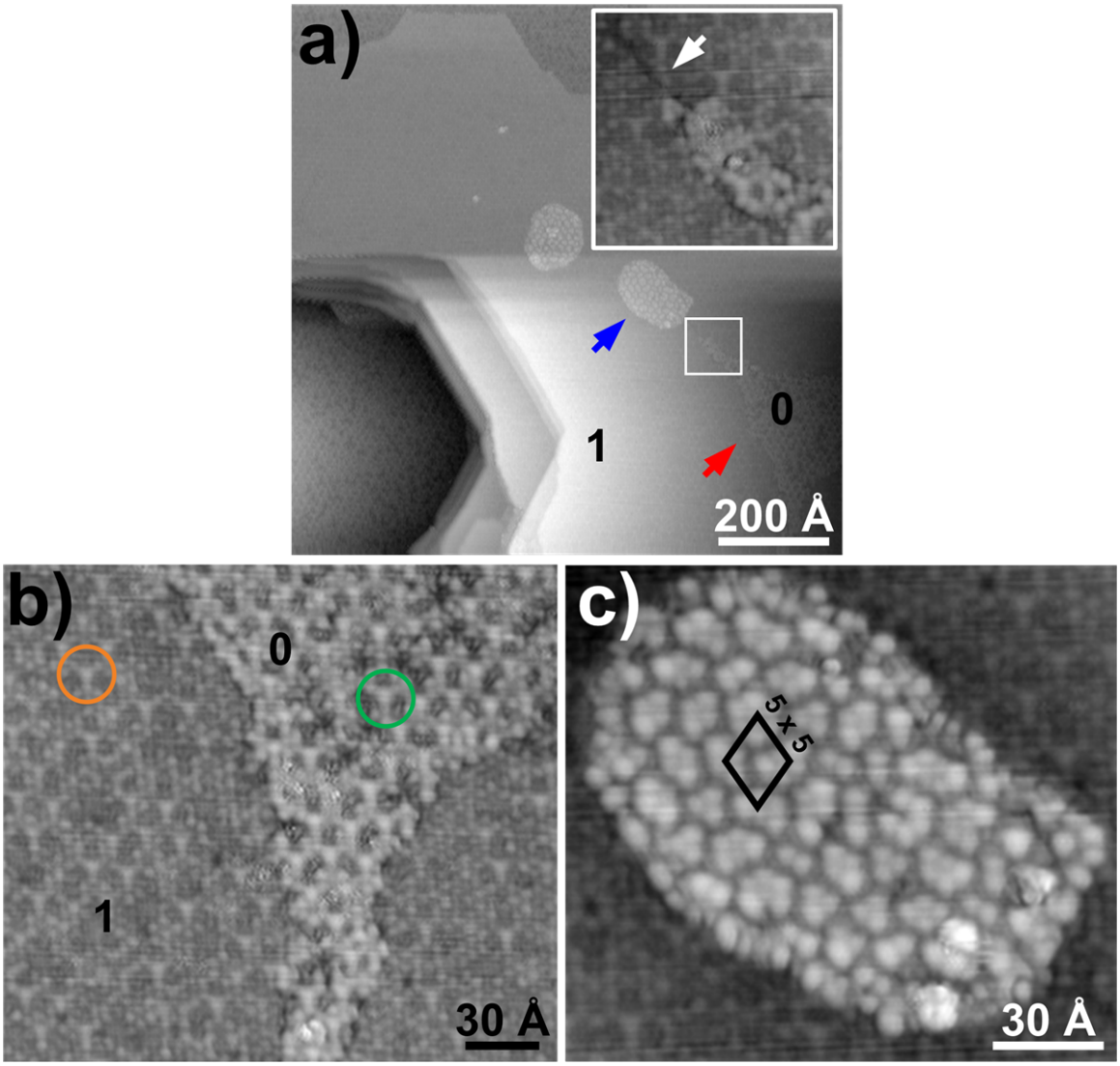

Figure 3.6: (a) 1050 Å × 1050 Å image of 1.8 ML_e thick sample (1 V, 100 pA). The image shows island-like features (blue arrow) and a layer 0 (red arrow) patch on layer 1 terrace. Inset is a magnified image (120 Å × 120 Å) of white boxed region in (a) showing a tear (white arrow) in layer 1 graphene. (b) 230 Å × 200 Å high resolution image showing interfacial features in layer 0 (green circle) and layer 1 (orange circle) (1 V, 100 pA). Interfacial features are imaged through layer 1 at high bias (see Sec. 5.1.2). (c) Magnified image (160 Å × 130 Å) of the island in (a) (blue arrow) showing (5×5) reconstructed clusters (black diamond) with varying number of atoms (1 V, 100 pA).

(5×5) islands were found to be even less common than patches of (5×5) regions. I believe the reconstruction is a deviation from the $(6\sqrt{3}\times 6\sqrt{3})R30°$ caused due to some local strain related perturbation during the growth. In Fig. 3.6(a) the (5×5) island is observed to lie close to a patch of layer 0, suggesting that it became stable near the layer 0 site with out undergoing any further phase change. This reconstruction has been reported by other groups [176, 191]. Owman *et al* [176]

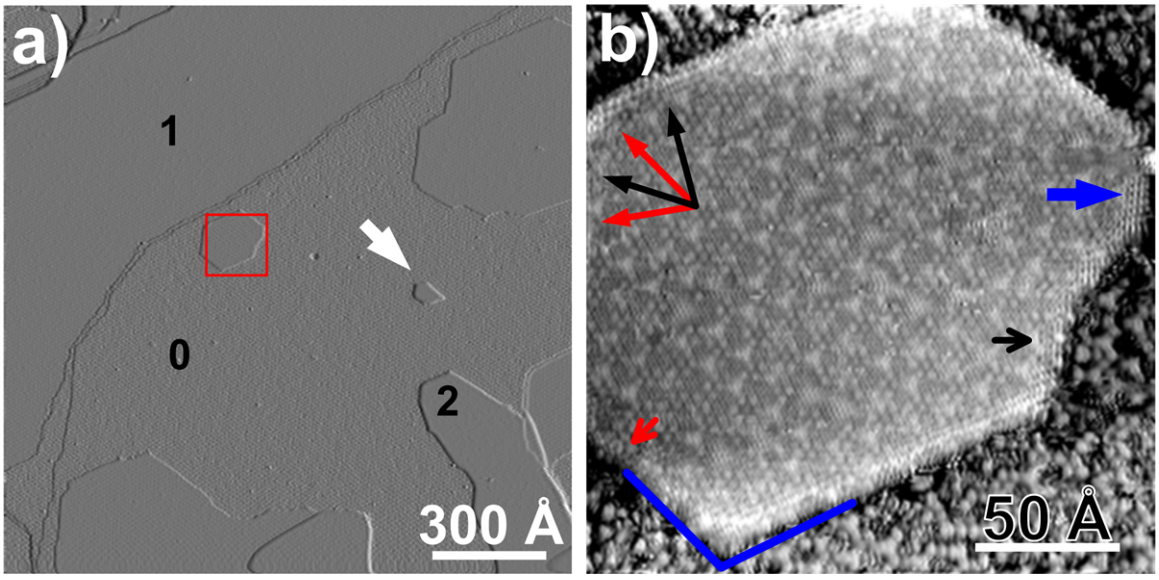

Figure 3.7: Electronic properties of layer 1 graphene islands is dominated by SiC substrate. (a) 1500 Å × 1500 Å gradient enhanced image showing layer 1 (red box) and layer 2 (white arrow) graphene islands in layer 0 (1 V, 100 pA). Different layers are identified by the roughness of the terraces. (b) High resolution 200 Å × 200 Å image of graphene island shows trigonal interface features and graphene lattice at 0.2 V bias (100 pA), where typically only the graphene lattice is imaged. Set of two red and two black arrows in the top left represents the armchair and zigzag direction respectively. Seven armchair edges (small red arrow) and one zigzag edge (small black arrow) are seen in this island. Scattering (blue arrow) is seen at step edges.

suggested that the (5×5) reconstruction is related to an incommensurate layer which gets separated into small subunits to relieve strain due to lattice mismatch. Riedl *et al* [191] studied the (5×5) reconstruction in detail under varying initial conditions prior to growth. Their work suggests that the relative coverage of (5×5) reconstruction depends on the initial treatment of the SiC surface with Si-flux.

In Fig. 3.5(a), we saw the topography in EG is dominated by step edges and domains of varying shape. A high density of steps suggests that the graphene growth may take place at the step edges. In my measurements, I have also observed graphene islands near the step edges and on the terraces. The relative population of the islands was found to be far less then step edges. Figure 3.7 shows a gradient enhanced image (1500 Å × 1500 Å) of a 1.8 ML_e thick sample. In this image, the gradient enhancement technique is particularly useful for identification of different layers and features based on roughness. To help in visualizing the roughness, I have identified the three layers 0, 1 and 2 on the basis of their texture. The image also shows two graphene islands on a layer 0 terrace. One

island is located near the step edge and the other island is in the middle of the terrace. This suggests that graphene islands can freely diffuse on the terrace. The smaller island identified by the white arrow is a layer 2 island. The bigger layer 1 island (red box) located near the step edge shows some interesting effects. This island is 180 Å wide and has a step height of ~2.8 Å.

The magnified high resolution (200 Å × 200 Å) image of the island is shown in Figure 3.7(b). It can easily be seen that the step edges of this island follows the direction of SiC reconstruction (blue lines). The angle between the blue lines is 120°. A set of two red and two black arrows in the top left corner of the figure represent the directions of the armchair and zigzag edges, respectively. In this image, we can identify seven armchair edges and one zigzag edge represented by small red and black arrows, respectively. Even at a low bias of 0.2 V where usually graphene is imaged (see Sec. 5.1.2), some interfacial features are visible indicating that the imaging in layer 1 graphene islands is dominated by SiC. The interface structure is imaged as trigonal features under RT conditions. A significant amount of scattering (blue arrow) is observed at the step edge indicating termination of graphene at the step edges [109–111]. High resolution images of the step edges (see Sec. 5.3) suggest a ($\sqrt{3}\times\sqrt{3}$)R30° scattering pattern. The free edges of the graphene islands may be bonded (covalent) to the substrate dangling bonds in a unique way.

In my STM studies, I found that the quality of a sample invariably depends on the background pressure during UHV growth. A higher value of the background pressure adversely affects the quality of the sample. Figure 3.8 shows 3000 Å × 3000 Å survey scans of three EG samples prepared from a common wafer. The samples were H_2 etched and cleaned in ultrasonic baths of acetone and ethanol prior to graphitization. During the graphitization of the sample imaged in Fig. 3.8(a), the background pressure rose to 8×10^{-8} Torr. It can observed that the sample has lot of defects and non-uniformity in the layer distribution. Also evident in the image is an unusually large number of island-like features. I found that if the background pressure is kept in control then the quality of the sample can be improved. This is evident in Fig. 3.8(b) and (c), where bigger terraces are observed. To ensure that the background pressure does not exceed a certain limit, care was taken to ensure that all the components that are heated are properly outgassed. This includes the sample heater, molybdenum sample holder and the tantalum tabs that hold the sample in place. Cryo-pumping was employed by filling the titanium sublimation pump (TSP) with liquid N_2 . Attempts were also

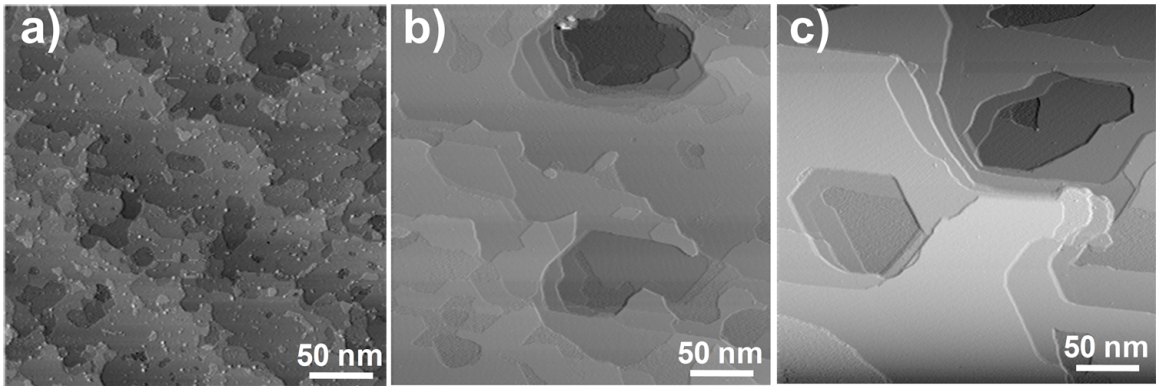

Figure 3.8: Background pressure in the UHV chamber during graphitization affects the quality of the sample. Three different samples shown in (a), (b) and (c) had a backgound pressure of 8×10^{-8}, 2×10^{-8} and 8×10^{-9} Torr, respectively during growth. Images (a), (b) and (c) were acquired at a bias voltage of -3, -4 and -3 V respectively, at a tunneling current of 100 pA

made to outgass samples prior to graphitization at lower annealing temperatures of 800 °C for several hours. Some attempts were made to improve the sample quality by depositing Si flux on the sample both prior to and during the graphitization. No discernable improvement however was observed in the quality of the samples using this process. In better quality samples a maximum terrace width of ~1000 Å was observed. As discussed previously, substantial amount of substrate roughening takes place during the growth, which may set an upper limit on the size of the terraces. LEEM measurements have reported similar results [87, 96, 172]. Some groups have also employed cryogenic techniques to keep the outgassing pressure in check during growth.

3.6 Conclusions

In this chapter I discussed the UHV graphene growth on 6H-SiC(0001). I showed that graphene growth in UHV results in a complex topography, with smaller domains and pits, due to substantial amount of substrate roughening. I also showed with STM imaging of low coverage samples, that the growth might possibly begin at step edges, at random locations. Si during growth, may diffuse out laterally or through the graphene films [132]. I showed locations of discontinuity (patches of layer 0 on a layer 1 terrace) in graphene coverage on terraces, that may act as ”venting sites” for Si. I also suggested, a growth mechanism where bigger graphene sheets might come together at these locations at elevated temperatures, resulting in a uniform coverage. Graphene islands in the middle of the terrace and step edges were showed. This suggested free diffusion of carbon on the terraces. I

showed that electronic properties of layer 1 islands in layer 0 are dominated by SiC reconstruction. I also showed that armchair termination is the preferred edge configuration in these islands. I also discussed the role of background pressure during growth. I showed that a high background pressure during growth adversely affects the quality of the sample.

CHAPTER IV

NEW GROWTH METHOD: LOW-VACUUM FURNACE GROWTH

UHV grown graphene on the Si-face of SiC was the first attempt to explore an epitaxial method to grow graphene. While being far from perfect, experiments done on this material system have produced some promising results [25, 55, 198, 229]. These samples suffer from smaller domains, fluctuations in layer distribution and a relatively high density of in-plane atomic scale defects [196]. These defects are scattering centers that slow down ballistic electrons by acting as "speed bumps" [196]. Transport measurements done on the Si-face have not produced high mobilities (1200 $cm^2V^{-1}s^{-1}$), although Subnikov deHass [25] oscillations were observed. This has prompted researchers to improve production methods for growing better quality graphene films. Some of this work includes growing graphene under different environmental conditions [62]. As explored in the previous Chapter, experimental conditions during the growth affects the quality of the samples. In the work described in this chapter, a new growth method is explored to improve the quality of the graphene films on SiC (0001). In this method, H_2 etched SiC samples are first graphitized in an RF-induction furnace. This is the starting template for graphene growth. These templates are further graphitized in UHV for thicker growth and for removal of carbon-based amorphous species observed via STM. The samples were found to be of superior quality with bigger domains and low defect density as compared to the UHV grown samples.

4.1 Sample Preparation

The samples are prepared on high purity semi-insulating 4H-SiC(0001) polytype purchased from Cree, Inc. [6]. After the H2 etching process (Sec. 3.1) the graphitization is carried out in a home-built radio frequency (RF) induction furnace (see Fig. 4.1(a)) [128]. In an induction furnace, a given material (typically a metal in a crucible) is heated by eddy currents that are produced due to varying electromagnetic (EM) field in the primary coil. In a conventional circuit, these eddy currents are undesirable, but in induction furnace they are of utmost importance and care is taken to maximize

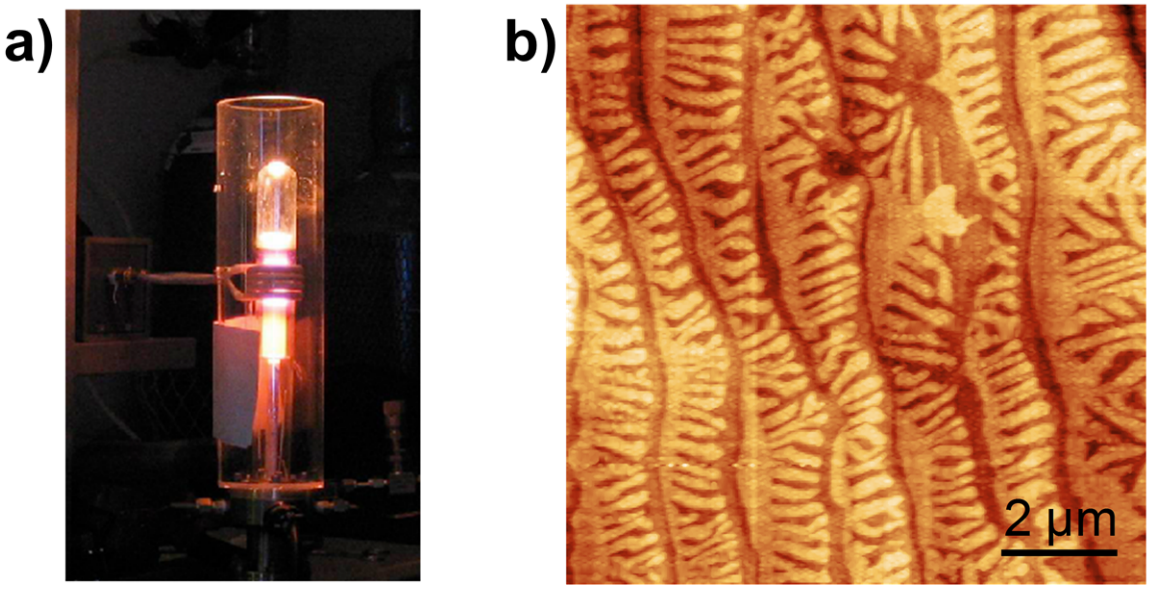

Figure 4.1: (a) An image of low vacuum (10^{-6} Torr) graphite RF induction furnace for epitaxial graphene (EG) growth. (b) AFM survey image (10 μm $\times$ 10 μm) shows unique topography of graphene grown on 4H-SiC(0001). The sample (#7H6) was annealed to a final temperature of 1550 °C during graphitization. The topography observed here is dominated by SiC steps and tiger stripe like patterns arranged perpendicular to graphene terraces.

them. An induction furnace offers many advantages over the conventional heating processes, including localized heating and rapid heating rates. The RF furnace designed by Dr. deHeer's group at Georgia Tech., is highly customized for graphene growth. The setup consists of a copper primary coil, AC power supply for generating varying EM field, a sample stage housed inside a ceramic tubing and a quartz shield. The furnace is operated under a low vacuum environment of 10^{-6}-10^{-5} Torr and during growth, the pressure is in the range of $\sim 10^{-4}$ Torr. The power supply generates an AC current for the primary coil, in the low RF (30-300 kHz) range. After the samples are loaded manually in the furnace, the graphitization process itself is fully automated via a LabView virtual instrument. For more details about the experimental parameters and furnace design, please refer to Ph.D. thesis work of Dr. Xuebin Li [128]. The furnace produces high quality graphene films on both faces of bipolar SiC. This work however is focused on graphene on the Si-face. Graphitization on Si-face in an induction furnace typically takes place at temperatures above 1350 °C. No significant changes are observed in the surface morphology of SiC for temperatures below 1300 °C.

The samples were transferred through air into RTUHV chamber for further characterization

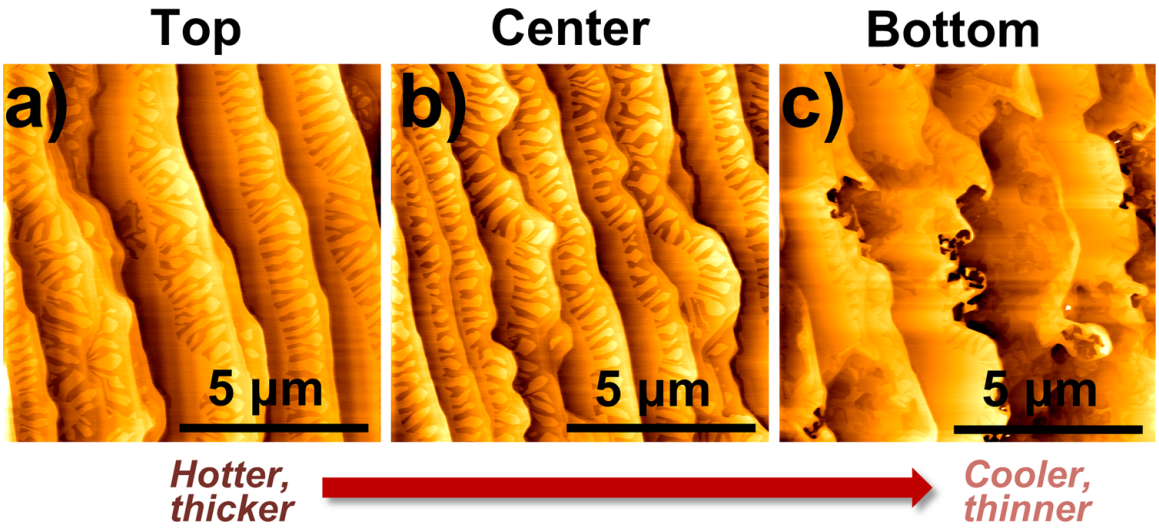

Figure 4.2: AFM images of the difference in the morphology at different location on the sample due to a thermal gradient. (a) 10 μm $\times$ 10 μm image shows bigger terraces in the top part of the sample compared to the terraces in the center as shown in (b). (c) Bottom part does not show *tiger stripes* suggesting a different morphology.

(AES, LEED and STM). AES measurement prior to annealing showed a small oxygen peak ($I_O/I_C <$ 0.1) depending on the time it was exposed to air. Some of these graphitized templates were heated in the RTUHV system to graphitization temperatures to get rid of the observed amorphous features after characterization. Growth in low vacuum environment in the induction furnace also resulted in some nanocap like features along with other amorphous carbon species (discussed in Sec. 4.2).

4.2 Furnace Grown Si-face Samples

Graphene growth under UHV conditions is expected to be different from graphene growth through low vacuum furnace. For understanding graphene growth, it is important to study the environment, and outgassing properties of different components in the low vacuum furnace. This would highlight the role of intermediate compounds and catalytic species generated under such conditions. Under UHV conditions, the Si which desorbs from the sample, gets lost to the vacuum. Consequently, the growth takes place at a lower temperature ($\sim$1200 $^\circ C$) in a Si depleted environment. At such temperatures, the graphene islands that are formed do not have enough energy to diffuse and thereby combine with other islands resulting in a sample that has smaller domains and more defects. Silicon

has a higher vapor pressure in a furnace environment, as compared to a UHV environment. Furthermore, under low vacuum conditions (10^{-4} Torr), there is a significant amount of background pressure in the furnace, which makes it difficult for the Si atoms to desorb. The Si atoms come off at a slower rate and their supply keeps getting replenished as the atoms bounce back from the walls, as well as the other heavier species present in the background pressure. This can be envisioned as a gradient in the Si flux away from sample. This enables the growth to take place at a higher temperature. Studies show that better quality graphite films can be grown by high temperature annealing. Cancado *et al* [39] studied the progression in the quality of graphite samples as a function of annealing temperature (1800-2700 °C), which were heated in an electrical furnace. Their STM and x-ray measurement results showed a significant improvement in the quality and average domain size for samples that were heated to a higher temperature.

Under low vacuum conditions, several different process are possible, depending on the partial pressure of O_2. It is important to note that for effective graphitization, the SiC surface has to be protected from the oxidation process. Presence of a Si rich environment could prevent SiC surface from O_2 etching. Gulbrans *et al* [83] studied oxidation of SiC at different partial pressure of O_2. They observed a weight loss of the sample at low O_2 pressure combined with high temperature. This is called *active oxidation*.In this reaction, SiO and CO species are released in this reaction. Whereas at high O_2 pressure a weight gain was observed due to the formation of a protective SiO_2 film along with release of CO. Different mechanisms have been discussed in the review article by Harris *et al* [89] which was focused on production trends in oxide layer growth on SiC. The degree of O_2 pressure during high temperature heating, determines the formation of SiO_2 layer that protects the surface or material loss due to O_2 etching.

Kusunoki's group [19, 115–117, 137] have studied low vacuum (10^{-4} Torr) high temperature annealing of both faces of SiC. They observed formation of graphite films on the Si-face(0001) [116] and carbon nanotubes on the C-face($000\bar{1}$). The growth was carried out in a custom designed electric resistance carbon heater. The Si-face samples were heated to temperatures of 1350 and 1700 °C for half an hour. The cross-sectional high resolution transmission electron micrscopy (HRTEM) studies at low temperature suggests a three-layer collapse mechanism similar to the conclusions drawn in an earlier work [210]. On the C-face however raised nanocaps (3-5 nm in diameter, 3-5 nm in height)

in graphene films were observed at 1300 °C. These were explained by formation of SiO bubbles on the SiC surface due the reaction of O_2 with SiC:

$$SiC + \frac{1}{2}O_2 \rightarrow SiO + C. \text{ [117]}$$

With further increase in temperature the graphite films start to stand up perpendicular to the SiC plane leading to the formation of carbon nanotubes towards the interior of SiC [117]. It was suggested that the structural differences between Si and C face may be responsible for observed different growth mechanisms [116]. Graphene sheets on Si-face grow in a parallel fashion and protects SiC surface from the oxidation. Clearly in our induction furnace graphene growth on both Si and C face suggests different mechanisms mediated by the enviorment in the furnace.

Figure 4.1(b) shows an atomic force microscopy (AFM) [5] image of a furnace-grown epitaxial graphene (EG) sample (#7H6). This sample was heated to a temperature of 1550 °C for graphitization. In this 10 μm × 10 μm image, the topography is dominated by SiC steps with considerably bigger terraces as compared to UHV grown samples. Also evident in the image are raised fingering features (*tiger strips*), aligned perpendicular to the edge of the terraces. There exists a thermal gradient in furnace rendering the top part of the sample thicker than the bottom part. Figure 4.2 shows 10 μ ×m 10 μm AFM images acquired from three different locations on a 6H-SiC(0001) furnace graphitized sample. This sample was heated just to grow a thin sample. AFM image from the top part of the sample shows (see 4.2(a)) bigger terraces compared to the center 4.2(b). *Tiger stripes* are also evident at these locations. Morphology of the bottom part however is observed (see Fig.4.2(c) to be different from the top and the center. Absence of tiger stripes that seem characteristic of furnace graphitized surfaces suggests that this part may not be graphitized. STM data in our measurements was acquired from the center of the samples.

Figure 4.3(a) shows an STM image of a furnace grown sample (#7H6) acquired at +3 V. The sample thickness was found to be 2.1 ML_e from AES and 9.3 Å from ellipsometry data. The sample was heated to 1100 °C prior to imaging for oxygen removal, which was confirmed by AES. In this survey image (4000 Å × 4000 Å), one can observe what will be shown to be *tiger stripe* features (red arrows) that are perpendicular to the terraces and terminate before the step edge. Also evident in this image are amorphous carbon species filling up the *tiger stripes*, which were previously imaged

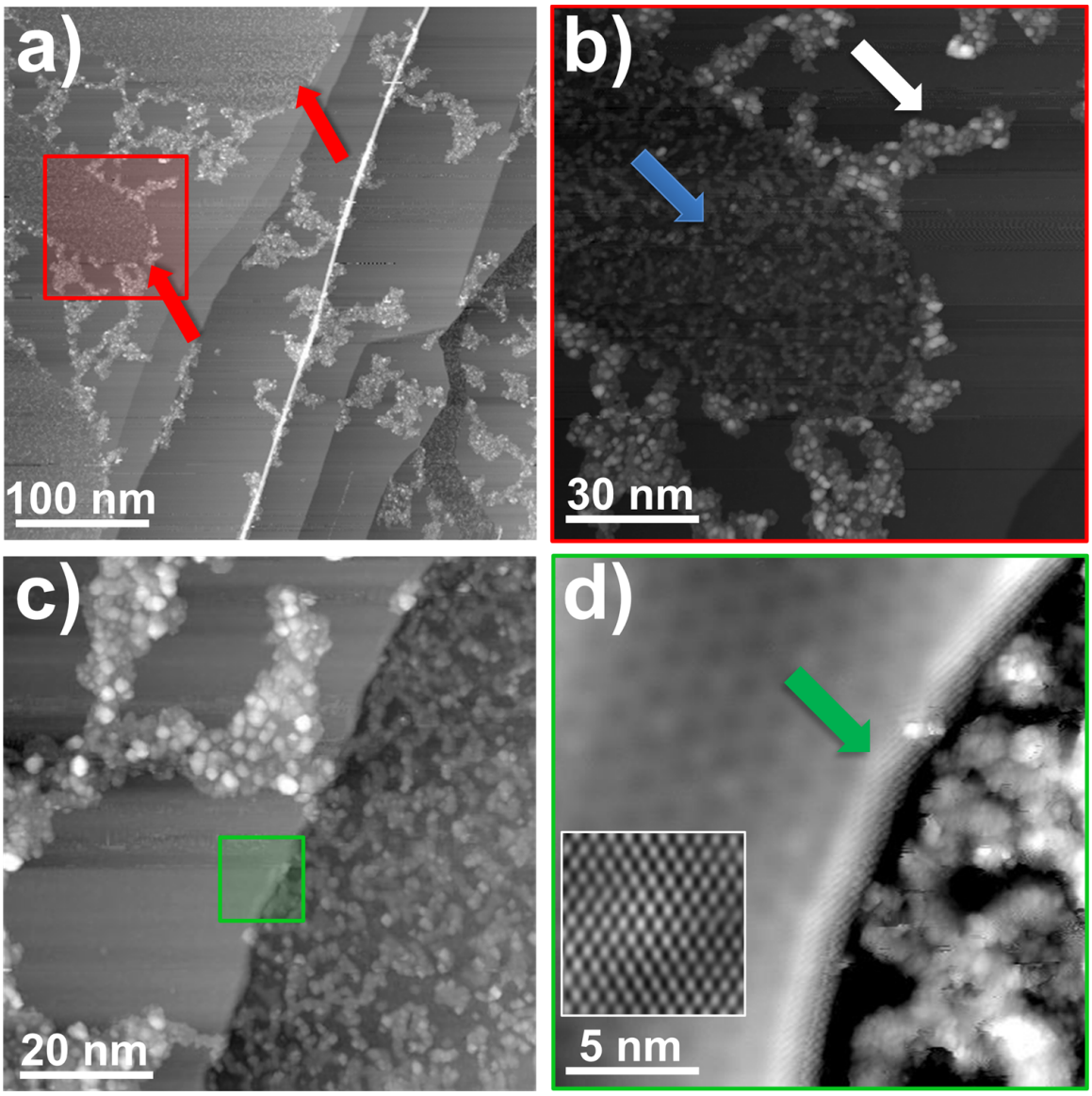

Figure 4.3: STM imaging of low vacuum induction furnace grown epitaxial graphene (EG) sample on 4H-SiC(0001). The sample was cleaned by thermal annealing (1100 °C) prior to imaging. (a) 4000 Å × 4000 Å scan shows tiger stripe regions (red arrow) surrounded by nanocap like formation (+3 V, 100 pA). Puckering of graphene is imaged as bright line along the step edge. (b) Magnified image (1200 Å × 1200 Å) of the region marked in (a). The image (+3 V, 100 pA) shows amorphous carbon species (3 Å high) inside *tiger stripe* features surrounded by nanocaps (12 Å high). (c) 800 Å × 800 Å image shows valley region alongside a step edge of a terrace covered with nanocaps (+3 V, 100 pA). (d) Magnified (240 Å × 240 Å) image of region marked in (c)(green box) shows scattering (green arrow) at the step edge (+1.2 V, 100 pA). Inset shows high resolution layer 2 graphene on the terrace with trigonal lattice (+0.3 V, 100 pA).

as flat raised features in the AFM image (see Fig. 4.1b). The stripes are surrounded by taller amorphous features (nanocaps) similar to the features observed on UHV grown C-face samples ([127]).

Figure 4.3(b) shows zoom in (1200 Å × 1200 Å) on one of the tiger stripes (red box in Fig. 4.3(a)). Here one can observe clear distinctions between the smaller amorphous features (blue arrow) and nanocaps (white arrow) that are of height 3 Å and 12 Å respectively. Under low vacuum conditions, due to significant background pressure and required elevated temperatures, different species have enough energy to diffuse to low energy sites. Among various low energy sites for nucleation (step edges, pits etc.), wrinkles in the graphene films also act as a low energy site for diffusing species. Consequently, numerous carbon-based clumps get trapped in these low energy sites by forming additional bonds in the wrinkled films, thereby lowering their energy and becoming stable. Bias dependent imaging did not reveal any apparent changes in the amorphous features. The bright line running along the step edge in Fig. 4.3(a) is the puckering of the graphene film at the step edge. These puckers may be caused by thermal expansion coefficient mismatch between SiC (4.0×10^{-6} /°C) and graphene (1.5×10^{-5} /°C), mediated by the sharp SiC step edges. It should be pointed out that the graphene blanket was observed to be continuous over step edges, except from a region of layer 1 to layer 0 where continuity cannot be confirmed because the graphene structure in layer 0 is unresolved. Another potentially interesting region is seen in the bottom right part of Fig. 4(a) where the graphene blanket falls into a valley covered with amorphous features. A similar region (800 Å × 800 Å)located in a different part of the sample is shown in Fig. 4.3(c). Figure 4.3(d) is a magnified image (240 Å × 240 Å) of the green boxed region in Fig. 4.3(c). Scattering is observed at the step edge (green arrow) and graphene film was not observed to be going over the valley regions even at low bias, which is ideally suited for imaging graphene. It is not clear whether there is graphene under the amorphous species; it seems to be rather predominantly covered by layer 0. The inset in Fig. 4.3(d) shows an atomic scale image of bilayer graphene on the terrace.

4.3 Regraphitization in Ultra-high Vacuum

In the previous section (Sec. 4.2), we observed considerably larger domains on the furnace grown samples compared to samples grown with the traditional UHV technique. These samples however have their own intrinsic problems with amorphous carbon species littering the sample surfaces. In my experiments, these species were found to be stable upto 1100 °C without any discernible change in their structure. These samples could be used effectively as templates for further regraphitization

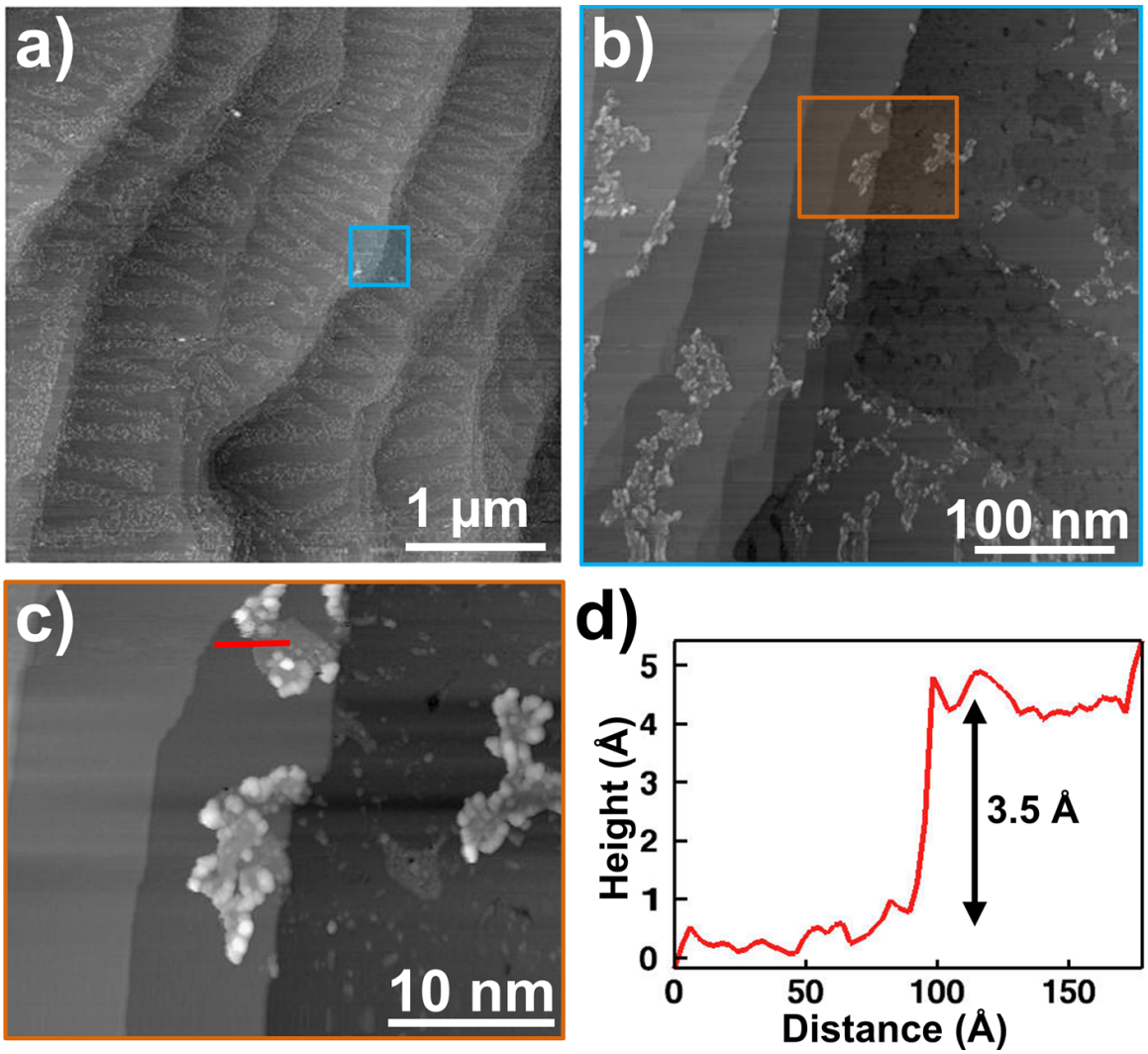

Figure 4.4: STM imaging of UHV regraphitized (1280 °C) furnace grown template on SiC(0001). (a) A 4 μm × 4 μm survey scan showing tiger stripes perpendicular to terraces and a topography dominated by SiC steps (+4 V, 100 pA). (b) Magnified image (4000 Å × 4000 Å) of region marked in (a)(blue box) showing nanocaps on terraces. Tiger stripe features (right side of (b)) with non-uniform coverage of layer 0 and layer 1 (+4 V, 100 pA) are also seen. (c) 1200 Å × 900 Å image (red box region in (b)) showing change in the structure of nanocaps (+1V, 100 pA). (d) A line profile at the nanocap step edge shows a height of 3.5 Å.

in UHV.

Figure 4.4 shows the topographic features of a furnace grown sample (#7H6) annealed to a graphitization temperature of 1280 °C. The sample was found to be 2.6 ML_e thick from AES. In Fig. 4.4(a) (4 μm × 4 μm), one can observe reminiscent of *tiger stripe* features that remain strongly etched in the terrace even after high temperature annealing in a topography dominated by

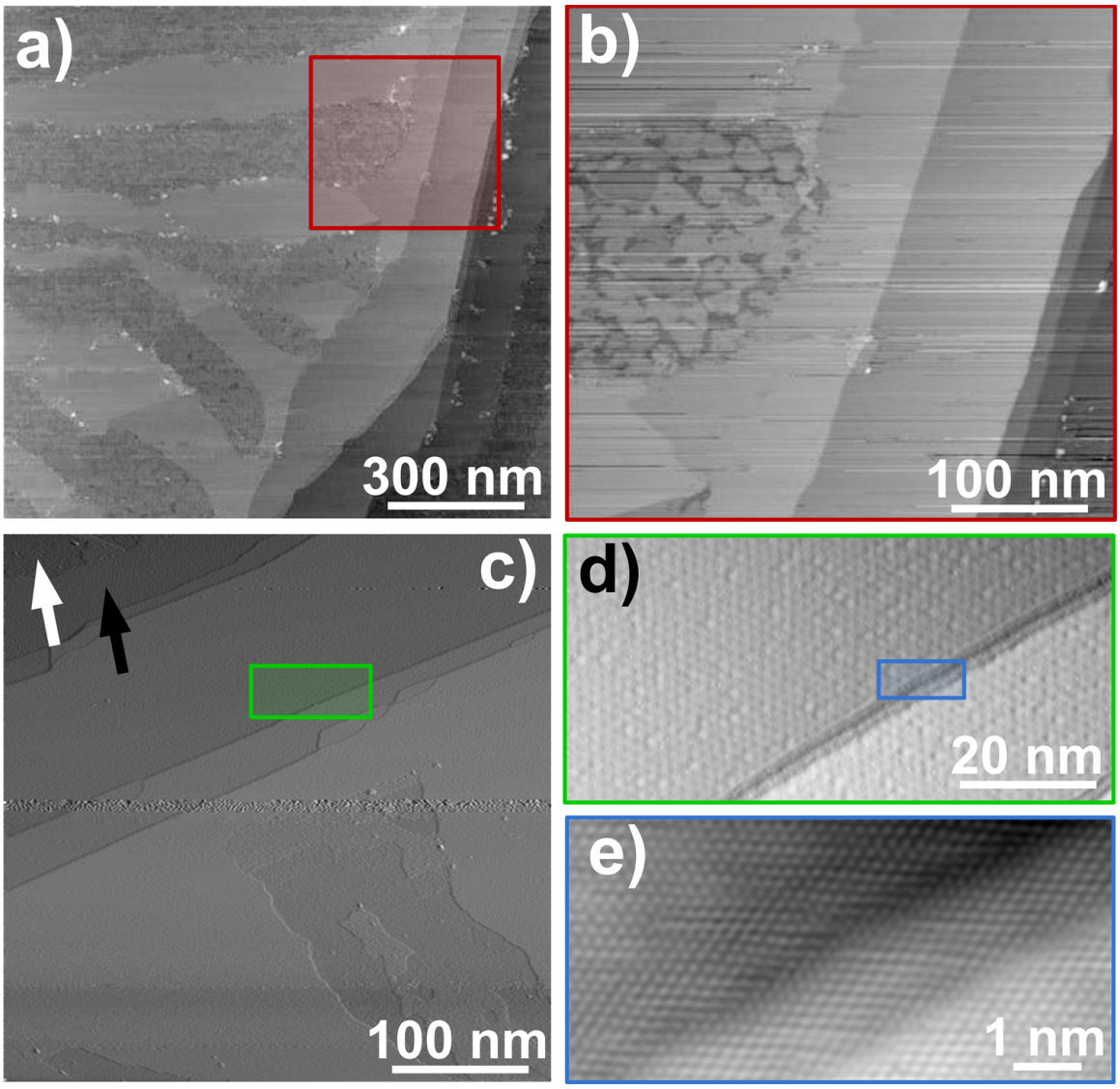

Figure 4.5: UHV graphitization at a higher temperature (1320 °C) removes nanocaps from the terraces. (a) 1.2 μm × 1.2 μm image shows tiger stripe features etched on the terrace (+4 V, 100 pA). Amorphous nanocap features are missing from the terraces after high temperature (1320°C) annealing. (b) Magnified image (4000 Å × 4000 Å) of the marked (red box) region in (a)shows non-uniform coverage of graphene in *tiger stripes*. Right side of (b) shows clean graphene terraces without nanocaps (+6V, 100pA). (c) 4000 Å × 4000 Å image of a different sample annealed to 1350 °C showing bigger terraces and uniform coverage of graphene in the tiger stripe (+1 V, 100 pA). (d) 800 Å × 800 Å magnified image of the region marked in (c) shows a step edge and the (6×6) period in EG (+1.0 V, 100pA). (e) High resolution magnified image (80 Å × 80 Å) of the stepedge shows graphene to be continuous over the step edge (+0.3 V, 100pA). No scattering is observed at this location.

SiC steps. *Tiger stripes* were found to be perpendicular to the graphitized terraces. Figure 4.4(b) shows a magnified image (4000 Å × 4000 Å) of the region marked (blue box) in Fig. 4.4(a). In

this image, *tiger stripe* regions are observed to be free of the amorphous carbon species that were present prior to graphitization (see Fig. 4.3(b)). These regions were found to contain non-uniform patches of layer 1 graphene with voids filled with layer 0 between them. The background pressure was high (8×10^{-8} Torr) during the graphitization process, and a large number of defects and non-uniformities were found in the graphene films in this region. Nanocaps were found on narrow terraces (Fig. 4.4(b)), and the graphitized regions alongside *tiger stripes*. Significant changes were observed in the structure of nanocaps after UHV heating to 1280 °C.

Figure 4.4(c) shows a magnified image (1200 Å × 1200 Å) of a nanocapped region in Fig. 4.4(b) (orange box). The valley regions (right part of Fig. 4.4(c)) were found to have graphene coverage with defects and nanocaps. Some parts of the nanocaps were observed to have a flatter topography. Figure 4.4(d) shows a line profile over the flat part of the nanocap with a step height of 3.5 Å, close to graphite step of 3.35 Å. However, atomic scale measurements did not image graphene in this region, due to non-uniformities in nanocap structure. This sample was further annealed to a graphitization temperature of 1320 °C for complete removal of nanocaps and other carbon species. The sample was found to be 3.0 ML_e thick from AES with sharp LEED spots, indicating bigger domains. Figure 4.5(a) shows a 1.2 μm × 1.2 μm survey topograph of the sample (#7H6) regraphitized the second time. Although the tiger stripe region is still evident, the terraces now are observed to be free of nanocaps. This is also true for the valley regions alongside the step edges. Fig. 4.5(b) is a magnified image (4000 Å × 4000 Å) of the region marked in Fig. 4.5(a) (red box) that shows the topography inside the *tiger stripe*. These regions were found to contain non-uniform patches of layer 1 graphene that with a few layer 2 islands. These patches of layer 1 were separated by narrow canyons of layer 0. Figure 4.5(c) shows a big STM image (4000 Å × 4000 Å) of a furnace grown sample annealed directly to a graphitization temperature of 1350 °C. The background pressure during annealing was 2×10^8 Torr. The *tiger stripe* regions are observed to have uniform graphene coverage. The gradient enhanced image assists in identifying different layers based on roughness. layer 0 and layer 1 regions are indicated in the figure by white and black arrow respectively. The region is dominated by layer 2 coverage. Figure 4.5(d) shows 800 Å × 400 Å magnified image of the green boxed region in (c). In this image of the step edge, (6×6) (20Å) period is evident. The graphene on either side of the step is layer 2 as observed in Fig. 4.5(c). No

scattering is observed at this double step suggesting the continuity of the graphene blanket over this region. In fact graphene was found to be continuous over variety of step edges configuration except between a layer 0 and layer 1 step. This will be discussed in detail in Sec. 5.3.

On the whole, the quality of the graphene film grown by regraphitization of furnace grown templates is significantly better, if the background pressure is kept low during UHV growth. The average domain size in my experiments was found to be $>$ 300 nm. The samples also exhibited lower defect density. Out of nearly fifty high resolution atomic scale (200 Å $\times$ 200 Å) scans on one of the samples, only one defect was observed. This is clearly a marked improvement in the quality of epitaxial graphene films on SiC (0001).

4.4 Conclusions

In this chapter I discussed a new method to grow graphene films on SiC(0001). I showed that graphene samples grown in low vacuum induction furnace have considerably bigger (300 nm) domains and lower defect density as compared to UHV grown samples. I discussed how the environment in the furnace might play an important role in the growth mechanism. AFM images showed unique raised fingering features (*tiger stripes*) emanating from the step and aligned perpendicular to terraces. With high resolution STM imaging, I showed that the tiger stripes are filled with amorphous carbon based species (~3 Å high) in contrast with the AFM imaging. The tiger stripes were "necklaced" and surrounded with nanocap (~12 Å high) like features. The terraces found to have a partial coverage of nanocaps. I discussed how wrinkles in the graphene films during growth may act as a low energy site for amorphous species. Clearly a an understanding of the origin and composition of these amorphous species is lacking.

The graphene sheets were found to be discontinuous over the the tiger stripe regions. The nanocaps and amorphous species in the tiger stripes were stable upto 1100 °C after thermal cleaning for STM. An attempt was made to thermally clean the sample to remove nanocaps and amorphous species in the tiger stripes. Heating the sample up to 1280 °C removed the amorphous species in the tiger stripes, which was also found to be covered with non-uniform patches of layer 1 graphene surrounded by voids of layer 0 (interface). The structure of the nanocaps was found to be different after heating with some parts of it having a flatter (~3.5 Å step) topography. After heating the

samples to 1320 °C the samples were found to be free of nanocaps and other amorphous species. The graphene was found to be continuous over the steps. Heating the samples directly to even higher temperatures (~1350 °C) filled up the tiger stripe regions with uniform graphene coverage. To my knowledge this is first high resolution STM studies of furnace grown Si-face samples.

CHAPTER V

STRUCTURAL AND ELECTRONIC PROPERTIES OF EPITAXIAL GRAPHENE

Ideal graphene is envisioned as a perfect flat plane of sp^2 bonded carbon atoms in a trigonal planar geometry. In real-life however, the topography is often corrugated. Giant corrugations [149, 150] have been observed on the ever so popular mechanically-exfoliated graphene, even at a very local scale [97]. Regions of electron-hole puddles [136] are found occurring naturally in graphene due to unavoidable disorder in the SiO_2. The interaction with the substrate plays an important role in the electronic properties of all graphene films. In epitaxial graphene(EG)/SiC systems, an interface region exists sandwiched between graphene overlayers and the SiC substrate. Furthermore, the graphene overlayers are found to be intrinsically electron doped due to charge transfer from the interface [228].

5.1 Different layers in epitaxial graphene

In this section, different layers commonly observed on EG (on SiC(0001)) after graphitization will be discussed. The layers, namely: layer 0, layer 1 and layer 2 exhibit unique structural and electronic properties. These layers grow epitaxially, and are found to be rotated 30° with respect to the underlying SiC lattice (see Sec. 3.4 for a detailed discussion).

5.1.1 Layer 0

Layer 0 is commonly referred as the *buffer* or the *interface* layer which is imaged as a stable $(6\sqrt{3}\times 6\sqrt{3})R30^\circ$ reconstructed layer in STM measurements. This is the main SiC reconstruction (there can be also a small 5×5 component) that is commonly seen after the graphitization process. Please refer to Sec. 3.3 for a detailed discussion about different reconstruction phases commonly observed in hexagonal SiC. This unavoidable layer forms naturally during the growth process around an annealing temperature of 1100-1150 ° C [135, 175, 176] and can influence the transport in the overlying graphene layers.

Figure 5.1(a) shows an empty state image of layer 0 acquired at +0.4 V. The sample is 2.3 ML_e

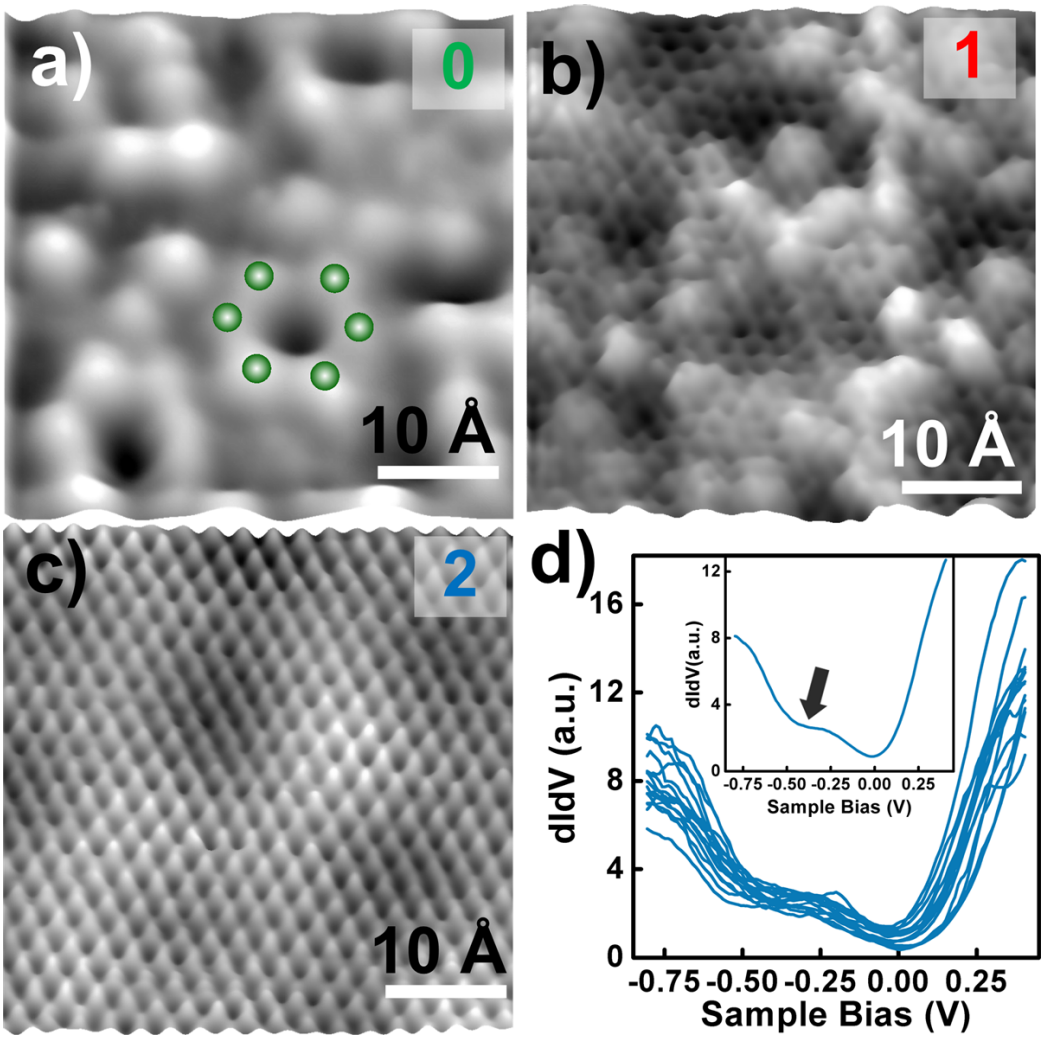

Figure 5.1: Difference in structural and electronic properties of layer 0, layer 1 and layer 2. (a) High resolution image (15 Å × 15 Å) of layer 0 (interface) shows no indication of a graphene network (1.0 V, 100 pA). Bias dependent imaging also did not reveal any graphene related features. Green balls indicate six orbitals of the hexagonal features commonly seen in this layer. (b) layer 1 shows position dependent variation in the imaging (15 Å × 15 Å) due to interface reconstruction (0.4 V, 100 pA). Graphene lattice is evident in areas not dominated by interface LDOS. (c) 15 Å× 15 Å layer 2 image shows a trigonal lattice as two neighboring carbon atoms do not image identically. (d) Randomly chosen 15 spectra in a 30 Å × 30 Å region of layer 2 terrace. The inset shows spatially averaged spectrum with a suppression in the DOS near -0.4 V. This is believed to be the position of the Dirac point [226].

thick. In this image, we do not observe any evidence of the graphene lattice. Bias dependent imaging also did not reveal any structural similarities with graphene and SiC. This suggests an interface between graphene and SiC. Counting only layers 1 and 2 (those that image as a carbon honeycomb), the graphene coverage of this sample is 1.5 ML_e. The difference of 0.8 ML_e between the AES film

thickness and the graphene coverage determined by STM implies that layer 0 is carbon rich. In previous studies, Johansson *et al* [100] observed a large amount of carbon, and surface-shifted features in Si (2p) and C (1s) levels, in core-level photoemission measurements on $(6\sqrt{3} \times 6\sqrt{3})R30^\circ$ surface. It was suggested that the carbon is not graphitic, and the reconstruction extends to a few layers, similar to the recent interpretations by Hass *et al* [92]. However, Forbeaux et.al [70, 71] observed graphitic π^* and σ^* bands in their k-resolved inverse photoemission spectroscopy (KRIPES) measurements for samples annealed to similar temperatures. They concluded that graphite films are formed on SiC(0001) at annealing temperatures of 1100 °C. An attempt was made by Chen *et al* [45] in 2005 to explain this discrepancy by proposing a carbon *nanomesh* of tiny graphitic islands as the interface. They suggested that these islands exist as isolated domains on SiC arranged in a (6×6) supercell structure. Several other recent theoretical [139, 211] and experimental [13, 173, 191] attempts have been made to explain the atomic arrangement in $(6\sqrt{3} \times 6\sqrt{3})R30^\circ$ reconstructed layer, but the verdict is still pending. Recent surface x-ray reflectivity measurements are best fit by a model where the transition spans one SiC bilayer (in which carbon largely replaces Si) plus a low-density predominantly Si adatom layer [92, 197]. Recent photoemission measurements [63] suggest that layer 0 is essentially a graphene like network where the C-C bond length is the same as graphene. It was also suggested that the dangling bonds of the SiC interface were covalently bonded with every third atom of this graphene like network. However, in our STM measurements most commonly observed features on layer 0 were found to be tetramers and hexagons. Figure 5.1 shows hexagon features highlighted by six green balls which were found to lie on $(\sqrt{3}\times\sqrt{3})$R30° SiC sublattice.

This layer 0 interface must be detrimental to the transport in graphene overlayers due to the presence of dangling bonds. Raman spectroscopy measurements on EG [198] (also discussed in Chapter. 6) suggest some influence of the interface region on the electronic properties of layer 1. There has been some partial success recently in passivating the SiC dangling bonds with atomic hydrogen [82].

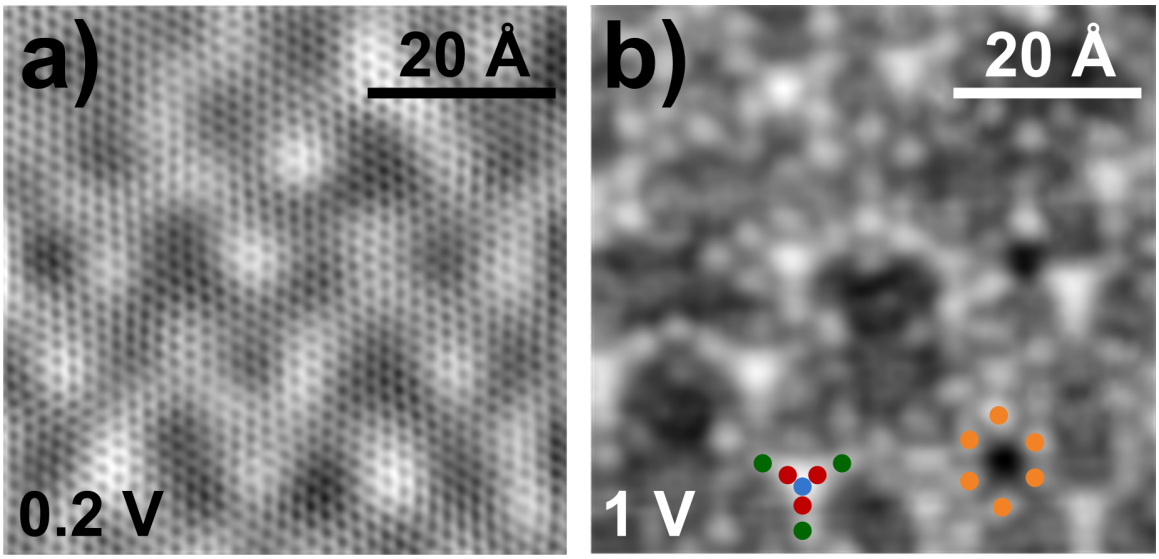

Figure 5.2: STM imaging of layer 1 graphene shows different topographic character at varying bias voltages. (a) 60 Å × 60 Å high resolution image shows a honeycomb lattice on layer 1 graphene (+0.2 V, 100pA). All six atoms of the graphene lattice are clearly resolved. (b) High bias (+1.0 V, 100 pA) imaging on the same terrace shows adatom like interfacial features replacing the graphene lattice. Two common features namely tetramers and hexagons, are observed. Hexagon orbitals are represented by orange balls, and tetramers are indicated by one blue and three red balls. Additional orbitals surrounding tetramers are represented by three green balls. Graphene deforms as it drapes over the interface features (tetramers) which is apparent as a (6×6) period in (a).

5.1.2 Layer 1

layer 1 is the graphene layer that forms above the interface layer. This layer images as a honeycomb lattice for low STM bias voltages <0.3 V and exhibits unique topographic character at higher biases [34, 133, 197]. Figure 5.1(b) is an empty states image (0.4 V) of layer 1 that shows the unique character of the STM "topography" which is dominated by position-dependent variations in the local density of states due to the subsurface (layer 0) reconstruction. Throughout the image, a network of sp_2-bonded C atoms as an underlying honeycomb pattern is evident. The tunnel voltage in the image was chosen to enable imaging of both the graphene lattice and the subsurface interface states [197].

Unique electronic character of SiC and layer 1 interaction, is also evident in the bias dependent imaging shown in Figure 5.2. The images are acquired from the same terrace of a 2.0 ML_e thick sample. Figure 5.2(a) shows an atomic resolution image (60 Å × 60 Å) of layer 1 graphene at 0.2 V. All six carbon atoms of the honeycomb lattice are observed along with a bigger (6×6) period

(discussed in Sec. 3.4). At a higher bias (1.0 V), graphene loses its transparency and adatom like features are observed instead of a graphene blanket (see Fig. 5.2(b)). Similar variation in the imaging as a function of bias voltage has been observed by other groups [34, 120, 197].

High bias scans revealed two distinct regular features on layer 1, namely: tetramers and hexagons, dominating the topography, with the number of tetramers being significantly greater than hexagons. It is reported [197] that at low temperature the tetramers image as a single lobe at high bias (1.0 V) and as a tetramer at lower bias (0.5 V) empty states imaging, whereas they are observed as a trimer in filled states imaging. Figure 5.2(b) shows a hexagon feature, where orange circles are placed on the observed six protrusions in the hexagon. In my experiments, the hexagons were found to lie on the ($\sqrt{3}\times\sqrt{3}$)R30° SiC sublattice. Also evident in Fig. 5.2(b) are tetramers (three red and one blue circle), surrounded by three orbitals (green balls) found lie on the same ($\sqrt{3}\times\sqrt{3}$)R30° sublattice. The observed features are due to an electronic effect that has been explained by partial hybridization of SiC dangling bonds with delocalized graphene bands [197]. These interfacial features are responsible for shaping the topography of the graphene sheet.

As mentioned previously, a (6×6) period is observed as the graphene blankets over the interfacial features. Judging by the relative population of tetramers and hexagons, it seems that the tetramers which were observed to be far greater in number are responsible for the observed period. Previously, the (6×6) period was believed to be caused by a *Moiŕe* effect in the STM studies by Forbeaux *et al* [71]. Recent low temperature STM measurements and DFT measurements done by Rutter *et al* [197] at NIST observe similar interfacial features (Owman *et al* made similar observations much earlier [176]). The group also suggests a carbon rich interface with Si adatoms similar to the model proposed by Hass *et al* [92]. Interestingly, our STM measurements show a step-height of 2.4 A from layer 0 to layer 1, consistent with the surface x-ray reflectivity measurements [92], but much smaller than the 3.35 Å interlayer spacing in graphite. This suggests some interaction between the interface layer 0 and the layer 1 graphene [198]. It is not evident if the interfacial features depend on the SiC polytype (4H-, 6H-).

ARPES measurements done by Zhou *et al* [228] suggest the presence of a graphene-like structure in layer 0 Bernal stacked with respect to layer 1. They observed a band gap of 0.26 eV in layer 1 spectra which was explained by sublattice symmetry breaking. Another group [33, 194] has

employed ”many-body” interactions argument to explain this feature which they believe is due to electron plasmon coupling. If Zhou et.al are to be believed then such a stacking would introduce an asymmetry in the charge density on the neighboring atoms which potentially could be observed via low bias STM measurements. We, however, did not observe any deviations from the honeycomb lattice in STM imaging. All six carbon atoms were regularly imaged at low bias. Moreover, as discussed previously, high bias imaging was dominated by interfacial features.

5.1.3 Layer 2

The stacking order of graphene layers plays a major role in shaping the electronic properties and Landau spectrum [80, 81] of the system. The most widely studied example of such behavior is the Bernal stacking in bilayer graphene. In Bernal stacking [106], the second layer is positioned such that the A' atoms in the top layer are directly above the A atoms in the bottom layer and the B',B atoms don't have anything directly above or below them(see inset Fig. 5.4). These layers are separated by a distance of 3.35 Å [50] with weak coupling ($\tau_\perp$=0.4 eV) between them. This breaks the sublattice symmetry and the electronic structure changes as a result. Theoretical work done by Latil *et al* [119] indicates preservation of linear dispersion for turbostratic (randomly rotated layers) multilayered systems. Such behavior has been observed experimentally in multilayered epitaxial graphene on SiC(000$\bar{1}$). X-ray measurements [92] suggest unique stacking of the graphene layers that enables many layers to electronically behave like a single layer. Recently there has been much interest in bilayer graphene. It is being investigated extensively both theoretically [105, 129, 143, 144, 154] and experimentally [95, 169, 185, 217] driven partly by the possibility of new electronic devices.

The Bernal stacking of bilayer graphene gives rise to unique electronic dispersions [143]. The low energy dispersion (Energy vs wavevector k) exhibits four hyperbolic bands. This is due to hybridization of bonding orbitals of A atoms in the two layers. Two of the bands meet at the Fermi level and the other two are separated by 0.4 eV, the strength of interlayer coupling constant ($\tau_\perp$=0.4 eV) [95]. This is in contrast with the two band linear dispersion exhibited by the single layer graphene. The charge carriers in bilayer graphene commonly referred to as *massive Dirac* particles, remain chiral in nature. They exhibit a Berry's phase of 2π as predicted by theory [143]

and observed experimentally [169]. The hyperbolic bands can be further perturbed by introducing asymmetry [142] in the system. For example, application of perpendicular electric field introduces a gap, which can be controlled.

It is believed that layer 2 EG on SiC substrate is Bernal stacked. ARPES measurements [171, 228] indicate band dispersions representative of bilayer graphene. An asymmetry in the form of a band gap is observed in these dispersion relations. layer 1 graphene is doped, as it accumulates the charge transferred from the interface. layer 2, on the other hand, is relatively undoped making it inequivalent to layer 1. This potential difference between the two layers is balanced out by a natural opening of gap. The gap can be controlled by electron doping which can be done by depositing metal on the sample. Ohta *et al* [171] demonstrated this by depositing pottasium on the sample. They observed closing and opening of the gap as the potassium deposits were increased which again can be explained by apparent changes in potential difference due to changes in the doping levels.

In the past, STM imaging has been used to study electronic properties and crystal structures of materials. One such classic example is the STM imaging of Si(111) [23, 31], which helped in resolving some the mysteries of its 7×7 reconstructed phase. Kubby *et al* [113] correlated bias dependent STM images with *dI/dV* spectra, and observed a layer resonance between the top surface (adatom layer) and the remaining bulk crystal. Similar measurements on HOPG, has led to an observation of a trigonal pattern [14, 15] at low bias conditions unlike the honeycomb lattice. This is a direct evidence of asymmetry in the charge density of the neighboring atoms due to Bernal stacking.

In the layer 2 empty-states image acquired at 0.5 V (Fig. 5.1(c)), the graphene atomic lattice is observed, but the two sublattice atoms in the honeycomb do not image identically. Also evident in Fig. 5.1(c) (and 3.4) is a superimposed modulation of the graphene surface height. This (6×6) period is due to the deformation of the graphene sheet as it blankets layer 1 and the interface reconstruction. The step height between layers-1 and 2 is 3.4 Å , essentially the same as the interlayer spacing of graphite.

In a recent theoretical work, Wang *et al* [218] computed the LDOS for both single and bi-layer graphene. They suggest that A the and B sublattice sites are not equivalent and should show

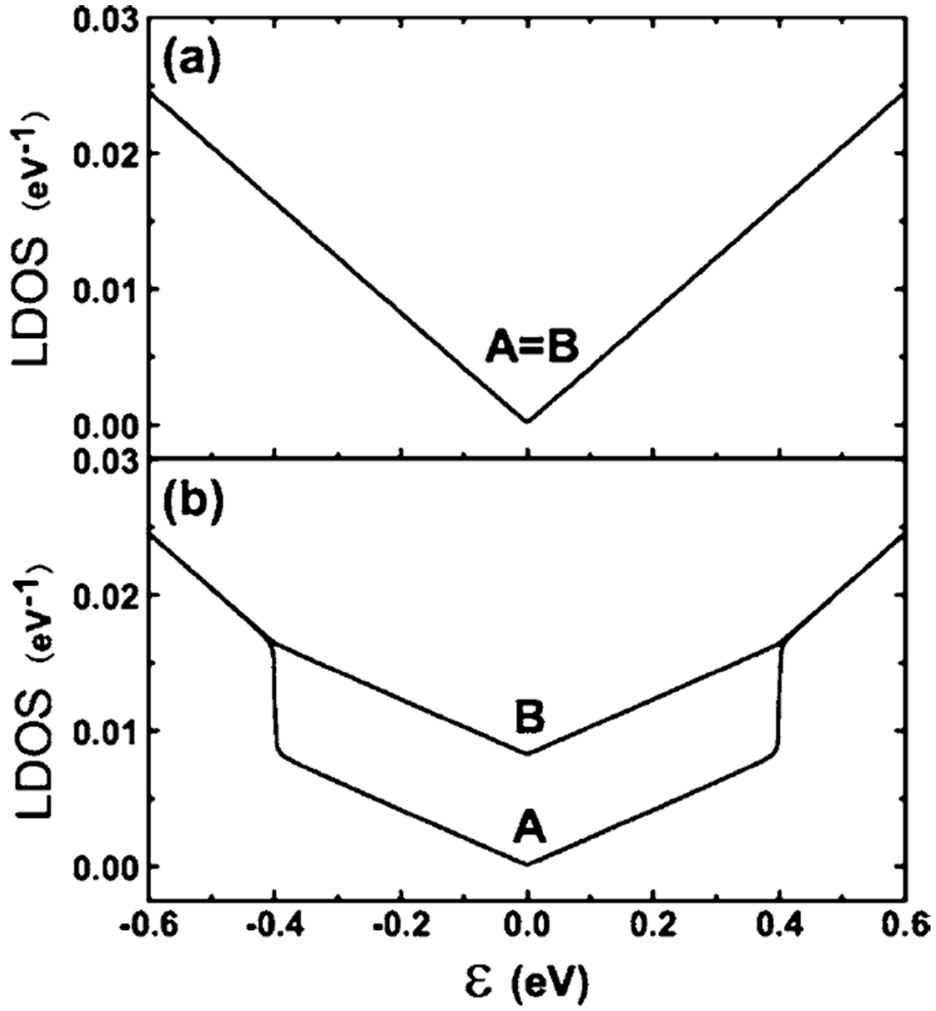

Figure 5.3: LDOS of monolayer and bilayer. (a) LDOS for A and B sublattice are equivalent for monolayer graphene. (b) LDOS for A and B atoms are non-equivalent for bilayer graphene. This figure is taken from Ref. [218].

up in STM measurements. Figure. 5.3 shows theoretically calculated LDOS for undoped bilayer graphene. Our STM is normally operated in the constant current tunneling mode. For bilayer this implies that both the A and B atoms will receive the same amount of tunneling current. Therefore:

$$I_A = I_B \tag{5.1}$$

Where I_i (i=A,B) is the tunneling current in A and the B atoms. The tunneling current in general depends on the LDOS, distance between the tip and the sample and the bias voltage (discussed in Sec. 2.1.1) and is given by:

$$I \propto exp\left(-\frac{2z}{\hbar}\sqrt{2mV_B}\right)\int_0^{eV}\rho_s(\varepsilon)d\varepsilon \tag{5.2}$$

where V_B is the barrier height, ρ_s is the sample density of states and z is the STM tip height. Substituting Eq. 5.2 in Eq. 5.2 for atoms A and B we get:

$$exp\left(-\frac{2z_A}{\hbar}\sqrt{2mV_B}\right)\int_0^{eV}\rho_{sA}(\varepsilon)d\varepsilon = exp\left(-\frac{2z_B}{\hbar}\sqrt{2mV_B}\right)\int_0^{eV}\rho_{sB}(\varepsilon)d\varepsilon \tag{5.3}$$

Rearranging,

$$z_B - z_A = \frac{\hbar}{2\sqrt{2mV_B}} ln\left(\frac{\int_0^{eV}\rho_{sB}(\varepsilon)d\varepsilon}{\int_0^{eV}\rho_{sA}(\varepsilon)d\varepsilon}\right) \tag{5.4}$$

Equation. 5.4 relates the height difference between A and the B atoms with their LDOS. The decay constant $\kappa = \sqrt{2mV_B}/\hbar$.

Figure 5.4(a)-(f) shows the atomic resolution (15 Å × 15Å) bias dependent STM imaging of bilayer EG. Figure 5.4(a) and (f) show a hexagon indicating A (yellow) and the B (blue) atoms. All images are acquired at a constant tunneling current of 100 pA, from the same terrace of a 3 ML_e thick sample. At low positive bias (0.2 V, Fig. 5.4(a) and 0.3 V, 5.4(b)) and low negative bias (-0.2 V, Fig. 5.4(d) and -0.3 V, 5.4(e)), every other atom (B) is imaged, suggesting asymmetry in the charge density of the neighboring atoms. This is also evident in Fig. 5.4(f) in which all six carbon atoms of the honeycomb lattice are imaged at higher bias (-0.6 V). This is a direct real space STM evidence of Bernal stacking in bilayer EG. Figure 5.4(g) shows a plot of STM height difference between A and B atoms of bilayer EG *versus* sample bias voltage. The red curve is the least square fit of the STM height difference ($z_A - z_B$) with:

$$LDOS_A(\tau_\perp, \alpha) = |V| + \alpha \tag{5.5}$$

$$LDOS_B(\tau_\perp, \alpha) = |V| + \alpha \tag{5.6}$$

for $|V| \geq \tau_\perp$.

$$LDOS_A(\tau_\perp, \alpha) = \frac{|V|}{2} + \alpha \tag{5.7}$$

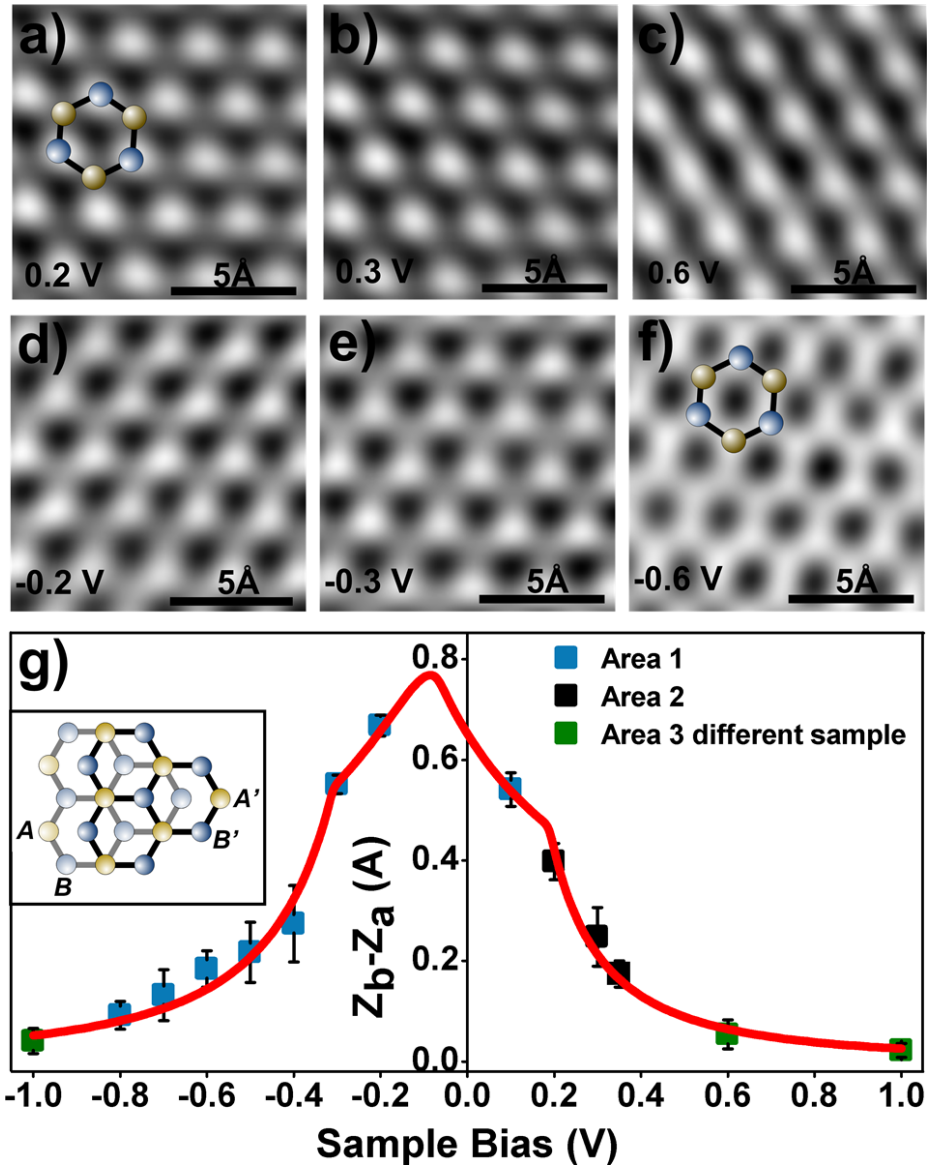

Figure 5.4: STM imaging of layer 2 shows bias dependent features indicating Bernal stacking. The hexagons show the approximate locations of the A (yellow ball) and B (blue ball) atoms of the honeycomb lattice. High resolution (15 Å × 15 Å) imaging at low bias ((a),(b),(d) and (e)), shows that A and B atoms are not imaged identically and a trigonal lattice is observed. At higher bias (-0.6 V), A and B atoms are imaged identically and a honeycomb lattice is evident in (f). (g) Plot of height difference between A and B atoms versus the sample bias voltage. The data was extracted by doing line profiles on the high resolution images in three lattice vector directions. Red curve is generated by doing by doing a least square fit on the experimental data. The fit generated interlayer coupling constant $\tau_\perp$=0.25 eV and *Dirac* point E_D=-0.065 eV with respect to the Fermi energy level. A background DOS contribution of 0.02 was used in the fitting. The inset shows the Bernal stacking in bilayer graphene.

$$LDOS_B(\tau_\perp, \alpha) = \frac{(|V| + \tau_\perp)}{2} + \alpha \tag{5.8}$$

for $|V| < \tau_\perp$.

Here α is a constant background density of states (this could potentially arise from defects). The best fit gives κ=0.8 Å, $tau_\perp$=0.25 eV, E_F=0.065 eV and α=0.02. Similar results have been obtained by Rutter *et al* [195] using low temperature (4.2 K) STM at NIST. They however observed the location of the Dirac point and the coupling constant as -0.3 eV and 0.4 eV, respectively in agreement with theory and experiments [55, 120, 228].

This discrepancy in the results could be due to several factors. In this model the tunnel matrix element is represented by a simple exponential function (see Sec. 2.1.1). This is a result of a small overlap between the wavefunctions on either side of the barrier. It is possible that this assumption is too simple. Recently, variation was reported for κ (it changes by a factor of 2) at low bias ($\sim \pm 0.1$ V) in exfoliated samples [226], but its value was essentially constant over the range of bias voltages employed here. It was also suggested that tunneling in graphene takes place via an inelastic tunneling channel. This channel is mediated by an out-of-plane 63 meV phonon. The electrons having energy less than the phonon energy tunnel elastically, and there is a giant enhancement (factor of 10) in conductance due to the inelastic phonon channel at energies higher than the phonon threshold energy. The inelastic channel enables coupling to graphene states with large parallel wave-vector $k_\parallel$. These states decay rapidly as a function of distance from the surface, thus the direct tunneling probability is small. The decay constant in such a situation is given by [207, 226]:

$$\kappa = \sqrt{\frac{2mV_B}{\hbar^2} + k_\parallel^2} \tag{5.9}$$

For higher biases the tunneling takes place through states that extend further into vacuum via virtual transitions. It is also possible to fit the data by including giant background DOS with "normal" values of E_F and $\tau_\perp$, which could come from defects and disorder in the sample. Si-face samples are known to have a high density of defects. The discrepancy in E_F, $\tau_\perp$ could also be related to the tip sample interaction, which is relatively unknown in case of graphene. Band bending effects [57, 64] can influence imaging due to highly intense electric field under the STM tip. Such high electric fields can locally gate dope graphene. Another possibility could be the presence

of defects or impurities in the immediate vicinity of the scanning area, which can locally alter the doping in graphene. Furthermore, recent ARPES measurements [228] suggest a small band gap (0.14 eV) in bilayer EG due to potential difference between layer 1 and layer 2, which is a result of difference in doping. A shift in the position of the Dirac point (-0.4 to -0.2 eV) as a function of thickness (1-3 layers) was also observed, which was associated with charges at the surface of the interface. Although there is no clear evidence that these mechanisms (or a combination of them) are responsible for the observed effects, multiple-bias imaging could provide a powerful technique to study electronic inhomogeneities at an atomic scale under room temperature conditions. Note that, interface states were not observed in layer 2 under varying bias conditions. Their contribution is expected to be minimal as they are offset by 5.8 Å from layer 2.

Scanning tunneling spectroscopy of bilayer EG is equally interesting. Figure 5.1(f) shows fifteen randomly chosen spectra in a 30 Å $\times$ 30 Å region. The averaged spectra in the inset shows a suppression (blue arrow) in the *dI/dV* near -0.4 V. Similar suppression in the *dI/dV* has been observed by other groups [34, 120]. Suppression in the *dI/dV* is believed to be the location of Dirac point, where a minimum in the density of states is observed. As discussed previously, in STM, the tunneling probability into the states near Dirac point is low, due to the inability to tunnel into states with large wavevectors. In my measurements, the energy location of the minimum with respect to the Fermi level roughly corresponds to the doping induced via charge transfer from SiC to graphene [228], although it is possible that the minimum is shifted 67 meV below the actual Dirac point due to the photon enhanced tunneling described above.

5.2 Defects

Recently there has been a giant wave of interest in the study of defects in graphene [35, 196]. Defects play an important role in defining the transport properties in an electronic material. In graphene, these defects or disorder gives rise to unique scattering events due to its singular electronic structure. Elastic scattering events in graphene at a local scale are of general interest to the scientific community. In an elastic scattering event, which could be mediated by a defect, an electron encounters a potential and undergoes a change in momentum, whereas its energy remains constant. The elastic scattering events in graphene are illustrated in the inset of Fig. 5.5. For simplification only

a 2D slice of the energy dispersion near the Fermi level E_F is shown. This gives as circles (blue) of radius q centered around the **K** and the **K'** points. There are two dominant scattering events in graphene, namely: intervalley and intravalley. Intervalley scattering process takes place between two in equivalent **K** points (red arrow). Intravalley scattering is shown by the magnified blue circle and represented by green arrow. Similar elastic scattering events have been studied extensively in carbon nanotubes [12, 146]. Following Ando's work [12], McEuen *et al* [146] showed that *long-range disorder* does not couple to the pseudospin component of the wavefunction, as it is seen as a constant at a small scale. The disorder potential seen by the electron is represented by Fourier components $\mathbf{V(q)}$, where $\mathbf{q} \ll \mathbf{K}$. The potential energy matrix can be written as [146]:

$$|\langle k'|V(r)|k\rangle|^2 = |V(k-k')|^2 \cos^2\left[\frac{\theta_{k,k'}}{2}\right] \tag{5.10}$$

where $\theta_{k,k'}$ is the angle between the initial and the final states. The intravalley scattering therefore will be suppressed in single layer graphene due to pseudospin and Berry's phase [28] of π [227]. In case of bilayer graphene since $\theta = 2\pi$ [169], Eq. 5.5 will give a non-zero contribution. The intravalley scattering will be allowed in bilayer graphene due to chirality of the heavy Dirac fermions [103].

In our STM studies we imaged various types of point defects on EG. These defects were found to exhibit unique electron density patterns in their immediate vicinity. These scattering patterns are due to interference of incident electron waves and the waves scattered from the defects [151]. The defects, themselves, were difficult to characterize, due unpredictable variability in the imaging at room temperature because of tip sample conditions. The scattering patterns however were found to be unique with a super period of ($\sqrt{3}\times\sqrt{3}$)R30°, and were observed to be common in all in-plane defects. Figure 5.5 shows a high resolution (200 Å × 200 Å) image of a defect on a layer 2 terrace (500 Å). This is an usual defect imaged by STM and it is difficult to determine the structure of the defect by STM alone. The inset is a magnified (25 Å × 25 Å) image of the region enclosed by the white box. A scattering pattern with donut shaped rings along with the graphene lattice can be observed in this image. The period of this scattering pattern represented by red diamond is ($\sqrt{3}\times\sqrt{3}$) with respect to the graphene lattice. Three black hexagons represent approximately the graphene honeycomb lattice. The scattering pattern is also found to be rotated by 30° with respect

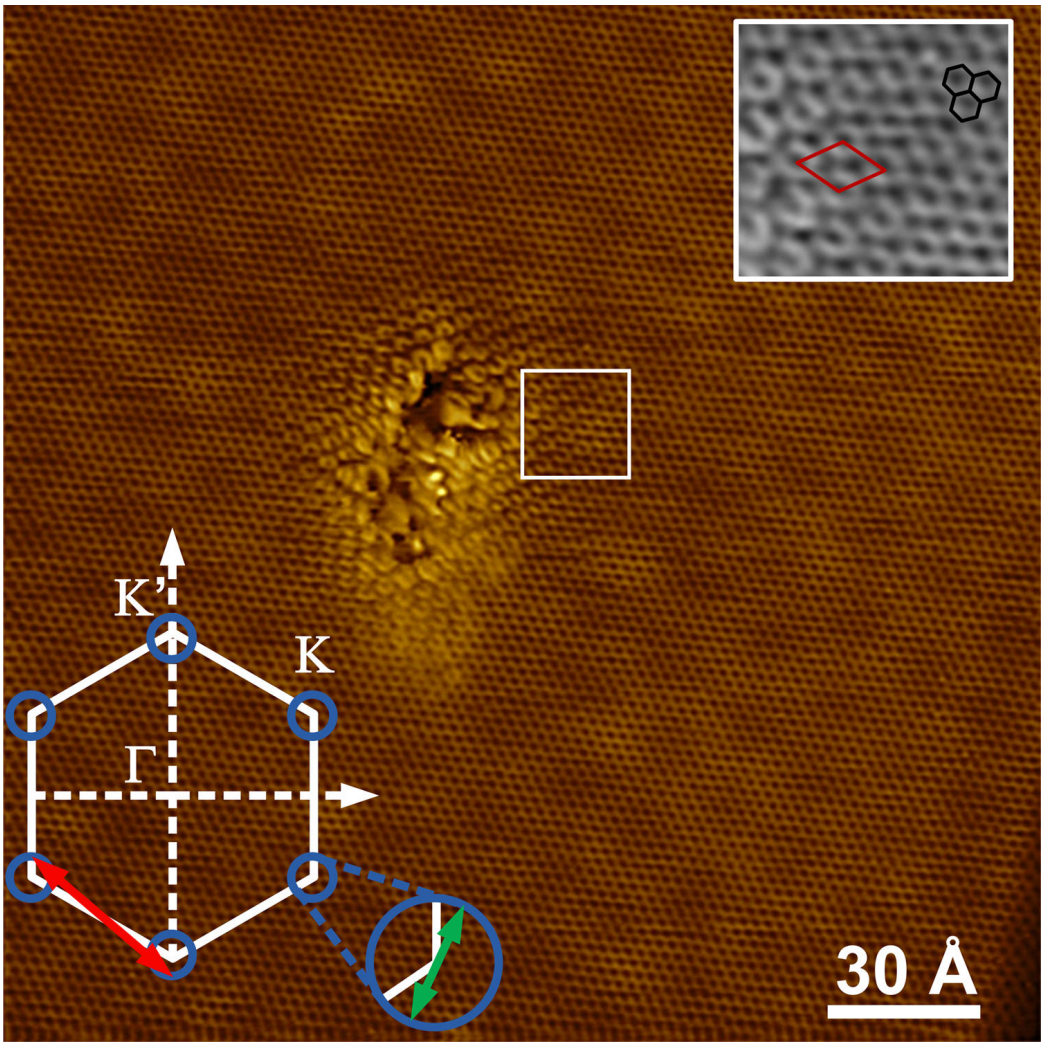

Figure 5.5: Defects in EG give rise to unique scattering patterns. Illustrtation in the image shows a 2D slice of the energy dispersion with intervalley and intravalley scattering events. High resolution image (200 Å × 200 Å) of layer 2 epitaxial graphene showing defect in the lattice and a scattering pattern (white box) (0.3 V, 100 pA). Inset shows the magnified image of the ($\sqrt{3}\times\sqrt{3}$)R30° scattering pattern (red diamond) with donut shaped rings. Three hexagons represent the graphene honeycomb lattice.

to the graphene lattice and its decay length was found to be ~30 Å. Theoretical calculations predict similar scattering patterns being generated by point defects in graphene [151]. High resolution STM measurements on HOPG have imaged similar scattering patterns at the defect sites [138, 163] and step edges [109, 110, 164, 165]. Recent low temperature (4.2 K) STM measurements by Rutter *et al* [196] have characterized some of the commonly found in-plane atomic scale defects in EG.

An interesting problem is the effect of multiple heating cycles on the quality of graphene films.

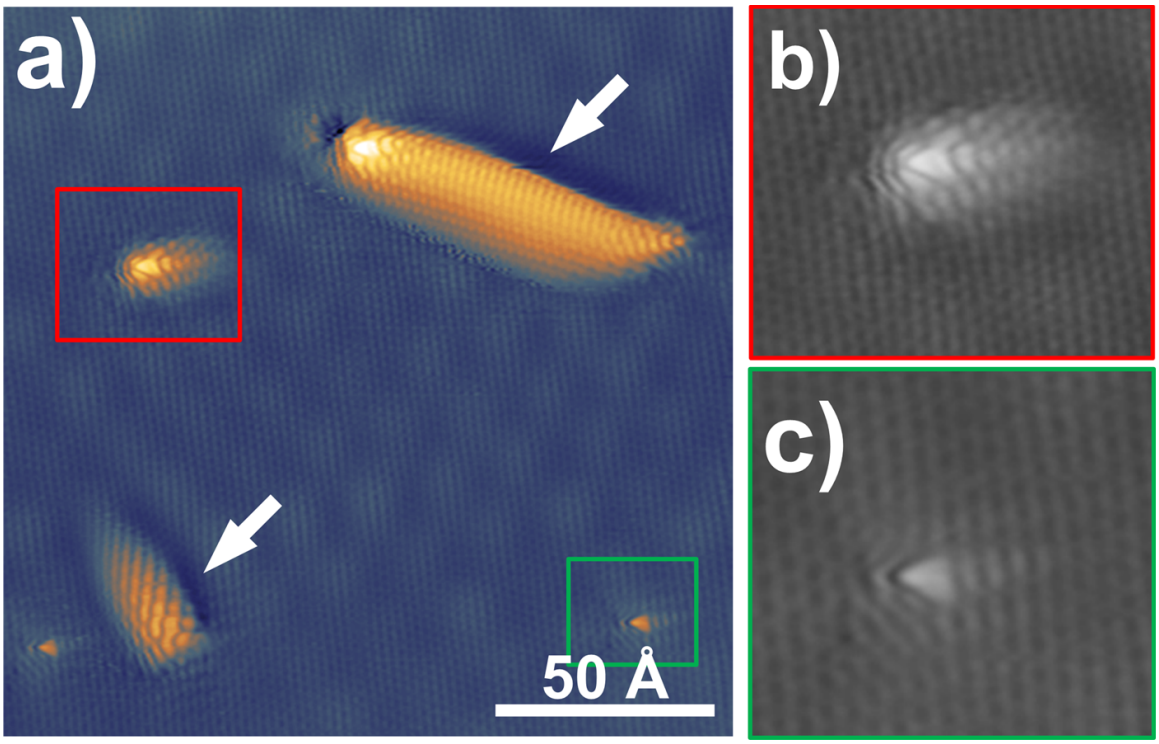

Figure 5.6: Defects on a 2 ML_e reheated (1200 °C) EG sample. (a) 160 Å × 160 Å high resolution image of defects on layer 2 shows five defects (-1 V, 100 pA). Bigger subsurface or "boil" (white arrow) like feaures appear after reheating the sample. These could be due to unzipping and zipping effect at the defect sites due to reheating. (b) and (c) are magnified images of regions enclosed by red and green box in (a) respectively. Defect (c) is similarly shaped as (a) and has an additional topographic deformity.

Graphene is a very robust fabric, however EG has higher density of in-plane defects as compared to its mechanically exfoliated graphene counterpart. Annealing EG close to the graphitization temperature might give us an opportunity to observe interesting effects at these sites. Figure 5.6(a) is high resolution image (160 Å × 160 Å) of layer 2 graphene terrace on a 2.0 ML_e thick. The sample was reheated to a temperature of 1200 °C twice after graphitization for cleaning. In this image (Fig. 5.6(a) acquired at -1 V one can observe five defects in the graphene lattice out of which two seem like large boils or sub-surface features (white arrows). In these larger defects, graphene seems to have enveloped something underneath, attaining a curvature of some sort. One possible explanation is that graphene is draping over some sub-surface feature. It is also possible that since the defect is a low energy site, graphene gets unzipped at this site at temperatures ~1200 °C. I believe carbon atoms get attached to the free edge and when the temperature is reduced again, the

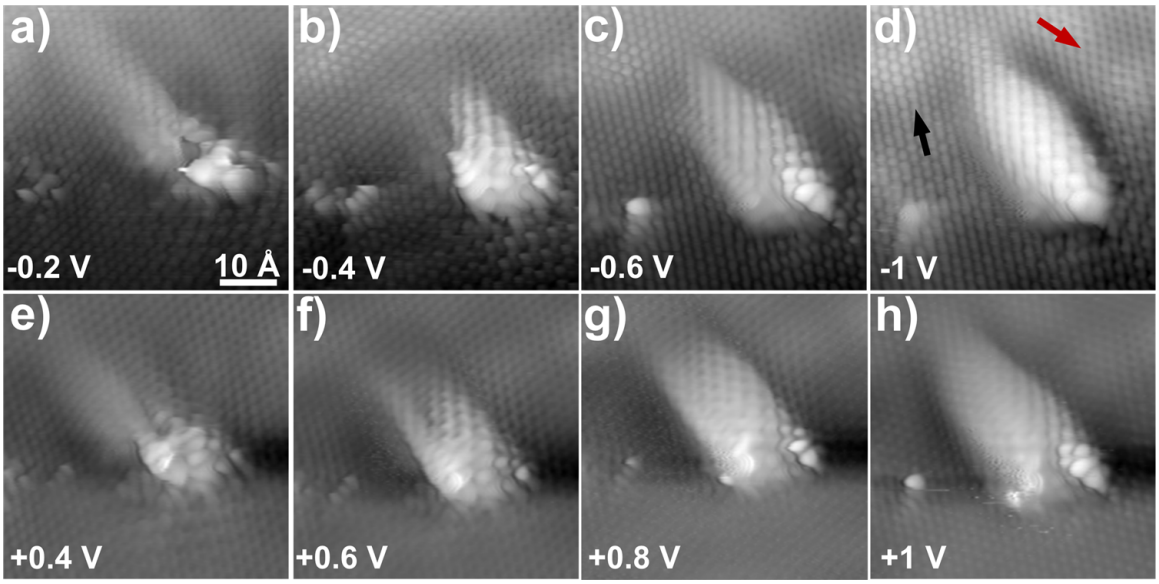

Figure 5.7: High resolution (60 Å × 60 Å) STM imaging on the layer 2 defect in Fig. 5.6 shows unique electronic and structural changes with change in bias voltage. (d) and (h) A unique curvature in topography is seen at higher bias (see figure for values) due to defect. (c), (f) and (g) At lower bias, the curvature in graphene is suppressed. (a), (b) and (e) The deformity in the topography due the defect is highly suppressed at low biases. Scattering is seen at all biases (100 pA) in the vicinity of the defect. In (d) graphene images differently (red and black arrow) on either side of the defect due to change in vertical alignment of A and B atoms in layer 1 and -2.

defect seems to acquire a curved surface. All this is evidenced from images in defects highlighted by the enclosed red box, and magnified in Fig. 5.6(b) as well the defect which is enclosed by a green box and magnified in Fig. 5.6(c). At first after graphitization, only defects such as the ones Fig. 5.6(c) were imaged with STM. Therefore, it seems plausible that these defects were the areas where graphene unzipped during reheating. On closer inspection one can observe the similarities in the shape (tip) of the defects (b) and (c). It seems highly likely from this data that these bigger defects are not subsurface features over which graphene drapes but rather they are ”boils” in the graphene lattice.

Figure 5.7 shows the bias dependent imaging of the defect observed in the bottom left portion of Fig. 5.6(a) (white arrow). These high resolution images (60 Å × 60 Å) were not acquired simultaneously. I would also like to point out that no tip switching was observed during these scans. In these images, one can observe changes in the shape of the bigger defect as a function of bias

voltage. At higher bias (Fig. 5.7(d) and (h)), the defect is observed as a boil in the graphene topography. Scattering is observed in the vicinity of the defect (points in the southwest direction). At a slightly lower bias voltage (Fig. 5.7(c), (f) and (g)), a suppression in the curvature of the defect is observed. On further reducing the STM bias voltage (Fig. 5.7(a), (b) and (e)), we observe that the boil is highly suppressed in contrast to the imaging at higher bias. Furthermore a slight ripple in the graphene fabric concentrated around the defect is evident in images acquired at -0.2 V and +0.4 V. These observation could be an electronic effect mediated by changes in the local electronic structure due to the defect. There is another possibility. It has been suggested that during low bias (<0.5 V) STM imaging on HOPG [170], the tip is in contact with the sample. This could also be true in case of graphene, although the EG samples are intrinsically *n* doped. In constant current tunneling mode, a lower bias voltage would bring the tip closer to graphene. Therefore it is possible that at low bias, since the STM tip could be in contact with the sample, the boil is getting compressed as the tip scans across.

In Fig. 5.7(d), the bilayer graphene lattice is imaged differently (red and black arrow) on either side of the defect. The raised defect has introduced a unique curvature in layer 2 graphene. It is possible that the layer 2 graphene lays differently on layer 1 on either side of the boil. This would result in a different vertical alignment of A and B atoms of layer 2 with respect to layer 1 on the sides of the defect.

5.3 Step Edges

Fully graphitized SiC substrates exhibit a topography which has a high density of SiC (2.5 Å) steps. As discussed in Chapter. 3, substrate roughening during the growth results in smaller domains with complex geometrical structures and pits in the sample extending all the way down to the substrate [87]. Table. 5.1 lists some of the step heights observed in EG on SiC(0001) by STM.

Figure 5.8(a) shows a 120 Å × 100 Å image around a SiC step. In this image, layer 2 graphene is observed on either side of a 2.5 Å SiC step. Also evident is the (6×6) period superimposed on the graphene lattice. The inset shows a rendered (bronze color) image of the 25 Å × 25 Å yellow boxed region on the step edge. The graphene blanket is observed to continues over this step and no scattering is observed at this location. In fact the robust nature of the graphene was evident in

Graphene Step Edges	STM Height (Å)
layer 0/layer 1	2.4 ± 0.2
layer 1/layer 2	3.4 ± 0.3
layer 1 island/layer 0	2.5 ± 0.3
layer 2 island/layer 1	variable

Table 5.1: Different step heights observed in epitaxial graphene (EG) on SiC(0001).

our other data where it appeared to go over any deformities in the topography. Epitaxial graphene layers were always observed to be continuous over step edges, whether over substrate steps, or steps between different EG layers. This is also the case for small raised islands of layer 2 material occasionally observed within an otherwise layer 1 terrace. Figure 5.8(b) shows a 150 Å × 50 Å image of a raised layer 2 island in a sea of layer 1 graphene. A close inspection of the image reveals that the step edges (red lines) follow the direction of SiC reconstruction. The angle between the two red lines along the step edges is observed to be 120 °C. Also evident in this image is some scattering (discussed below) in top right portion of the image due to the presence of a layer 0 region (not shown in the image). On the whole, graphite step edges were observed to be less sharper than the SiC steps.

Figure 5.8(c) shows a 80 Å × 160 Å image of a layer 1 region bordered (top left section) by a layer 0 region. In this image scattering is observed near the step edge (blue arrow). Fujita *et al* [73] were the first to theoretically predict the presence of the local electronic states at the zigzag edges in graphene ribbons with tight binding calculations. We can observe in this image that the coexistence of the zigzag and armchair edges makes it difficult to isolate the electronic properties of either of them to the LDOS. Interface states can be observed in layer 0. The inset shows magnified image of the blue boxed region in which ($\sqrt{3}\times\sqrt{3}$)R30° pattern is evident. The pattern extends to 30 Å from the step edge. layer 0 is structurally and electronically different from layer 1 as discussed in previous sections. Variety of experiments [92, 100, 120, 229] have not been able detect graphene in layer 0. It therefore seems plausible that there is a discontinuity in the graphene fabric at this step edge. The ($\sqrt{3}\times\sqrt{3}$)R30° pattern observed at this hydrogenated step edge is similar to scattering observed in hydrogenated graphite step edges [109–111]. In our samples, ($\sqrt{3}\times\sqrt{3}$)R30° scattering

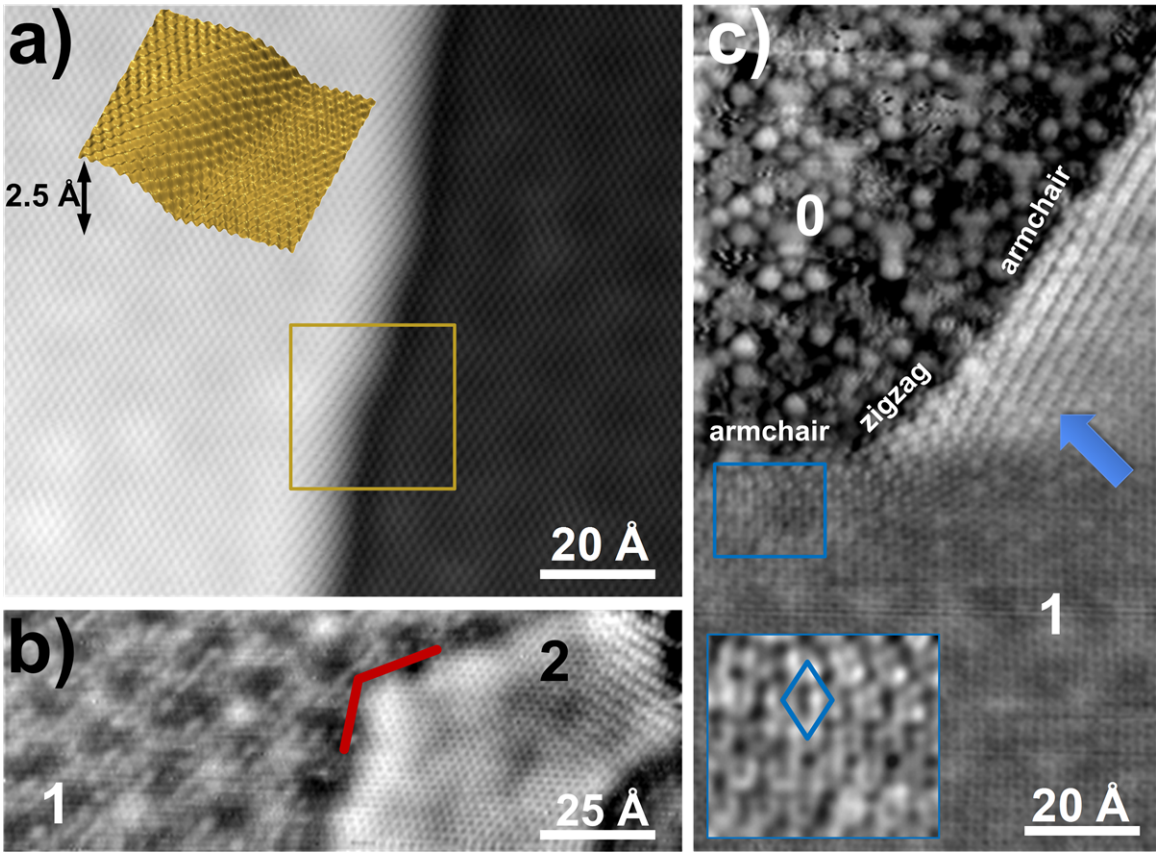

Figure 5.8: STM imaging of step edges in EG on SiC(0001). (a) 120 Å × 100 Å image of a graphene covered SiC (2.5 Å) step edge (0.3 V, 100 pA). Regions on either side of the step edge are covered with layer 2 graphene. (6×6) period (20 Å) is seen superimposed on either side of the step edge. Inset (rendered image) of the yellow boxed region on the step edge shows the continuity of the graphene sheet over the step edge. (b) 150 Å × 50 Å image shows a raised layer 2 island in a sea of layer 1 graphene (1.0 V, 100 pA). The step edges (red lines) follow the direction of the SiC reconstruction. The angle between the red lines is 120 °C. Top right section of the image shows some scattering due the presence of a layer 0 region (not shown in the image). (c) 80 Å × 160 Å image shows scattering (green arrow) at layer 1 (step up) layer 0 step edge (0.2 V, 100pA). Scattering indicates a discontinuity in the graphene fabric at the step edge. The inset shows ($\sqrt{3}\times\sqrt{3}$)R30° scattering pattern (blue diamond).

is also observed at the edges of layer 1 islands in layer 0 terraces. The continuity of graphene films over steps and surface deformities is useful for device applications.

5.4 Conclusions

In this chapter I showed unique structural and electronic properties of EG on SiC(0001) with STM and STS. I discussed the properties and differences between the commonly observed layers in EG, namely: layer 0, layer 1 , layer 2. Layer 0 is the interface between SiC and overlying graphene

films with no evident graphene-like lattice. Tetramers and hexagonal shaped features were found to be abundant in layer 0. I also showed the bias dependent imaging of layer 1 where a graphene honeycomb lattice was seen at low bias (0.2 V) and subsurface features replaced the graphene lattice at high bias (1 V). These features were commonly found to be tetramer and hexagonal shaped with tetramers having a relatively higher population density than hexagons. I also showed the bias dependent STM imaging of layer 2 graphene. The graphene imaged as a triangular lattice at low bias and a honeycomb lattice at high bias. The *dI/dV* spectra at room temperature showed a unique suppression in DOS near -0.3 V, which could be the location of Dirac point.

I showed the ($\sqrt{3}\times\sqrt{3}$)R30° pattern due to scattering of electron waves from a point defect. I also talked about the effect of high temperature (~1200 °C) heating on the quality of the graphene samples. I also showed "boil-like" features originating from the defect site after reheating. Bias dependent imaging showed suppression in the curvature of the "boil" at low bias conditions. I showed the continuity of graphene lattice over subsurface deformities and step edges except at a layer 0/layer 1 step edge. Scattering was seen at such locations with a ($\sqrt{3}\times\sqrt{3}$)R30° period.

CHAPTER VI

RAMAN SPECTROSCOPY OF EPITAXIAL GRAPHENE

Historically, Raman spectroscopy has played a significant role in the structural and opto-electronic characterization of graphitic materials providing us qualitative information about defects, stacking of graphene layers and finite size of the crystallites. It has been applied successfully for the past few decades for characterization of highly oriented pyrolytic graphite (HOPG), kish graphite (and other natural forms), fullerenes, carbon nanotubes, nanographene ribbons, glassy carbon, carbon fibers and mechanically exfoliated graphene. Some of the modern Raman analysis techniques make it possible to identify the edge defects (armchair/zigzag) [37, 38]. The advantages of such a technique are immense since the focus is now shifting towards graphene nanoribbons where the nature of the edge along with the width plays an important role in shaping the electronic properties. Lately, Raman spectroscopy is being used as a powerful tool to study and identify different layers [68, 84] in mechanically-exfoliated graphene samples. Furthermore, since the epitaxial multi-layered C-face graphene exhibits linear dispersion (quasi 2D graphene) [93, 119] due to rotational stacking faults, this technique could be a powerful tool to analyze the stacking disorder in this and other new graphene-based material systems.

6.1 Phonons in Graphene

Phonon dispersions in graphene are unique in many ways and are responsible for some of its exotic properties. The 2D graphene lattice has two carbon atoms per unit cell. This gives us six phonon dispersion branches. Three phonon bands are acoustic *(A)* and three are optical *(O)*. In case of both optic and acoustic phonon modes one is out-of-plane *(Z)* and the other two are in-plane, longitudinal (L) and transverse (T). The six phonon modes LO, TO, ZO, LA, TA and ZA are plotted along the high symmetry points $\mathbf{\Gamma K}$, $\mathbf{KM}$ and $\mathbf{M\Gamma}$ in Fig. 6.1. The inset in Fig. 6.1 shows the high symmetry points $\mathbf{\Gamma}$, $\mathbf{K}$ and $\mathbf{M}$ in the 2D Brillouin zone (BZ). At the $\mathbf{K}$ point, the LO (optical) and LA (acoustic) branches meet resulting in a doubly degenerate phonon with $\mathbf{E'}$ symmetry. The phonon modes *LO* and *TO* are degenerate at $\mathbf{\Gamma}$ point and they are Raman active from group theory. The phonon mode

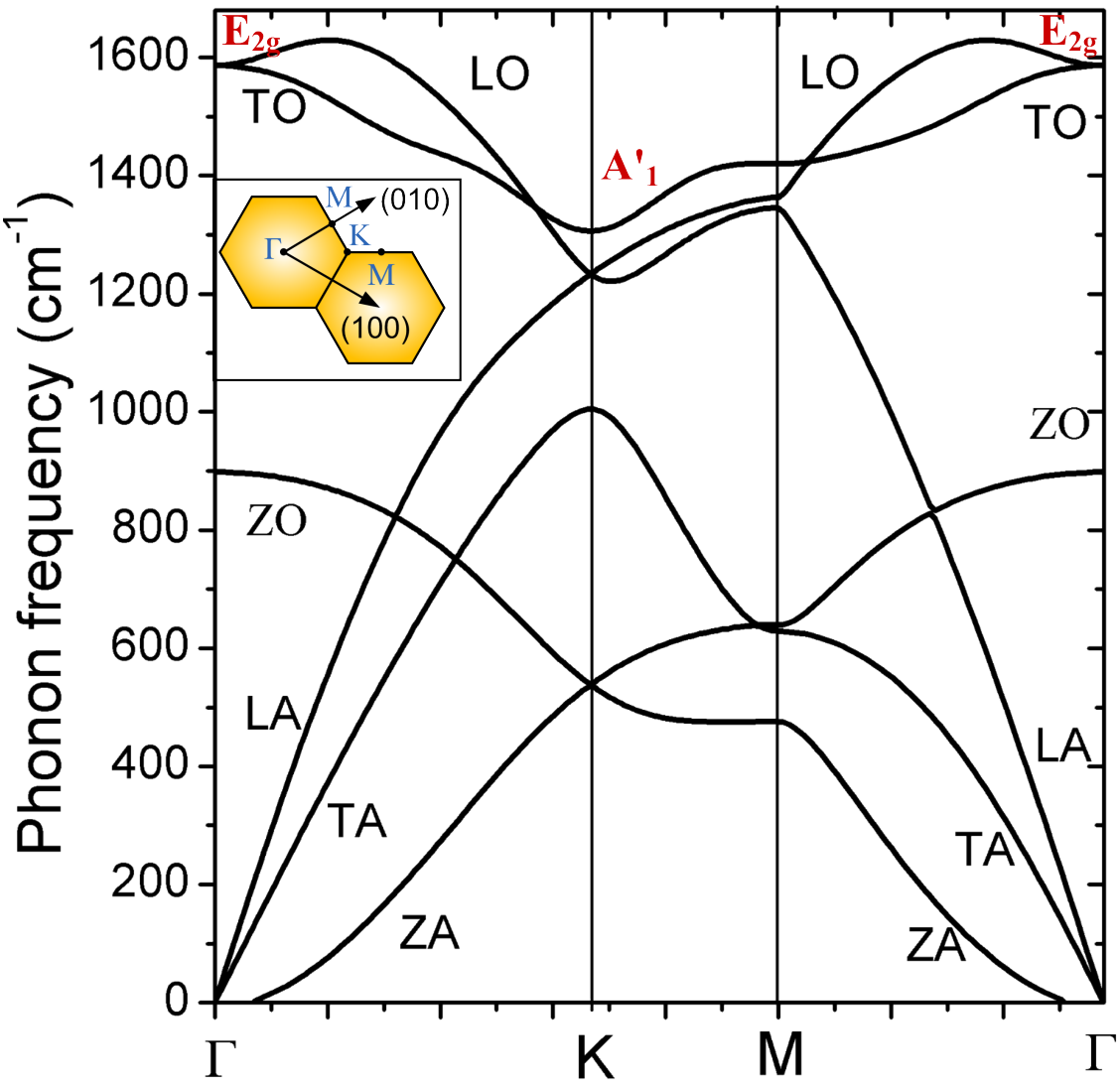

Figure 6.1: Calculated phonon dispersions along **ΓK**, **KM** and **MΓ** directions. The optical phonon modes are in-plane *LO* and *TO*, and out of plane *ZO*. The corresponding acoustic phonon modes are *LA, TA* and *ZA*. Modes *LO* and *TO* are Raman active and *ZO* is infrared active. Enhanced electron-phonon coupling takes place at A_1' and E_{2g} (see text). The inset shows the graphene Brillouin zone with **Γ**, **K** and **M** high symmetry points. Figure provided by Dr. J.A. Yan.

ZO is infrared active. Along the **Γ**-**M** direction the *LO* and *TO* branches have $\sum_1$ and $\sum_3$ symmetries respectively. Along the **Γ**-**K** direction *LO* and *TO* branches have $\mathbf{T_3}$ and $\mathbf{T_1}$ symmetries respectively. The unique dispersions of the LO and TO phonon branches near the **Γ** and **K** are explained in the following few sections.

6.1.1 Electron-Phonon Coupling and Kohn Anomaly

It is known that strong electron-phonon coupling (EPC) can adversely affect ballistic transport in carbon nanotubes [225]. As mentioned in the previous section, *TO* and *LO* phonon modes are degenerate at the **Γ** point. There is significant bond distortion in the LO mode (see Fig. 6.2) as nearest neighbors vibrate opposite to each other. This vibration can couple to the electronic states through intravalley (same *Dirac* cone) scattering process following the Raman fundamental selection rule (**q**~0). This suggests a strong EPC for this mode at the **Γ** (E_{2g}). An enhanced EPC is also expected at the highest *TO* A_1' at the **Γ** point due to intervalley scattering.

Phonon modes in a lattice are typically derived by setting up force constant equations. Anomalous behavior of certain phonon modes near Brillouin zone boundary renders such an approach ineffective at these points. The electronic conduction (π^*) and valence bands (π) in graphene are located at the two inequivalent points **K** and **K'** and have a zero band gap. These points are connected by vector **K**, since

$$\mathbf{K'} = \mathbf{2K} \tag{6.1}$$

Now, it is known that electrons partially screen the atomic vibrational states. Depending on the shape of the fermi surface, changes in the phonon dispersion near certain **q** points of the BZ are observed due to rapid changes in screening (for example metals and graphene, a semimetal). This anomalous behavior near certain points near the Brillioun zone is called the *Kohn anomaly*. Furthermore, as pointed out by Kohn [112] only wavevectors **q** that relate two electronic states (**k** and **k′**=**k**+**q**) on the Fermi surface can manifest Kohn anomaly. Therefore, from Eq. 6.1 Kohn anomalies can occur at **q**=**Γ** or **q**=**K**. In graphene, Kohn anomalies occur as two sharp kinks in the phonon dispersion (see Fig. 6.1). It was shown by Piscanec *et al* [188] that the slope of the kinks is proportional to the square of electron-phonon coupling.

6.2 Modes in Graphene

There are several phonon modes that can propagate in graphene. However we are only going to discuss three primary modes namely G, D and 2D (or G') . According to the Raman fundamental selection rule **q**~0, all unit cells must vibrate with the same phase. The second order modes are

allowed as **q+(-q)**=0. Graphene contains two carbon per unit cell and group theory predicts two in-plane normal modes namely E_{2g} and B_{2g}. E_{2g} mode is Raman active and B_{2g} is optically inactive.

6.2.1 G Mode

The G mode typically observed at $1580cm^{-1}$ [68] is a Raman allowed mode (**q**~0) exhibited by graphene and its derivatives and other carbon-based forms. Its presence in a Raman spectrum indicates an sp_2 network of carbon atoms. The G peak is due to a one phonon process involving Γ-point optical phonons. These phonon modes namely *LO* and *TO* (E_{2g} symmetry) are doubly degenerate at the Brillouin zone center (see Fig. 6.1) and Raman active for a graphene network. Figure 6.2(a) illustrates the bond stretching process in sp_2 bonded carbon atoms for the G peak.

6.2.2 D Mode

The *D* mode is a Raman disallowed mode and it propagates due to relaxation of the Raman fundamental selection rule, **q**~0 for perfect lattice. This is due to deviation from the ideal graphene lattice lying within the monochromatic laser beam radius (1 μm). The deviations from the ideal graphene include but are not limited to atomic scale defects, finite domains, nature of the edge and stacking faults. Under such disorder, the mode propagates and the lattice can "breathe". Figure 6.2(b) shows the real space illustration of this breathing mode. As discussed previously, the Kohn anomaly resulting from electron-phonon coupling increases the phonon dispersion [188] near the Γ, K points. The *LO* phonons give rise to defect-induced Raman features [66]. This mode is activated by a double resonance process. Vidano *et al* [214] suggested that the D-band is dispersive in nature and the D-band frequency was found to be dependent on the laser excitation energy. Previously, a maximum in the phonon density of states was believed to be the origin of D-band. It was shown that upshift in frequency of the D mode as a function of change in laser energy is linear with a slope of 50 cm^{-1}. The D-band originates from an intervalley double resonance process that involves the two inequivalent points **K** and **K'** of the 2D graphene BZ. This mechanism was proposed by Baranov *et al* [20] and Thomsen *et al* [140, 208] later calculated the scattering cross section of the double resonance process.

Figure 6.2(c) illustrates the intervalley (between inequivalent **K** and **K'** points) double resonance (DR) process for D mode. In Fig. 6.2(c1) an incident photon resonantly excites an electron in the

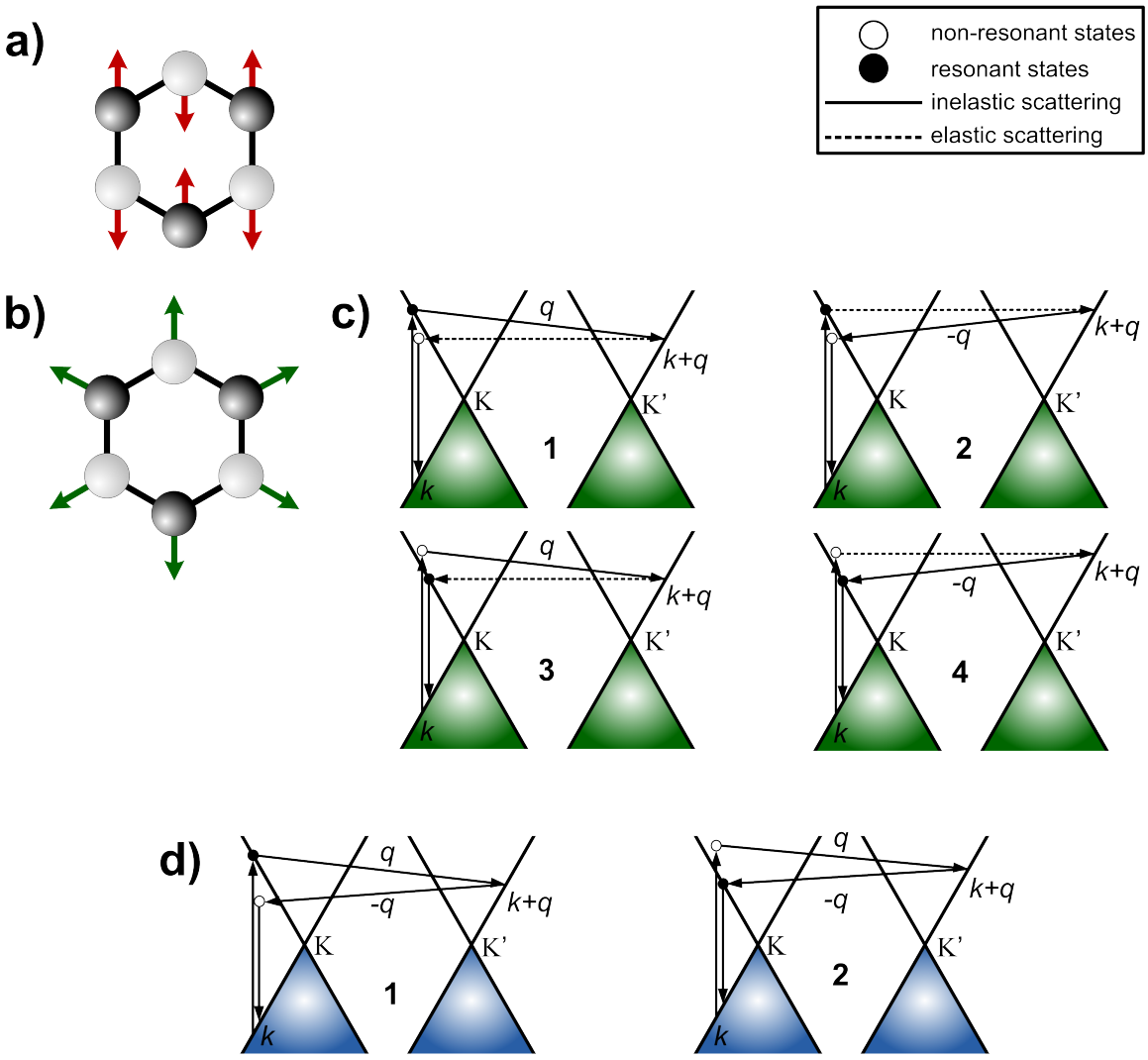

Figure 6.2: (a) Bond stretching process in Raman allowed G mode. (b) D mode breathing process which is a Raman disallowed mode and is only seen in samples having disorder or defects. (c) One phonon double-resonance intervalley process for D mode (see text). The process involves two real electronic transitions, one virtual transition, one elastic and one inelastic scattering process. (d) Two phonon double-resonance intervalley process for 2D (G') mode (see text). The process involves two real electronic transitions, one virtual transition and two inelastic scattering processes.

valence band (π) to conduction band (π^*). The electron then scatters inelastically by emitting a phonon of momentum $\hbar\boldsymbol{q}$ to a conduction band state in **K'**. The electron is further backscattered by a defect through a non-resonant elastic process. The electron then recombines with the hole by a non-resonant process. In the second process, (Fig. 6.2(c2)) the inelastic backscattering from defect due to emission of phonon ($-\hbar\boldsymbol{q}$) occurs, after the elastic scattering from **K** to **K'**. In processes (c3) and (c4) the $\pi - \pi^*$ transition due to incident photon is non-resonant. Electron-hole recombination

process is elastic. In process (c3) backscattering is elastic, and occurs after the inelastic scattering of the electron. In the double resonance (DR) process either the initial or the final **k** state is a real state and **k+q** is always a real electronic state. The two real electronic transitions namely: the vertical transition between the hole state and the electron state, and the intervalley transition makes it a double resonance process.

As seen previously (in Sec. 1.2.2.3) there can be two different kinds of edges in graphene, *armchair* and *zigzag*. Localized edge states are observed in *zigzag* edges, whereas no electronic states are observed for the *armchair* edge. Raman spectra can be used as tool to study edge structure in graphene [38]. The edge behaves as a defect by backscattering the electron in the DR process. In the backscattering process, the step edge related defect has a 1D character. It can transfer momentum only in the direction perpendicular to the step edge. Furthermore, the strength of scattering is sensitive to the edge termination. The D band is about four times more intense in armchair configuration compared to zigzag configuration [38]. The direction of the transferred momentum vector in the case of armchair configuration satisfies the conditions for the DR process by defect scattering.

The size of the domain also influences the *D* mode. X-ray and Raman measurements done by Tuinstra *et al* [209] on several graphitic samples suggested an inverse relation between the domain size L_a and I_D/I_G (ratio of *D* and *G* peak intensity). This relationship (Equation. 5.1, fix this later) was determined experimentally [108] by using 2.41 eV laser line on different graphitic systems and later by Cancado *et al* [39], who used a series of different laser lines.

6.2.3 2D Mode

The 2D mode, also known as G', appears at a frequency that is the first overtone of the D band. It is the second order mode in the Raman spectra and is an allowed mode (**q+(-q)**=0). This mode is very sensitive to the stacking order in graphite and its analysis can be extended to multilayer graphene with rotational stacking faults.. It has been shown by Nemanich *et al* [160] that the spectral shape of the 2D peak changes from one peak to two peaks in poly- and single-crystal graphite respectively. This mode is highly dispersive and a linear relation (slope $100cm^{-1}$) was observed between the upshift and the change in laser energy [214]. The mechanism for this mode was first proposed by Baranov *et al* [20] and later by Thomsen *et al*[208]. The mode orginates from a double resonance

process between the inequivalent **K** and **K'** points.

Two phonons are involved in this double resonance process as shown in Fig. 6.2(d). In the first process (d1) an incident photon resonantly excites an electron from π to π^* band. The electron then scatters inelastically by emitting a phonon of momentum $\hbar\boldsymbol{q}$ to a conduction band state in **K'**. The electron backscatters inelastically by emitting a phonon (-$\hbar\boldsymbol{q}$). The electron then recombines with the hole (at **k** state) by a non-resonant process and emits a scattered photon. In process (d2), the $\pi - \pi^*$ transition is non resonant and the electron-hole recombination after two scattering processes (phonons $\hbar\boldsymbol{q}$ and -$\hbar\boldsymbol{q}$) is resonant.

The 2D mode is very sensitive to the stacking order in graphene, as energy bands evolve with the number of layers and stacking order [119]. Changes in the both spectral shape and intensity of the 2D peak have lately been used a powerful tool to count the number of layers in exfoliated graphene samples [68, 84].

6.3 Experiment

Raman spectroscopy can be used to distinguish and characterize mechanically exfoliated graphene since this material has a very characteristic *G*-band peaked at 1590 cm_{-1} and a *2D*-band at 2720 cm_{-1} [68]. Moreover, changes in the spectral shape and intensity of *2D*-band can be used as tool for monitoring thickness [68] of such samples. Several different thickness epitaxial graphene samples were grown on *n*-doped 6H-SiC(0001) under ultra-high vacuum (UHV) conditions (base pressure $< 1 \times 10^{-10}$ Torr). The aim was to extract and possibly isolate layer dependent Raman spectra, in a manner similar to exfoliated graphene samples. SiC samples were etched at 1500 °C in 1-atm of 5% H_2/95% Ar gas mixture to remove scratches from the surface (see Fig. 3.1). A reference sample of highly oriented pyrolytic graphite(HOPG) was obtained from SPI supplies [4]. The substrate is then annealed in UHV by electron-bombardment heating (max pressure $\sim 10^{-8}$ Torr) at a temperature >1200 °C for EG growth. It is possible to control the epitaxial graphene layer thickness to a certain degree by adjusting the growth temperature and time. The average thickness was determined by Auger electron spectroscopy (AES) from different locations on the sample (typically >4 spectra). The thickness reported in this section includes the contribution of the carbon in the interface (~0.8 ML_e), please refer to Sec. 3.2 for more details about AES thickness measurements.

The characterization was done *in situ* with low energy electron diffraction (LEED) and scanning tunneling microscopy (STM).

Raman measurements were done ex situ in a Renishaw RM 1000 Raman microscope at Material Science and Engineering department (see Sec. 2.4.2) at room temperature under atmospheric conditions. Raman spectra was done with Argon laser at a fixed wavelength of 514.5 *nm* (2.41 eV) and exit power below 3 mW. The laser is focussed on the EG surface to a spot diameter 1 μ m using a 50× objective. Under these conditions the spectral features scale linearly with intensity. The high intensity laser penetrates deep and there is significant contribution from the SiC bulk. For background subtraction, Raman spectra were acquired from ungraphitized H_2 etched control sample by focussing the laser into the SiC bulk below the surface.

6.4 Analysis and Discussion

Figure 6.3 shows Raman spectra acquired from the SiC bulk and from samples with 1.8 and 2.7 ML_e Auger thickness. Spectra are normalized to have equal intensity at the SiC edge near 1950 cm^{-1}. In the 2.7 ML_e sample, clear differences are observed from SiC spectra. There are additional pronounced peaks at 1360, 1590, and 2720 cm^{-1}. To isolate these features, the SiC and a linear background was subtracted from the spectra. The background-subtracted spectrum is shown for comparison in Fig. 6.3. Three major peaks are identified as due to graphene: the *D*-modenear 1360 cm^{-1}, the *G*-mode at 1590 cm^{-1}, and the *2D*-mode near 2720 cm^{-1} [67, 68]. As mentioned previously, the G peak is due to a one phonon process involving Γ-point optical phonons, and is characteristic of sp2-bonded carbon [68], while a single-lorentzian 2D peak has been shown to be a signature of single-layer graphene [68]. The *2D* peak for the 2.7 ML_e sample is well-fit by a single Lorentzian with a full-width-half-maximum (FWHM) of 47 cm^{-1} (the FWHM of the *2D* peak for the mechanically exfoliated graphene is known to be approximately 30 cm^{-1} [68]). The D peak or the breathing mode is due to a resonance process involving two inequivalent K and K′ points in the brillouin zone of graphene [67, 186]. The D peak is not allowed in ideal graphene due to the large wave-vector of the K-point phonon involved. Its presence is an indication of disorder, such as the finite size domains, atomic scale defects [39] and armchair-type edge defects [37, 38]. The D and 2D bands are respectively, one-phonon *plus* elastic scattering and two-phonon double resonance

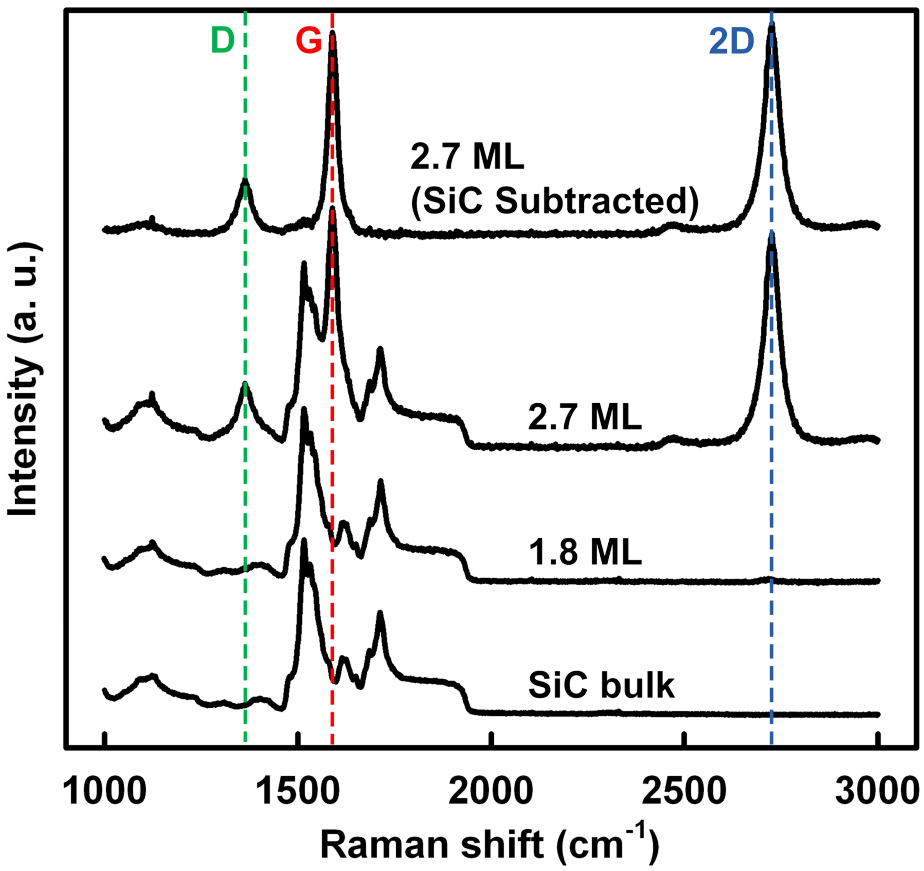

Figure 6.3: Raman spectra showing the subtraction of the SiC background from the Raman raw data. Raman spectra for and SiC and two different thickness (1.8 ML_e, 2.7 ML_e and 2.7 ML_e after subtraction) are shown. SiC band extends from 1000 cm^{-1} to 2000 cm^{-1}. Changes after subtraction can be traced by following the dashed lines. D, G and 2D bands are identified at 1360 cm^{-1}, 1590 cm^{-1} and 2720 cm^{-1} respectively for the 2.7 ML_e sample after the subtraction. Relatively small intensity of the 2D peak for the 1.8 ML_e sample is observed.

processes. The peak locations of the *D*, *G* and *2D* bands are indicated by green, red and blue dashed lines respectively (see Fig. 6.3).

The 2.7 ML_e sample has approximately 65% layer 2 coverage. Although layer 2 has a significant coverage on the sample there are fluctuations in the domain size and layer distribution, the intensity of the *2D* peak cannot be used as a tool for thickness measurement [68]. However, the Raman spectra will be dominated by contribution from layer 2. The presence of *D* peak is an indication of disorder in the system. Measurements done by Cancado *et al* [39] suggest an emperical relation between domain size, laser energy and relative intensity of the *D* and the *G* peak given by:

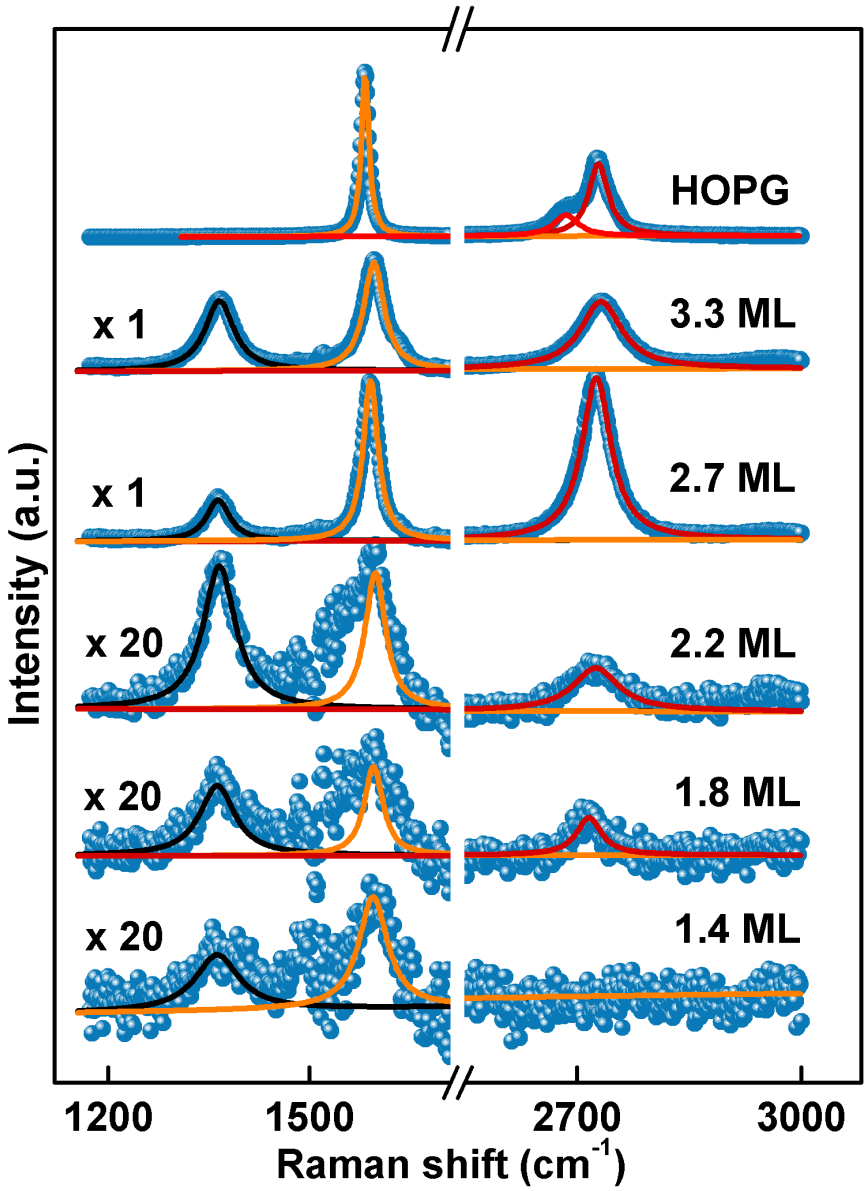

Figure 6.4: Raman spectra are shown for 1.4 ML_e, 1.8 ML_e, 2.2 ML_e, 2.7 ML_e, 3.3 ML_e and HOPG samples with 2.41 nm Argon laser. SiC background spectrum is subtracted from the raw data. The EG Raman data for all samples has been normalized to the most intense SiC Raman feature. 1.4 ML_e sample shows no evidence of 2d peak. A sharp rise in intensity is observed for the 2D peak in 2.7 ML_e sample. 2D peak in Raman spectra for HOPG is clearly different from the single lorentzian observed in EG.

$$L_a(nm) = (2.4 \times 10^{-10})\lambda_{laser}\left(\frac{I_D}{I_G}\right) \tag{6.2}$$

where, I_D and I_G are integrated intensities, L_a is the lower bound limit of the domain size, and

λ_{laser} is the wavelength of the incident laser beam (514.5 *nm*). For the 2.7 ML_e sample lower bound limit of the domain size is estimated to be 32 *nm* and is consistent with the STM measurements.

Raman spectra were acquired on five different thickness samples(1.4, 1.8, 2.2, 2.7, and 3.3 ML_e)in addition to a spectrum on HOPG (see Fig. 6.4). In the spetrum for 1.4 ML_e sample, there is some evidence of the D and G peaks but no intensity for the 2D peak after background subtraction. It should be noted that 1.4 ML_e sample has only layer 0 and layer 1 coverage. For 1.8 and 2.2 ML_e samples, there is a fractional coverage of layer 2 and some intensity is observed from the *2D* mode. A dramatic jump in intensity is observed for the thick 2.7 ML_e sample (Fig. 6.4). At such thickness there is a significant increase in the coverage of layer 2. The observation of single Lorentzian for the *2D* peak for thicker samples (2.7 and 3.3 ML_e) suggests similarities between these EG samples and single layer exfoliated graphene. This is claim is supported by an observation of a Berry's phase of π [55] in the transport measurements on similar thickness samples.

Suppression of the *2D* mode in layer 1 graphene is a striking results that suggests strong interaction between the interface and the terminating graphene layers. STM images 5.1 unique topography of layer 1 graphene, which is dominated by position dependent variations in the local density of states due to the subsurface reconstructions. As discussed previously in Sec. 5.1.2, step height between layer 1 and layer 0 is 2.4 A° from STM measurements which is in close agreement with recent x-ray reflectivity measurements [92].

6.4.1 Peak Shift and Line Width

The peak position in the Raman spectra is due to shift in the energy of inelastically scattered photon. This shift depends on the vibrational modes or the phonon modes. Several factors such as doping and compressive strain [65, 122, 162, 192] to a larger extent contribute to shift in the position of the peaks.

It was observed that peaks are usually shifted into higher energy compared to exfoliated ones. The G and 2D band shifts relative to the exfoliated sample and HOPG are shown in Fig. 6.5. For undoped graphene the average position of G band is expected at 1580 cm^{-1}, for turbostratic graphite there is an upshift of 20 cm^{-1} [123]. In our samples there is an upshift for the G peak of 8 cm^{-1} which seems to be only weakly dependent on thickness, and is likely due to a combination of doping

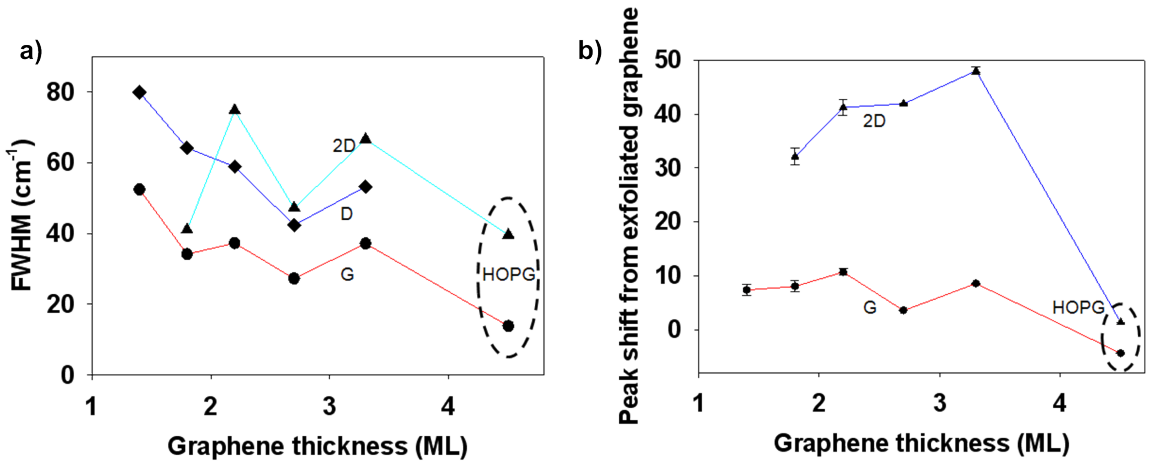

Figure 6.5: (a) Plot of FWHM of the D, G and 2D peak for 1.4, 1.8, 2.2, 2.7, and 3.3 ML_e samples. (b) Peak shift deviation for G and 2D peak from Raman spectra of a single layer exfoliated graphene on SiO_2.

and disorder effects. Intrinsic doping levels of 10^{12} cm^{-2} are achieved due charge transfer from the SiC substrate to the graphene layers (work-function difference). In doped systems there is change in the Fermi surface and this moves the Kohn anomaly [112]. Since the Fermi surface does not follow the Dirac cone displacement, this also leads to stiffening of the G mode phonons. Work done by Pisana *et al* [187] suggest G peak stiffening for both hole- and electron- doping. Electrochemical gating was employed by Das *et al* [53] to reach higher doping levels (up to 5×10^{13} cm^{-2}). In these measurements, phonon stiffening was observed for the G peak, whereas the 2D peak shows phonon softening (20 cm-1) for higher gate voltage. As shown in Fig. 6.5, there is a considerable shift to higher frequency (50 cm^{-1}) for the 2D band and this shift seems to be maximum near 2.7ML_e. The shift does not indicate phonon softening, rather it has been associated with compressive strain [65].

The Raman peak widths also change as a function of film thickness, as shown in Fig. 6.5. Using D or 2D peak energy width Γ as a measure of the mean excitation lifetime $\tau = \hbar/\Gamma$ produces estimates of the hot-carrier transport path length that are close to the measured domain sizes. The mean transport length can be estimated as $v_F\tau/2$ assuming ballistic transport up to the lifetime limiting event, or as $\sqrt{D\tau}$ for diffusive transport (elastic scattering time τ_e much less than τ), where $D = v_F^2\tau_e/2$ is the carrier diffusion constant. Taking $\tau_e = 10$ fs [196] and a peak width of 50 cm^{-1} gives transport lengths of 50 nm (ballistic limit) and 25 nm (diffusive limit), which are comparable to measurements of the domain size from the D/G intensity ratio (see Eq. 6.2), from surface x-ray

scattering [91], and as shown below, from STM. Consequently, for films under 2 graphene ML_e, the excitation lifetime appears to be limited by domain size and defects. For thicker films, the peak width is thought to include a contribution also from multilayer peak splitting plus strain [122].

In exfoliated graphene, after taking trigonal warping into account, only the dispersion along ΓMK are considered. Where, Γ, M and K are the points of high symmetry. Only the phonons having $q >$ K contribute significantly towards the double resonance process. Kurti *et al* [114] suggest that due to trigonal warping, $q <$ K involves an even portion of phase space and $q \sim$ K does not contribute at all to this process because of zero electron-phonon coupling [140, 188]. It is possible that for layer 1 the bands warp in a manner that there is no significant contribution towards the double resonance process at all. This discussion assumes a uniform coverage and a well-ordered film. However, as discussed below, the surface and buffer layer have complicated geometric structures with a relatively high density of SiC steps and domains of different graphene thickness.

STM survey scans on the samples prepared for Raman measurements indicate differences in the thickness and domain size of graphene. Domain sizes appear to depend sensitively on experimental conditions; a direct relation was observed between the domain size and the intensity of the *D* peak for two samples prepared under nominally identical conditions (samples having smaller domains had a larger D peak). None of the samples had significant coverage of layer 3.

6.5 Conclusions

In this chapter, I showed systematic changes in the Raman spectra as the film thickness increases from 1 to 3 layers. The most striking result is a large increase in the intensity of the Raman 2D (G') band for samples with a mean thickness of more than 2.5 graphene-equivalent layers. Correlating this information with STM images, I showed that the first graphene layer imaged by STM produces no 2D peak, but the second imaged layer shows a single-lorentzian 2D peak near 2750 cm-1, similar to spectra acquired from single-layer mechanically exfoliated graphene on SiO_2. The 4-10 cm^{-1} higher frequency shift of the G peak relative to exfoliated samples can be associated with charge exchange with the underlying SiC substrate and the formation of finite size domains of graphene. The much greater (32-50 cm-1) blue shift observed for the 2D-band for thicknesses >1.8 layers may

be correlated with Raman scattering involving these domains and structural strain.

CHAPTER VII

METAL ISLANDS ON EPITAXIAL GRAPHENE

In Chapter. 1 some of the distinct properties of graphene were briefly discussed. The extraordinary linear dispersion relation due to sublattice symmetry makes it a truly unique electronic system. Recently, both fundamental(references needed) and complicated devices (references) have been successfully fabricated on graphene. In principle, it is possible to realize semiconducting/metallic (zigzag/armchair) behavior in graphene and one can envision a circuit with seamless graphene interconnects. In other words, a complete circuit can be realized on a single graphene sheet by using advanced lithographic techniques. However, in a real world situation, metal/graphene contact is unavoidable. The unique electronic structure of graphene will result in a graphene/metal interface unlike traditional metal/semiconductor contacts with different characteristics to address[Here discuss about nanotubes/metal contact experiments]Graphene has a unique electronic structure localized around the K points of its Brillouin zone (see Sec. 1.2.2), and most of the metals exhibit a 3D electronic structure. Furthermore, carrier density in metals is much greater than graphene. Figure 7.1(a) illustrates the poor wavefunction matching at the metal/graphene interface of a metal having a Fermi wavevector less than that of graphene, such as the noble metals Cu, Ag and Au. This results in a low transmission probability leading to high impedance. The workfunction difference of metals and graphene results in screening charge at the interface due to equilibration of Fermi levels. Size related quantum effects can be observed in this accumulated charge at the interface. In the past, similar experiments using contact based STM measurements has been done on HOPG [170]. In these studies, confinement of the screening charge has been suggested at the interface due to a big impedance mismatch between the screening region and the area around it.

Metamaterials or negative indexed materials (NIMs), have generated a lot of interest in the scientific community in the past few years leading to a flurry of experimental [44, 79, 124, 130] and theoretical studies [72, 131, 179–184, 213, 222]. The concept of a NIM was first proposed by Victor Veselago [212] in 1967. Recently, the concept has been applied to graphene in which negative

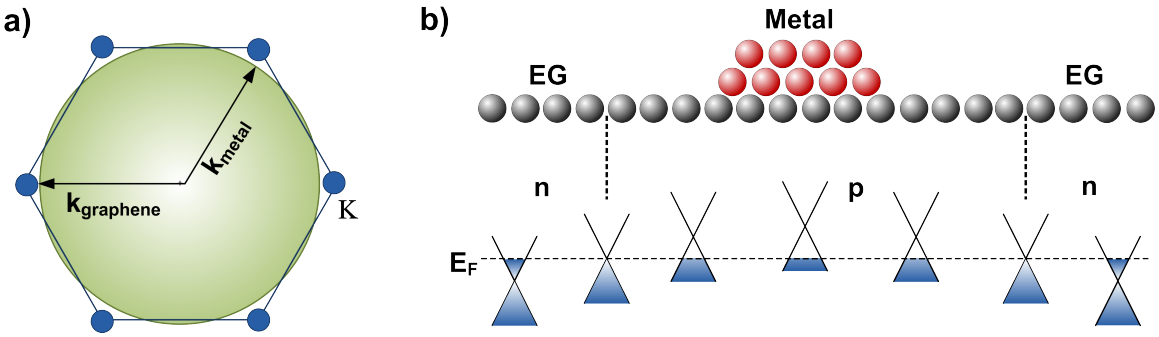

Figure 7.1: (a) An illustration of poor wavefunction matching at metal/graphene interface of noble metals (Cu, Ag and Au) having a Fermi wavevector less than that of graphene. (b) An illustration showing the change in doping induced by a metal island having a workfunction greater than that of graphene. Graphene is hole-doped under the metal island and electron-doped away from it. The doping changes as a function of distance.

refraction of electron waves has been envisioned [43]. For experimental realization, however, one needs to create an abrupt pn junction (a major requirement). It is know, that the sign of the carriers can be changed by applying gate voltage [166, 167] to graphene. A *pn* junction can be generated by gating graphene with a "split gate" such that we have both hole and electron flavors. An abrupt junction can then be realized by fine tuning the gate voltages, to make electron and hole densities on either side of the junction equal.

7.1 Experiment

Metals can be deposited on graphene by using standard lithographic techniques. Such techniques however leave behind residual resist, rendering the samples dirty that are unsuitable for STM measurements. STM techniques require the samples to be clean and electrically conducting. To overcome this, the samples for metal deposition in our experiments were prepared following the procedure outlined in Sec. 3.1. The metal epitaxial graphene (Metal/EG) system is realized by depositing nickel *in situ*, with a metal deposition setup mounted on the room temperature UHV system. As discussed, prior to graphitization, samples were H2 etched in an external home built RF furnace. The samples were then mounted on a molybdenum sample holder with tantalum tabs, and transferred to the room temperature UHV chamber. Graphitization was done by exposing the back of the samples to the electron flux generated by the e-beam heater. The temperature and the background

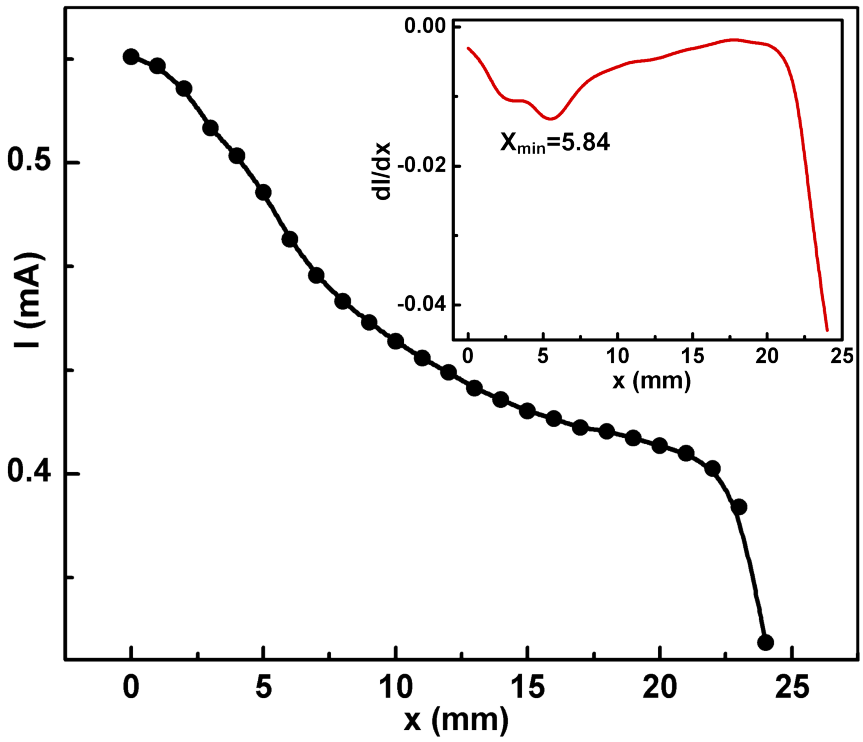

Figure 7.2: Calibration of Ni evaporator is done by locating the minimum in derivative of emission current dI/dx as a function of distance x. This position corresponds to the end of the rod in the plane of the filament. Plot of emission current (I) as a function of Ni source displacement. Inset shows a plot of dI/dx as a function of distance. A minimum in the curve occurs when the end of the Ni source is in the plane of the filament.

pressure during graphitization, were monitored via optical pyrometer and ion pump current respectively. The complete procedure, including various reconstruction phases during the graphitization process, is described in detail in Sec. 3.1. Thicker samples which had a substantial coverage of layer 2 were prepared for metal/EG experiments.

The metal deposition was done via electron beam Ni evaporator, which was developed and constructed by Dr. Cullen [51], a former student. This setup consisted of a 2" long 2 *mm* diameter rod of high purity Ni, mounted on a linear motion feedthrough (Please refer to Dr. Cullen's Ph.D. thesis [51] for details) . The source rod is aligned with the axis of a circular tungsten filament (0.175 *mm*). During operation, a high voltage (2 *kV*) is applied to the Ni rod, and a current of 2.2-2.8 *A* is passed through the filament, held at ground potential. The rod gets heated by electron bombardment from the filament. During operation, the end of the rod is positioned 10 *cm* from the plane of the circular filament. This ensures focusing of the electron beam from the filament,

on to the tip of the rod. The generated flux consists of Ni atoms (and ions[1]) that are collimated by a cylindrical enclosure, having an aperture opening at the end. The beam of Ni atoms exiting the aperture, is projected on the sample (the distance between the sample and the aperture opening is ~15 *cm*). Both the flux rate and the deposition time, can be varied for depositing the desired amount of material. The linear feedthrough allows a travel of 25 *mm* to compensate for the wire loss. It is essential to maintain the geometry of the setup for proper focusing of the electron beam on the tip of the rod. In our experiments, the method proposed by Jones *et al* [101] was used to compensate for the rod loss. In this method, emission current *I(x)* is recorded at x=0, when the rod is fully extended through the plane of the filament. Hereafter, the *I(x)* is recorded at 1.0 *mm* increments of x. Figure 7.2 shows the plot of *I(x)* vs x. Spline fit differentiation of the I(x) curve with respect to x, results in a minimum (see inset in Fig. 7.2), at the point where the tip of the rod is close to the plane of the filament. This location identifies the position of the rod with respect to the the filament.

Prior to deposition, the e-beam evaporator is outgassed and calibrated with a quartz crystal monitor. The quartz crystal microbalance is mounted on the sample manipulator in the RT system, with the crystal pointing in the same direction as the sample heater. For calibration, the flux is evaporated onto the quartz crystal microbalance, and the signal is read via Inficon XTM/2 deposition monitor [1] through an external coaxial BNC connection. Both the deposition rate and the thickness of the film, is monitored using the Inficon monitor. The Inficon monitor can be programmed with parameters for different materials. A fresh quartz crystal microbalance has a natural resonance frequency of 6 MHz which decreases as material gets deposited on the sample. In our experiments, the deposition rates were kept around 0.05 ML_e/s.

7.2 Growth

HOPG has routinely been used for metal deposition, to create nanostructures and other features [8, 49, 94]. The basal plane of HOPG offers a variety of low energy sites including step edges, terrace edges and edge defects making it an ideal template for material deposition. During graphene growth on SiC(0001) substantial amount of substrate roughening takes place. This results in a nonuniform

[1]These ions can be collected to generate ion current.There exists a linear relationship between the ion current and the flux of atoms passing through the aperture. The flux can be monitored by measuring the ion current.

topography with smaller domains, pits, defects and high density of SiC steps as discussed in Chapter. 3. However the Si-face offers a big advantage in terms of intrinsically n-doped graphene films. The doping is due to charge transfer from the surface of the SiC interface, with the doping levels reaching 10^{12} /cm^2. The electron doping in EG has been experimentally verified with variety of different techniques [55, 120, 228]. Now, metal islands will either hole dope or electron dope graphene depending on the workfunction difference between them. Effects of metal (Potassium) doping on EG were recently observed in ARPES measurements [171]. As mentioned previously, the screening charge exists in the metal/EG system as the Fermi levels have to align. This screening charge is envisioned to exist as a 2D "puddle" at the metal/EG interface.

Let us now calculate approximately the doping levels that can be achieved in a Ni/EG system. The workfunction difference between Ni (5.2 eV) and graphene (4.6 eV) is $\Delta\Phi$ ($\Phi_{Ni} - \Phi_{graphene}$) = 0.6 eV. The surface charge density (σ) at the interface with a simple electrostatic model can be given by:

$$\sigma = \frac{\epsilon_0 \Delta\Phi}{ed} \tag{7.1}$$

Where ϵ_0 (=8.85 $\times$ 10^{12} m^{3}kg$^{-1}s^4$A^2) is the permivitty of free space, e (=1.6 $\times$ 10^{-19} C) is the charge of an electron and d (=3.3 Å approx.) is the distance between the metal island and graphene layer. This gives us doping levels of $\sim 10^{13}$ /cm^2, enough to hole dope graphene. The screening charge is given by $\sigma.\pi x^2$ where x is the radius of the screening area. Nickel in principle will give us the desired hole doping with acceptable doping levels.

Ideally a single metal island on a large terrace is a perfect system for scanning STM measurements. One such low energy site for nucleating an island on a terrace is an in-plane atomic scale defect. After deposition the diffusting species can anchor on a defect leading to the formation of an island. Some other low energy sites available for nucleation are step edges, steps and pits. These sites were also found populated with Ni islands and clusters. However, in general, it is difficult to anchor foreign material on graphene as they diffuse rapidly on the surface.

Figure 7.3 shows an 1800 Å $\times$ 1800 Å image of Ni metal islands on EG/SiC(0001). The sample thickness was found to be 2.7 ML$_e$ from AES. The sample is covered with 0.5 ML$_e$ of Ni which was deposited by exposing the sample to a 0.05 ML$_e$/s flux of Ni atoms for 10 s following the procedure

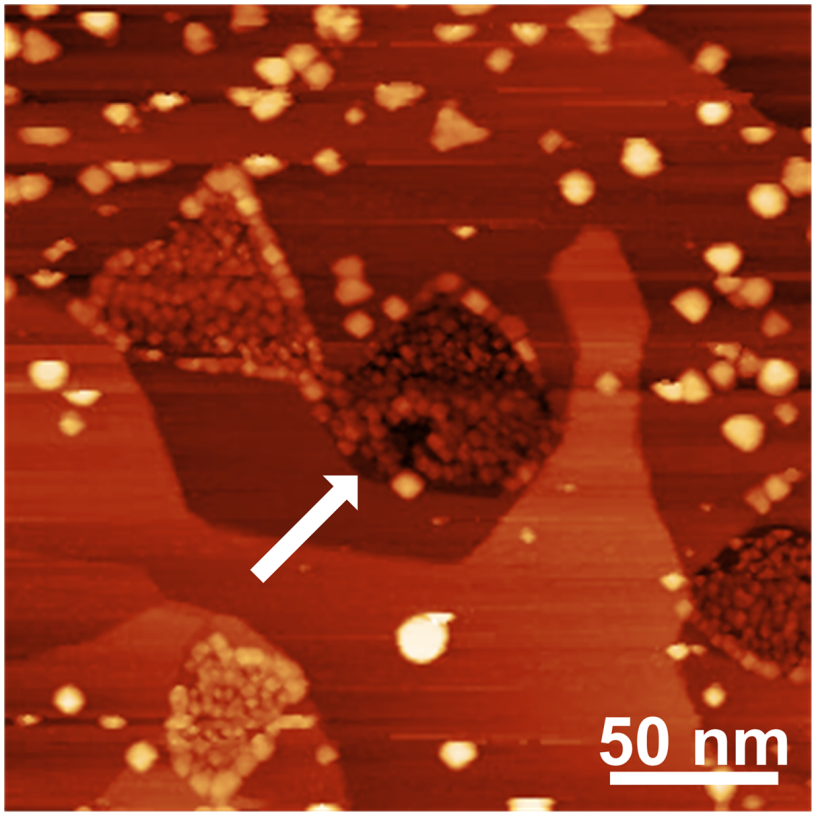

Figure 7.3: STM image (1800 Å × 1800 Å) showing distribution of Ni islands on 2.5 ML_e EG/SiC(0001) (1.0 V, 100 pA). The sample thickness is 2.7 ML_e and the total Ni deposited was ~0.5 ML_e. Ni islands of various shapes and sizes are seen abundant on the sample. A relatively high density of smaller Ni islands are seen in pits (white arrow). "Necklace" formation of islands are seen bordering the pits.

described in Sec. 7.1. Although it was not the focus of this work, a high coverage was useful to study the distribution of these islands on the rough EG/SiC(0001) topography. It is also useful in identification of the low energy sites for island nucleation. The sample was observed to be covered with Ni islands of several different shapes and sizes. The shape of these islands was found to fall under the three categories namely triangular, trapezoidal and circular. These shapes are illustrated in Fig. 7.4(d) and the three island types triangular, trapezoidal and circular are represented by blue, red and green color, respectively. Although the islands were found at all possible low energy sites, the pits were found to be most densely populated. In the past, nucleation sites have been created on HOPG by oxygen etching [178]. This is done by heating HOPG to ~650 °C in a controlled O_2 environment which produces 700 Å wide and monolayer-deep (3.35 Å) pits. These pits were found to be effective nucleation sites for anchoring metals [141]. However, an essential difference here is

that the pits in EG run several layers deep. Nonetheless, as seen in Fig. 7.3 the pit (white arrow) is observed to be "necklaced" with Ni islands similar to the metal nanostructures seen around pits on etched HOPG [141]. Also evident in this image is the relatively high population of metal islands in the pit. Interestingly, the islands in the pit were found to considerably smaller than the islands found at other locations. A possible explanation for this is that due to small terraces in EG the diffusing species get trapped in the pits before they can combine with other similarly diffusing species for bigger island formation. Furthermore, only circular islands were found in the pits. The terraces and steps were found to contain bigger islands of all shapes.

Figure 7.4(a) shows a smaller image (900 Å $\times$ 900 Å) from a different location on the same sample. In this image one can observe trapezoidal and triangular shaped islands on the terrace and an accumulation of circular islands in the pit. There are a few smaller clusters that appear as tiny specks in the image. Figure 7.4(c) shows a line profile across a triangular shaped island. The height and the width of this island is 12 Å and 150 Å respectively. Similarly shaped electron beam deposited Ni islands have been observed on other surfaces. Ni deposition on Au(111) results in metal islands anchored at the elbows of the herringbone ($22 \times \sqrt{3}$) reconstruction [41, 51]. It should be remembered that gold surface is extremely flat and provides an ideal template for material deposition. These islands were suggested to be highly ordered. In Fig. 7.4(b) one can observe the absence of islands (white arrows) that were imaged in the previous scan. The images (a) and (b) were acquired consecutively, one after the other. This is also evident in Fig. 7.3 where some atoms the islands are partially imaged before disappearing. These atoms move under the influence of STM tip. These islands are not securely anchored on the terraces and are highly mobile. Manipulation of atoms and clusters with STM is an extensively researched area [203–205, 220].

The relative population of different islands was calculated by counting them individually in eight 3000 Å $\times$ 3000 Å sized scans at different locations on the sample. For this particular sample (2.7 ML_e) and 0.5 ML_e Ni deposition, 75% of the sample was found to be covered with circular islands as compared to 15% and 10% in case of triangular and trapezoidal shaped islands, respectively. It seems likely that the island distribution is a function of sample quality (terrace size, defects and pits) and amount of deposited Ni. The relative population of these islands is represented by the pie-chart in Fig. 7.4(d), along with the illustration of their shapes.

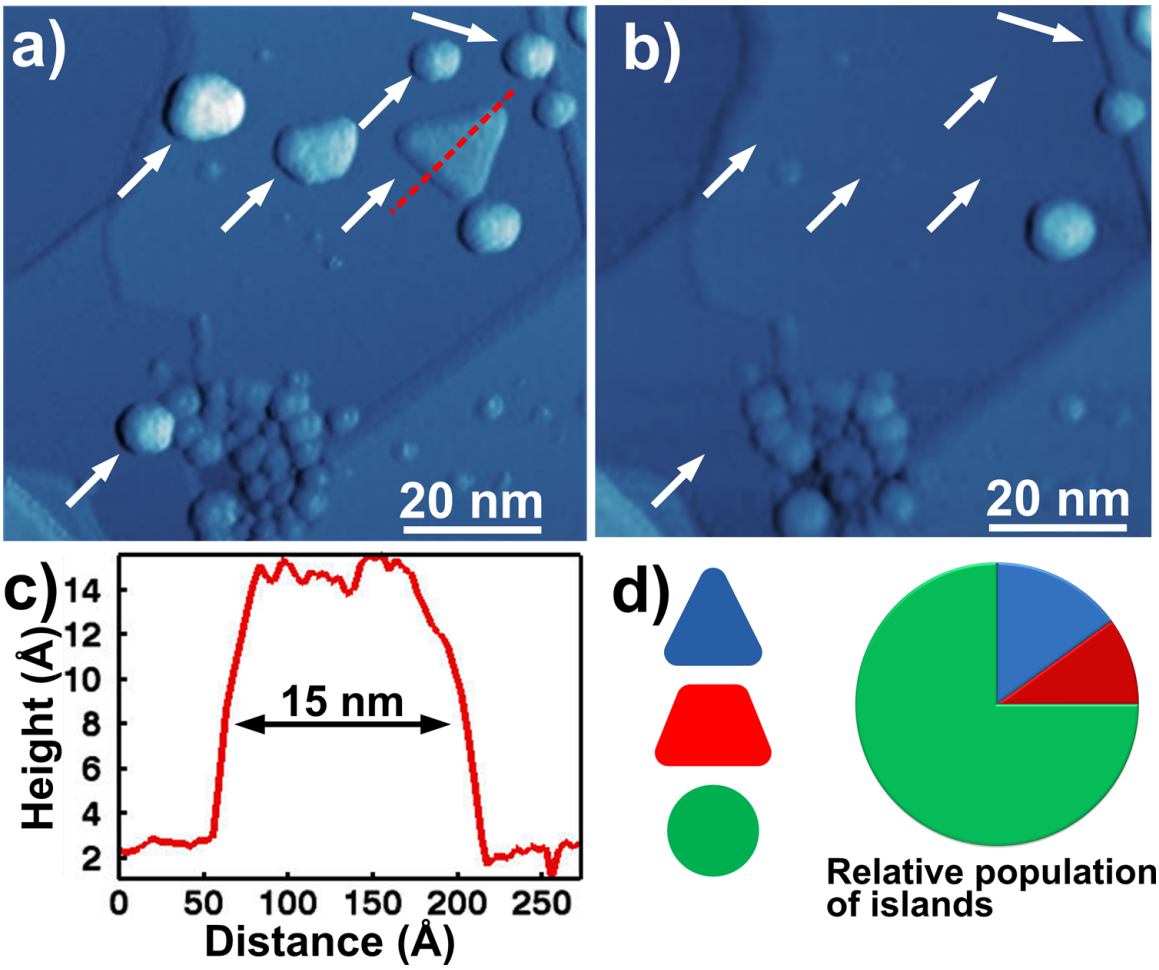

Figure 7.4: STM imaging of different types of Ni island on EG/SiC(0001). (a) 900 Å × 900 Å image shows circular islands in the pit and bigger islands on the terrace and the step (2 V, 100 pA). White arrows point to the location of the island that were not imaged in the subsequent scan, as shown in (b)(2 V, 100 pA). (c) Line profile across triangular island shows that it is 12 Å high and 150 Å wide. (d) Relative population of triangular (blue), trapezoidal (red) and circular (green) is 15%, 10% and 75%, respectively.

The screening charge region of an island is expected to be bigger than its size. A high coverage of Ni, 0.5 ML_e in our case, may not be suitable for studying doping related effects as it may uniformly dope the sample. This may happen if the population density of these islands is high so that the screening regions of these individual islands overlap. In order to overcome such a potential problem only a fractional amount of Ni should be deposited so that individual islands are well separated form each other. We also saw the difficulty in anchoring Ni islands on graphene and even a massive 12 Å high 150 Å wide island can get displaced under an STM tip.

7.3 Spectroscopy of Nickel Clusters

As discussed previously, Ni islands can potentially hole dope EG. The screening charge region is believed to exist at the interface of the metal/EG contact in the form of a 2D "puddle". It is possible that due to small size of the island quantization of this screening charge may take place under the metal island. It is also of interest, to find out whether wavevector matching at the graphene/Ni interface would play any role in such small islands. Figure 7.1(b) illustrates the doping effect of a metal island on graphene, where the metal workfunction is assumed to be greater than graphene workfunction (4.6 eV). Under such conditions graphene could be hole doped under the metal island. If we move away from the island, the hole doping decreases, and we make a transition into the region with intrinsic *n* doping. The transition region is of interest, as not only there is a change in the nature of doping, the electronic structure of EG may also evolve. If this transition region is abrupt then negative refraction of electron waves can be observed. Such changes in the doping and electronic structure as a function of distance can be measured with scanning tunneling spectroscopy (STS) technique. Similar measurements techniques have been employed in the past to study the tunneling of GaAS(110) with Fe clusters [69]. In these measurements size dependent and distance dependent changes in the tunneling were observed. Similar measurements have also been done on Au nanocrystals on Au(111) [88] and HOPG [29] surface.

In the previous section, we saw the difficulty in anchoring Ni islands on graphene and even a massive 12 Å high 150 Å wide island can get displaced under an STM tip. The sample was also found covered with metal clusters, although their population density was found to be significantly lower than that of metals. They were found to be less mobile than the islands. STS studies over these clusters would gives us similar doping effects but at a more local scale.

Figure 7.5(a) shows a high resolution image (180 Å $\times$ 180 Å) of a metal cluster on EG. The sample thickness is 3 ML_e and the Ni coverage is 0.15 ML. The cluster size is approximately 10 Å $\times$ 20 Å. It is difficult to predict the structure of the metal cluster by STM alone. A scattering pattern can be observed in the vicinity of the Ni cluster. This pattern is similar to the scattering observed around defects and step edges. Figure 7.5(b) shows a magnified rendered image of the Ni cluster (red box). This image was subsequently taken after an *IV* spectral grid in the previous image. The

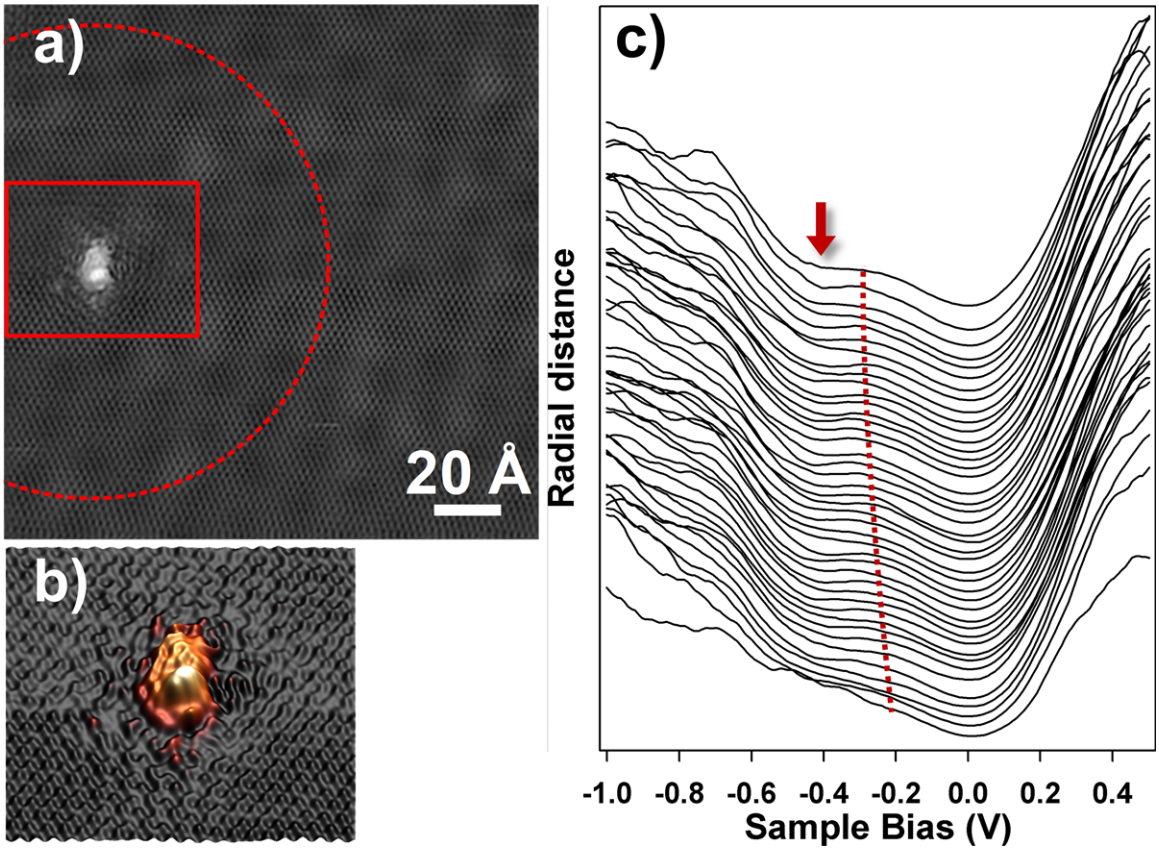

Figure 7.5: Spectroscopy studies of a Ni cluster as a function of distance. (a) 180 Å × 180 Å high resolution image of a Ni cluster on EG (0.5 V, 100 pA). A scattering pattern is also seen around the cluster. (b) Magnified rendered image of the metal cluster in (a) (red box). An *IV* spectra is taken at every eighth point (8 × 8 grid) in the image. *dI/dV* spectra is produced by doing a numerical derivative of the *IV* spectra. (c) Radially averaged spectra (red circle in (a)) as a function of distance from the center of the Ni cluster (see text). The spectra are vertically displaced for clarity. Arrow points to the approximate location of the Dirac point for EG/SiC(0001) samples. A shift is observed in the hump (red line) and the shoulder on the left, with distance.

spectra were only teken at every eighth point (8 × 8 grid) in the image due to the thermal drift at 300 K. The conductance (*dI/dV* spectra were generated by doing a numerical derivative of the *IV* spectra. In these measurements, we are looking for changes as a function of distance. Starting from the center of the cluster, all the spectra lying within a radius of 10 Å were selected and averaged together. This radial averaging process was continued for 42 different radii. These different radii were offset by 3.2 Å, the first radius was 10 Å, the second was 13.2 Å and so on. This process is also illustrated in Fig. 7.5(a) by the red circle. This radial averaging process was done by using FORTRAN based interactive data language (IDL) [2] software package. Figure 7.5(c) shows 42

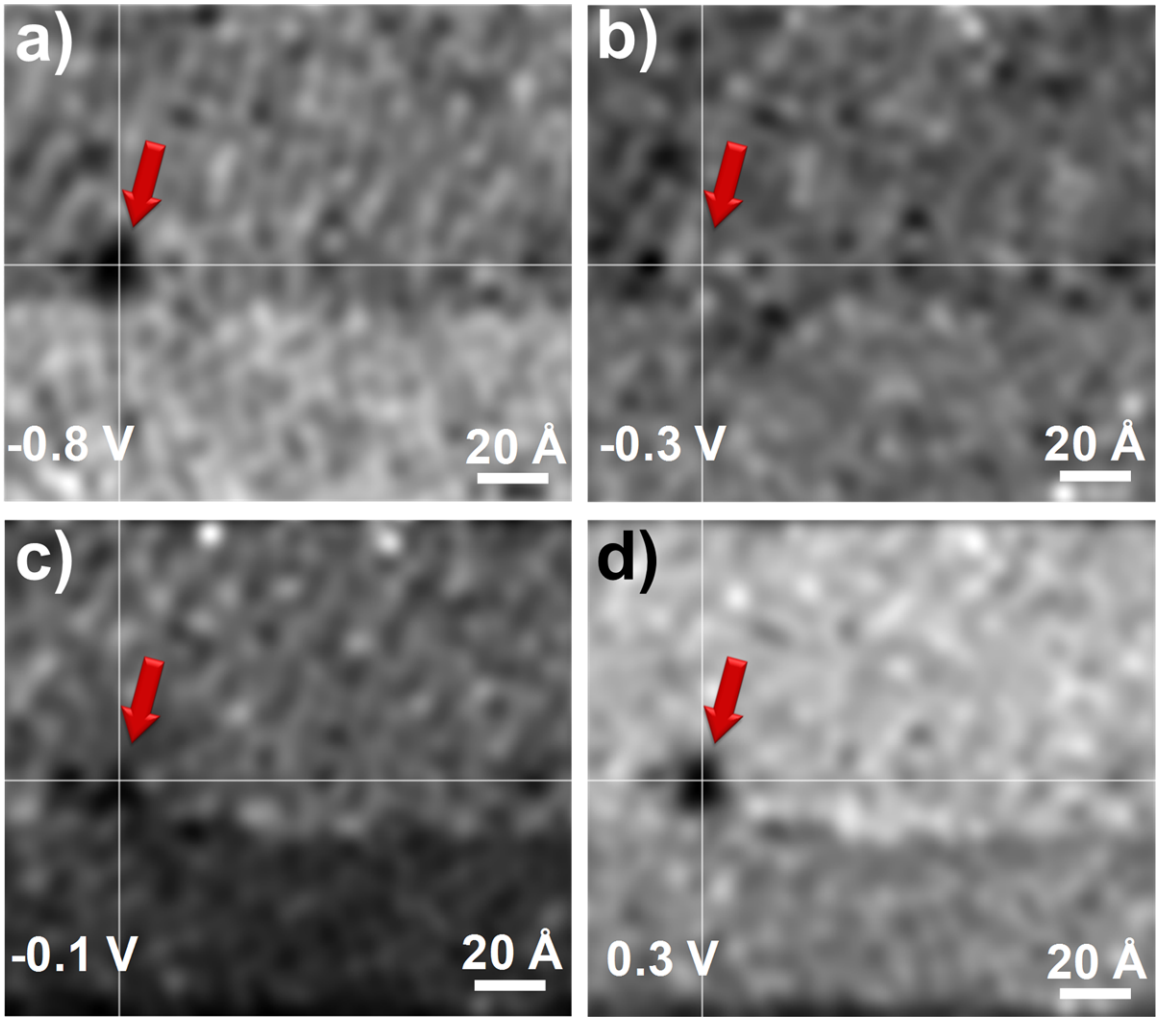

Figure 7.6: Conductance (dI/dV) map of the topographic image in Fig. 7.5(a) with Ni cluster (see Figures for energy values (V)). The red arrows point to the location of the Ni cluster in the topographic image. Horizontal and vertical lines are drawn for better clarity. At energies away from the Dirac point (~-0.3 eV relative to the Fermi level), the DOS is suppressed at the location of the Ni cluster. (b) Near the *Dirac* point, however, such suppression is not observed due to infinitely long wavelengths. Change in contrast between top and the bottom half of the image could be due different reconstruction domains.

radially averaged spectra offset by a distance of 3.2Å from each other. The spectra are also vertically displaced for clarity. The bottom most and top most spectra correspond to a distance of 10 Å and 138 Å, respectively, from the center of the cluster. A red arrow approximately points to the location of the Dirac point on the spectra far away (138 Å) from the cluster. Please refer to Sec. 5.1.3 for discussion about the minimum in the DOS at near -0.3 V. A shift is observed in the "hump-like" feature centered around -0.3 V, with distance. From top to the bottom spectra this feature shifts

towards higher energy. The red dashed line traces the shift in the position this feature. A similar trend is also evident for the shoulder centered around -0.7 V. It is difficult to predict a similar shift for the minimum (possibly the *Dirac* point). It is difficult to localize charge from an impurity on graphene, which could be reason for not seeing a pronounced shift in the position of the minimum. The room temperature STS (RTSTS) measurements put a limit on the energy resolution of the data. In general, the broadening is given by:

$$\Delta E = 3.3 k_B T \tag{7.2}$$

where, k_B is the boltzman constant and ΔE is the broadening due to temperature and experiment. At room temperature ΔE=0.085 eV. It is possible that the minimum feature is getting masked by the hump. The upshift in the energy location of the "hump-like" feature agrees with the hole doping expected around the metal island. There is an energy shift of ~0.1 eV over a distance of 128 Å for this feature.

Figure 7.6 shows an extrapolated *dI/dV* map of the spectral grid. Although, there is a significant amount of thermal broadening in STS at room temperature, some interesting results are seen in the (dI/dV) maps. In all figures, the red arrow points to the location of the cluster in the topography. At energies away from the *Dirac* point (Fig. 7.6 (a),(c) and (d)), a suppression in the DOS is observed at the location of the metal cluster. Whereas near the *Dirac* point such a suppression is not observed. At the Dirac point, the electrons wavelength is infinitely long and it becomes difficult to scatter them. They become insensitive to local perturbation in the potential. A change in the contrast between the upper half and the lower half of the image can be observed in Fig. 7.6(b). This might due to a change in the SiC reconstruction domain along the scan direction.

These results indicate some changes in the local electronic structure by the Ni cluster. Similar studies on bigger island would help us understand analogous problems in lithography. The confinement of the 2D screening charge at the metal/EG contact is an open question. Future work may also include STS studies of the hole to electron transition region. An abrupt transition region could give rise to negative refraction of electron waves.

7.4 Conclusions

In this chapter, I investigated the electronic properties growth of Ni islands on EG/SiC(0001). At a higher coverage of Ni (0.5 ML), I found the sample to be covered with islands of three different shapes, namely: circular, triangular and trapezoidal. I suggested that the relative population density of these different shaped islands, depends both on the quality of EG, and the amount of deposited Ni. I identified step edges, pits and in-plane atomic scale defects as low energy sites for island nucleation. Pits by far were found to be the most populated with only smaller islands. I suggested the possibility that these smaller islands get trapped in the pits, before they can combine with other such similar species for bigger island formation.

I showed STS studies of metal clusters as a function of distance. I also showed doping dependent shift in the energy position of the dominant features in the radially averaged spectra. A suppression in the DOS was shown at -0.3 V with respect to the Fermi level. This minimum is believed to be the location of Dirac point [120, 226]. I showed extrapolated *dI/dV* maps at room temperature taken on the same cluster. The maps showed a suppression in the DOS at the cluster location for energies away from the *Dirac*-point energy. *dI/dV* map at the Dirac point energy, showed no suppression in the DOS. Near the Dirac point, wavelength of the electrons is infinitely long and they become insensitive to local perturbation.

CHAPTER VIII

CONCLUSIONS

Electronic properties of graphene have been investigated in a variety of experiments. Results of these studies highlight the potential of this material system as a replacement for the aging Si technology. However, for better integration into the present technological trends, epitaxial solutions are required. In this thesis work, I studied growth and electronic structure of epitaxial graphene (EG) on SiC(0001). The samples were grown both in ultra-high vacuum and low vacuum furnace environments. I used different surface science tools, namely: scanning tunneling microscopy (STM)/spectroscopy (STS), Auger electron spectroscopy (AES), low energy electron difraction (LEED) and Raman spectroscopy to study this new 2D electronic material system.

The graphene growth on SiC(0001) in UHV is epitaxial. I found that the topography is dominated by smaller domains, pits and a high density of defects. This is due to substantial amount of substrate roughening during the growth. I found some evidence on the low coverage samples which may indicate that the growth starts at random locations on the step edges. The growth must include mechanisms by which Si can desorb from the samples. On low coverage samples, I found patches of layer 0 (interface) on a layer 1 (first graphene layer) terrace that can act as potential venting sites for Si. This suggests a growth mechanism where individual graphene sheets come together at elevated temperatures. Graphene islands were found to be less common on the EG samples. I have shown that the electronic properties of the islands is dominated by SiC substrate. These graphene islands were found to prefer armchair over zigzag step edge configuration. I also found that a high background pressure during UHV growth adversely effects the quality of the samples. Future work may include more detailed investigation of growth process on low coverage samples with STM, and correlating these observations with theoretical simulations.

I also carried out STM investigations of low-vacuum furnace grown EG samples on SiC(0001). I found that the topography was dominated by SiC steps and bigger graphene terraces (compared to UHV grown samples). Atomic force microscopy (AFM) showed raised solid ”tiger-stripe” features

emanating from the bottom of the steps and running perpendicular to the step edges. With high resolution STM imaging, I found the "tiger stripe" features to be filled with amorphous carbon-based species. Other higher nanocaps were discovered around the tiger stripes and on the terrace. I made an attempt to regraphitize the furnace grown samples in UHV. I found that on heating the samples to 1280 °C, the tiger stripes were found to be free of amorphous carbon species and parts of nanocaps had a flatter topography of height 3.5 Å. I was able to get rid of the nanocaps at 1320 °C. The average terrace size of these samples was found to be ~300 nm. It is evident that the low-vacuum furnace environment plays an important role in the growth process. Furthermore, the role of the amorphous species is also not understood. Clearly a good deal of work remains before a complete understanding of the growth process is established.

I was able to study the unique electronic and structural properties of EG on SiC(0001). I found evidence of an interface region (layer 0) in agreement with previous studies. I was not able to image graphene in the interface region. I was able to study unique properties of the first graphene layer (layer 1). At higher energies, layer 1 became transparent and interface states were imaged. At low bias, a honeycomb graphene lattice was seen. The second graphene layer (layer 2) was found to show asymmetry in the charge distribution of the neighboring atoms. A model based on the STM height difference of the A and the B atoms at different biases, showed the location of the Dirac point as -65 mV (relative to the Fermi level). This discrepancy indicates a need for a more complex model for interaction between the first two graphene layers. Future work may involve analysis of other parameters (decay constant) that may vary with bias voltage. I also found that scattering of electron waves from a defect gives rise to unique patterns ($\sqrt{3}\times\sqrt{3}$)R30°). I found graphene to be continuous over step edges except between layer 0/1, and any subsurface deformities.

Raman spectroscopy has been a powerful tool for identification of different thickness exfoliated graphene samples. A single layer graphene shows a single lorentzian peak for the 2D mode, which evolves for other thicknesses. I was able to extract similar layer dependent information for EG/SiC(0001) samples. I found an anomalous suppression of the 2D peak in layer 1, whereas layer 2 showed a single lorentzian. I suggested a strong interaction between layer 0 and layer 1. Interestingly I found a step of 2.4 Å (<graphite step of 3.35 Å) from layer 0 to 1 with STM measurements.

For device application, it is important to characterize the metal/EG contacts. For small contacts,

quantization effects are expected in the screening charge that exists at the interface. Ni metal islands can locally hole dope EG, which regains its electron doping in regions away from the metal island. I found three different shaped islands distributed on EG. The pits were found to be highly populated relative to the rest of the sample. Spectroscopy measurements on the Ni metal cluster showed shift in energy of some spectral features as a function of distance. I was not able to establish a similar trend in the energy position of the Dirac point. In *dI/dV* maps I found the inability of the metal cluster to scatter electrons near Dirac point energy due to infinitely long wavelengths. A lot of work remains to be done to have a complete understanding of the system. It may be interesting to investigate the change in the electronic structure of EG near the transition region. An abrupt pn junction (transition region) could exhibit negative refraction. Future work may include STM/STS studies of size related quantum effects on the screening charge.

Bibliography

[1] *Inficon, XTM/2 Thin Film Deposition Monitor*.

[2] *Interactive Data Language (IDL), Research Systems, Inc.*

[3] *Princeton Research Instruments, Reverse View LEED Optics RVL 8-120*.

[4] *SPI Supplies, HOPG grade SPI-1*.

[5] *Veeco; di CP-II atomic force microscope.*

[6] Cree Inc., www.cree.com, 2004.

[7] Abergel, D. S. L., Russell, A., and Fal'ko, V. I. Visibility of Graphene Flakes on a Dielectric Substrate. *Applied Physics Letters 91*, 6 (Aug 6 2007).

[8] Ahn, Y., and Seidl, M. Defect-Induced Nucleation of Sputter-Deposited Gold on Graphite. *Journal of Applied Physics 77*, 11 (Jun1 1995), 5558–5562.

[9] AIZAWA, T., SOUDA, R., OTANI, S., ISHIZAWA, Y., and OSHIMA, C. ANOMALOUS BOND OF MONOLAYER GRAPHITE ON TRANSITION-METAL CARBIDE SURFACES. *PHYSICAL REVIEW LETTERS 64*, 7 (FEB 12 1990), 768–771.

[10] AIZAWA, T., SOUDA, R., OTANI, S., ISHIZAWA, Y., and OSHIMA, C. BOND SOFTENING IN MONOLAYER GRAPHITE FORMED ON TRANSITION-METAL CARBIDE SURFACES. *PHYSICAL REVIEW B 42*, 18 (DEC 15 1990), 11469–11478.

[11] Ando, T. Theory of electronic states and transport in carbon nanotubes. *Journal Of The Physical Society Of Japan 74*, 3 (Mar. 2005), 777–817.

[12] Ando, T., Nakanishi, T., and Saito, R. Berry's Phase and Absence of Back Scattering in Carbon Nanotubes. *Journal of Physics Society, Japan. 67*, 8 (1998), 2857–2862.

[13] Angot, T., Portail, M., Forbeaux, I., and Layet, J. M. Graphitization of the 6H-SiC(0001) Surface Studied by HREELS. *Surface Science 502* (Apr 2002), 81–85.

[14] Atamny, F., and Baiker, A. Investigation of Carbon-Based Catalysts by Scanning Tunneling Microscopy: Opportunities and Limitations. *Applied Catalysis A: General 173*, 2 (Oct 1998), 201–230.

[15] Atamny, F., Spillecke, O., and Schlogl, R. On the STM Imaging Contrast of Graphite: Towards a "True" Atomic Resolution. *Phys. Chem. Chem. Phys. 1*, 17 (Sep 1999), 4113–4118.

[16] Auger, P. The Effect of a Photoelectric Compound. *Journal De Physique Et Le Radium 6* (1925).

[17] Avouris, Ph. Molecular electronics with carbon nanotubes. *Acc. Chem. Res. 35*, 12 (Dec. 2002), 1026–1034.

[18] Bai, C. *Scanning Tunneling Microscopy and Its Application*. Springer, 1995.

[19] Bang, H., Ito, Y., Kawamura, Y., Hosoda, E., Yoshida, C., Maruyama, T., Naritsuka, S., and Kusunoki, M. Observation of Nanosized Cap Structures on 6H-SiC $(000\bar{1})$ Substrates by Ultrahigh-vacuum Scanning Tunneling Microscopy. *Japanese Journal of Applied Physics Part 1-Regular Papers Brief Communications & Review Papers 45*, 1A (Jan 2006), 372–374.

[20] Baranov, A., Bekhterev, A., Bobovich, Y., and Petrov, V. Interpretation of some Singularities in Raman-Spectra of Graphite and Glass Carbon. *Optika I Spektroskopiya 62*, 5 (May 1987), 1036–1042.

[21] Bardeen, J. Tunnelling from a Many-Particle Point of View. *Physical Review Letters 6*, 2 (1961).

[22] Becker, A., Till, J., and McCulloch, E. Cytological Demonstration 0f Clonal Nature of Spleen Colonies Derived from Transplanted Mouse Marrow Cells. *Nature 197*, 486 (1963).

[23] Becker, R., Golovchenko, J., Hamann, D., and Swartzentruber, B. Real-space Observation of Surface-states on Si(111)7x7 with the Tunneling Microscope. *Physical Review Letters 55*, 19 (1985), 2032–2034.

[24] Bednorz, J., and Mullar, K. Possible High-TC Superconductivity in the BA-LA-CU-O System. *Zeitschrift Fur Physik B-condensed Matter 64*, 2 (1986), 189–193.

[25] Berger, C., Song, Z., Li, X., Wu, X., Brown, N., Naud, C., Mayou, D., Li, T., Hass, J., Marchenkov, A. N., Conrad, E. H., First, P. N., and de Heer, W. A. Electronic confinement and coherence in patterned epitaxial graphene. *Science 312*, 5777 (May 2006), 1191–1196.

[26] Bernhardt, J., Schardt, J., Starke, U., and Heinz, K. Epitaxially ideal oxide-semiconductor interfaces: Silicate adlayers on hexagonal (0001) and (000(1)over-bar) sic surfaces. *Applied Physics Letters 74*, 8 (Feb. 1999), 1084–1086.

[27] Bernhardt, J., Schardt, J., Starke, U., and Heinz, K. Silicate monolayers on the hexagonal surfaces of 4h-and 6h-sic. *Silicon Carbide and Related Materials 1999 PTS, 1 & 2 338-3* (2000), 383–386.

[28] BERRY, M. QUANTAL PHASE-FACTORS ACCOMPANYING ADIABATIC CHANGES. *PROCEEDINGS OF THE ROYAL SOCIETY OF LONDON SERIES A-MATHEMATICAL PHYSICAL AND ENGINEERING SCIENCES 392*, 1802 (1984), 45–57.

[29] Bigioni, T. P., Harrell, L. E., Cullen, W. G., Guthrie, D. E., Whetten, R. L., and First, P. N. Imaging and tunneling spectroscopy of gold nanocrystals and nanocrystal arrays. *European Physical Journal D 6*, 3 (June 1999), 355–364.

[30] Binnig, G., and Rohrer, H. Scanning tunneling microscopy. *Helvetica Physica Acta 55*, 6 (1982), 726–735.

[31] Binnig, G., Rohrer, H., Gerber, C., and Weibel, E. 7x7 reconstruction on si(111) resolved in real space. *Physical Review Letters 50*, 2 (1983), 120–123.

[32] Binnig, G., Rohrer, H. H., Gerber, C., and Weibel, E. Tunneling through a controllable vacuum gap. *Applied Physics Letters 40*, 2 (1982), 178–180.

[33] Bostwick, A., Ohta, T., Seyller, T., Horn, K., and Rotenberg, E. Quasiparticle dynamics in graphene. *Nat Phys 3*, 1 (Jan. 2007), 36–40.

[34] Brar, V. W., Zhang, Y., Yayon, Y., Ohta, T., McChesney, J. L., Bostwick, A., Rotenberg, E., Horn, K., and Crommie, M. F. Scanning tunneling spectroscopy of inhomogeneous electronic structure in monolayer and bilayer graphene on sic. *Applied Physics Letters 91*, 12 (2007), 122102.

[35] Brihuega, I., Mallet, P., Bena, C., Bose, S., Michaelis, C., Vitali, L., Varchon, F., Magaud, L., Kern, K., and Veuillen, J. Y. Quasiparticle Chirality in Epitaxial Graphene Probed at the Nanometer Scale. *Physical Review Letters 101*, 20 (NOV 14 2008).

[36] Burk, A., and Rowland, L. The role of excess silicon and in situ etching on 4H-SiC and 6H-SiC epitaxial layer morphology. *JOURNAL OF CRYSTAL GROWTH 167*, 3-4 (OCT 1996), 586–595.

[37] Cancado, L., Pimenta, M., Neves, B., Dantas, M., and Jorio, A. Influence of the atomic structure on the raman spectra of graphite edges. *Physical Review Letters 93*, 24 (Dec 10 2004).

[38] Cancado, L., Pimenta, M., Neves, B., Medeiros-Ribeiro, G., Enoki, T., Kobayashi, Y., Takai, K., Fukui, K., Dresselhaus, M., Saito, R., and Jorio, A. Anisotropy of the raman spectra of nanographite ribbons. *Physical Review Letters 93*, 4 (JUL 23 2004).

[39] Cancado, L., Takai, K., Enoki, T., Endo, M., Kim, Y., Mizusaki, H., Jorio, A., Coelho, L., Magalhaes-Paniago, R., and Pimenta, M. General equation for the determination of the crystallite size l-a of nanographite by raman spectroscopy. *APPLIED PHYSICS LETTERS 88*, 16 (APR 17 2006).

[40] Casiraghi, C., Hartschuh, A., Lidorikis, E., Qian, H., Harutyunyan, H., Gokus, T., Novoselov, K. S., and Ferrari, A. C. Rayleigh imaging of graphene and graphene layers. *Nano Letters 7*, 9 (2007), 2711–2717.

[41] Chambliss, D., Wilson, R., and Chiang, S. Nucleation of Ordered Ni Island Arrays on Au(111) by Surface-Lattice Dislocations. *PHYSICAL REVIEW LETTERS 66*, 13 (APR 1 1991), 1721–1724.

[42] Charlier, J.-C., Blase, X., and Roche, S. Electronic and transport properties of nanotubes. *Reviews of Modern Physics 79*, 2 (2007), 677.

[43] Cheianov, V. V., Fal'ko, V., and Altshuler, B. L. The focusing of electron flow and a veselago lens in graphene p-n junctions. *Science 315*, 5816 (Mar. 2007), 1252–1255.

[44] Chen, H., Ran, L., Huangfu, J., Zhang, X., Chen, K., Grzegorczyk, T. M., and Kong, J. A. Negative refraction of a combined double s-shaped metamaterial. *Appl. Phys. Lett. 86*, 15 (2005), 151909–.

[45] Chen, W., Xu, H., Liu, L., Gao, X., Qi, D., Peng, G., Tan, S. C., Feng, Y., Loh, K. P., and Wee, A. T. S. Atomic structure of the 6h-sic(0001) nanomesh. *Surface Science 596*, 1-3 (Dec. 2005), 176–186.

[46] Chen, Z., Appenzeller, J., Lin, Y.-M., Sippel-Oakley, J., Rinzler, A. G., Tang, J., Wind, S. J., Solomon, P. M., and Avouris, Ph. An integrated logic circuit assembled on a single carbon nanotube. *Science 311*, 5768 (Mar. 2006), 1735–.

[47] Chen, Z., Li, J., and Wang, E. In situ scanning tunnelling microscopic study of nickel electrodeposition on hopg. *Journal of Electroanalytical Chemistry 373*, 1-2 (Aug. 1994), 83–87.

[48] Chu, T., and Campbell, R. Chemical etching of silicon carbide with hydrogen. *Journal of the Electrochemical Society 112*, 9 (1965).

[49] Chu, X., and Schmidt, L. Reactions of NO, O2, H2O, and CO2 with the Basal-Plane of Graphite. *SURFACE SCIENCE 268*, 1-3 (MAY 1 1992), 325–332.

[50] Chung, D. Review graphite. *J. Mater. Sci. 37*, 8 (Apr. 2002), 1475–89.

[51] Cullen, W. G. *The Role of Place-Exchange, Dislocations and Substrate Symmetry in Ni/Au(111) Heteroepitaxy.* PhD thesis, School of Physics, Georgia Institute of Technology, 1999.

[52] Cullen, W. G., and First, P. N. Island shapes and intermixing for submonolayer nickel on Au(111). *Surf. Sci. 420*, 1 (Jan. 1999), 53–64.

[53] Das, A., Pisana, S., Chakraborty, B., Piscanec, S., Saha, S. K., Waghmare, U. V., Novoselov, K. S., Krishnamurthy, H. R., Geim, A. K., Ferrari, A. C., and Sood, A. K. Monitoring dopants by Raman scattering in an electrochemically top-gated graphene transistor. *NATURE NANOTECHNOLOGY 3*, 4 (APR 2008), 210–215.

[54] Davisson, C., and Germer, L. Diffraction of electrons by a crystal of nickel. *Physical Review 30*, 6 (DEC 1927), 705–740.

[55] de Heer, W. A., Berger, C., Wu, X., First, P. N., Conrad, E. H., Li, X., Li, T., Sprinkle, M., Hass, J., Sadowski, M. L., Potemski, M., and Martinez, G. Epitaxial graphene. *Solid State Commun. 143* (2007), 92–100.

[56] Deacon, R. S., Chuang, K.-C., Nicholas, R. J., Novoselov, K. S., and Geim, A. K. Cyclotron resonance study of the electron and hole velocity in graphene monolayers. *Physical Review B (Condensed Matter and Materials Physics) 76*, 8 (2007), 081406.

[57] Dombrowski, R., Steinebach, C., Wittneven, C., Morgenstern, M., and Wiesendanger, R. Tip-induced band bending by scanning tunneling spectroscopy of the states of the tip-induced quantum dot on inas(110). *Physical Review B 59*, 12 (Mar 15 1999), 8043–8048.

[58] Dresselhaus, M. Future directions in carbon science. *ANNUAL REVIEW OF MATERIALS SCIENCE 27* (1997), 1–34.

[59] Dresselhaus, M., and Avouris, P. *Carbon Nanotubes: Synthesis, Structure, Properties, and Applications*. Springer, 2001.

[60] DRESSELHAUS, M., DRESSELHAUS, G., and SAITO, R. PHYSICS OF CARBON NANOTUBES. *CARBON 33*, 7 (1995), 883–891.

[61] Dulot, F., Mansour, L., Leycuras, A., Wulfhekel, W., Sander, D., d'Avitaya, F., and Hanbucken, M. Structure and morphology of concave-shaped surfaces on 6H-Si(0001) after H-2 etching. *APPLIED SURFACE SCIENCE 187*, 3-4 (FEB 28 2002), 319–325.

[62] Emtsev, K. V., Bostwick, A., Horn, K., Jobst, J., Kellogg, G. L., Ley, L., McChesney, J. L., Ohta, T., Reshanov, S. A., Rotenberg, E., Schmid, A. K., Waldmann, D., Weber, H. B., and Seyller, T. Atmospheric pressure graphitization of sic(0001)- a route towards wafer-size graphene layers.

[63] Emtsev, K. V., Speck, F., Seyller, T., Ley, L., and Riley, J. D. Interaction, growth, and ordering of epitaxial graphene on SiC{0001} surfaces: A comparative photoelectron spectroscopy study. *PHYSICAL REVIEW B 77*, 15 (APR 2008).

[64] Feenstra, R., and Stroscio, J. Tunneling spectroscopy of the gaas(110) surface. *Journal of Vacuum Science and Technology B 5*, 4 (Jul-Aug 1987), 923–929.

[65] Ferralis, N., Maboudian, R., and Carraro, C. Evidence of structural strain in epitaxial graphene layers on 6h-sic(0001). *Phys. Rev. Lett. 101*, 15 (Oct. 2008), 156801–4.

[66] Ferrari, A., and Robertson, J. Interpretation of raman spectra of disordered and amorphous carbon. *Physical Review B 61*, 20 (May 15 2000), 14095–14107.

[67] Ferrari, A. C. Raman spectroscopy of graphene and graphite: Disorder, electron-phonon coupling, doping and nonadiabatic effects. *Solid State Communications 143*, 1-2 (July 2007), 47–57.

[68] Ferrari, A. C., Meyer, J. C., Scardaci, V., Casiraghi, C., Lazzeri, M., Mauri, F., Piscanec, S., Jiang, D., Novoselov, K. S., Roth, S., and Geim, A. K. Raman spectrum of graphene and graphene layers. *Physical Review Letters 97*, 18 (2006), 187401.

[69] First, P. N., Stroscio, J. A., Dragoset, R. A., Pierce, D. T., and Celotta, R. J. Metallicity and gap states in tunneling to Fe clusters on GaAs(110). *Physical Review Letters 63*, 13 (Sept. 1989), 1416–1419.

[70] Forbeaux, I., Themlin, J. M., Charrier, A., Thibaudau, F., and Debever, J. M. Solid-state graphitization mechanisms of silicon carbide 6h-sic polar faces. *Appl. Surf. Sci. 162* (Aug. 2000), 406–412.

[71] Forbeaux, I., Themlin, J. M., and Debever, J. M. Heteroepitaxial graphite on 6h-sic(0001): Interface formation through conduction-band electronic structure. *Phys. Rev. B 58*, 24 (Dec. 1998), 16396–16406.

[72] Fu, C., Zhang, Z. M., and First, P. N. Brewster angle with a negative-index material. *Appl. Opt. 44*, 18 (June 20 2005), 3716–24.

[73] Fujita, M., Wakabayashi, K., Nakada, K., and Kusakabe, K. Peculiar localized state at zigzag graphite edge. *Journal Of The Physical Society Of Japan 65*, 7 (July 1996), 1920–1923.

[74] Geim, A. K., Booth, T. J., Yang, R., Jiang, D., Novoselov, K. S., Castro Neto, A. H., Blake, P., and Hill, E. W. Making graphene visible. *arxiv:0705.0259v3 [cond-mat.mes-hall]* (2007), 1–3.

[75] Geim, A. K., and MacDonald, A. H. Graphene: Exploring carbon flatland. *Physics Today 60*, 8 (2007), 35–41.

[76] Geim, A. K., and Novoselov, K. S. The rise of graphene. *Nat. Mater. 6*, 3 (Mar. 2007), 183–191.

[77] Greiner, W., and Bromley, D. A. *Relativistic Quantum Mechanics*. Springer, 2000.

[78] Griffiths, D. J. *Introduction to Quantum Mechanics*. Pearson Prentice Hall, 2006.

[79] Grigorenko, A. N., Geim, A. K., Gleeson, H. F., Zhang, Y., Firsov, A. A., Khrushchev, I. Y., and Petrovic, J. Nanofabricated media with negative permeability at visible frequencies. *Nature 438*, 7066 (Nov. 2005), 335–338.

[80] Guinea, F., Neto, A. H. C., and Peres, N. M. R. Electronic states and landau levels in graphene stacks. *Phys. Rev. B 73*, 24 (2006), 245426.

[81] Guinea, F., Neto, A. H. C., and Peres, N. M. R. Interaction effects in single layer and multilayer graphene. *European Physical Journal-Special Topics 148* (Sep 2007), 117–125.

[82] Guisinger, N. P., Rutter, G. M., Crain, J. N., Heiliger, C., First, P. N., and Stroscio, J. A. The atomic-scale investigation of graphene formation on 6H-SiC(0001). *J. Vac. Sci. Technol. A* (2007). in press.

[83] Gulbrans, E., Andrew, K., and Brassart, F. Oxidation of silicon carbide at 1150 degrees to 1400 degrees c and at 9 x 10-8 to 5 x 10-1 torr oxygen pressure. *Journal of the Electrochemical Society 113*, 12 (1966), 1311–&.

[84] Gupta, A., Chen, G., Joshi, P., Tadigadapa, S., and Eklund, P. C. Raman scattering from high-frequency phonons in supported n-graphene layer films. *Nano Letters 6*, 12 (Dec 13 2006), 2667–2673.

[85] Hallin, C., Bakin, A., Owman, F., Martensson, P., Kordina, O., and Janzen, E. Study of the hydrogen etching of silicon carbide substrates. In *Silicon Carbide and Related Materials*, Nakashima, S and Matsunami, H and Yoshida, S and Harima, H, Ed., vol. 142 of *Institute of Physics Conference Series*. IOP Publishing Ltd., Techno house, Redcliffe Way, Bristol, England BS1 6NX, 1996, pp. 613–616.

[86] Hallin, C., Owman, F., Martensson, P., Ellison, A., Konstantinov, A., Kordina, O., and Janzen, E. In situ substrate preparation for high-quality sic chemical vapour deposition. *J. Cryst. Growth 181*, 3 (Nov. 1997), 241–253.

[87] Hannon, J. B., and Tromp, R. M. Pit formation during graphene synthesis on SiC(0001): In situ electron microscopy. *PHYSICAL REVIEW B 77*, 24 (JUN 2008).

[88] Harrell, L. E., Bigioni, T. P., Cullen, W. G., Whetten, R. L., and First, P. N. Scanning tunneling microscopy of passivated Au nanocrystals immobilized on Au(111) surface. *J. Vac. Sci. Technol. B 17*, 6 (Nov. 1999), 2411–2416.

[89] Harris, C., and Afanasev, V. Sio2 as an insulator for sic devices. *MIcroelectronic Engineering 36*, 1-4 (JUN 1997), 167–174.

[90] Hass, J., de Heer, W. A., and Conrad, E. H. The growth and morphology of epitaxial multilayer graphene. *Journal of Physics-Condensed Matter 20*, 32 (Aug 13 2008).

[91] Hass, J., Feng, R., Li, T., Li, X., Song, Z., de Heer, W. A., First, P. N., Conrad, E. H., Jeffrey, C. A., and Berger, C. Highly ordered graphene for two dimensional electronics. *Appl. Phys. Lett. 89*, 14 (2006), 143106.

[92] Hass, J., Millan-Otoya, J. E., First, P. N., and Conrad, E. H. Interface structure of epitaxial graphene grown on 4h-sic(0001). *Physical Review B 78*, 20 (NOV 2008).

[93] Hass, J., Varchon, F., Millan-Otoya, J. E., Sprinkle, M., Sharma, N., De Heer, W. A., Berger, C., First, P. N., Magaud, L., and Conrad, E. H. Why multilayer graphene on 4H-SiC(000$\bar{1}$) behaves like a single sheet of graphene. *Physical Review Letters 100*, 12 (Mar. 2008), 125504.

[94] Hennig, G. Determination of Lattice Vacanicies in Graphite. *JOURNAL OF CHEMICAL PHYSICS 40*, 10 (1964), 2877–&.

[95] Henriksen, E. A., Jiang, Z., Tung, L.-C., Schwartz, M. E., Takita, M., Wang, Y.-J., Kim, P., and Stormer, H. L. Cyclotron resonance in bilayer graphene. *Physical Review Letters 100*, 8 (2008), 087403.

[96] Hibino, H., Kageshima, H., Maeda, F., Nagase, M., Kobayashi, Y., and Yamaguchi, H. Microscopic thickness determination of thin graphite films formed on sic from quantized oscillation in reflectivity of low-energy electrons. *Physical Review B (Condensed Matter and Materials Physics) 77*, 7 (2008), 075413.

[97] Ishigami, M., Chen, J., Cullen, W., Fuhrer, M., and Williams, E. Atomic structure of graphene on sio2. *Nano Letters 7*, 6 (2007), 1643–1648.

[98] Itoh, H., Ichinose, T., Oshima, C., Ichinokawa, T., and Aizawa, T. Scanning tunneling microscopy of monolayer graphite epitaxially grown on a tic(111) surface. *Surf. Sci. 254*, 1-3 (Aug. 1991), L437–L442.

[99] Jiang, Z., Henriksen, E. A., Tung, L. C., Wang, Y.-J., Schwartz, M. E., Han, M. Y., Kim, P., and Stormer, H. L. Infrared spectroscopy of landau levels of graphene. *Physical Review Letters 98*, 19 (2007), 197403.

[100] Johansson, L. I., Owman, F., and Martensson, P. High-resolution core-level study of 6h-sic(0001). *Phys. Rev. B 53*, 20 (1996), 13793–13802.

[101] Jones, T., Sawler, J., and Venus, D. Simple, Calibrated Deposition Monitor Iincorporated into angle Electron-Beam Evaporator. *Review of Scientific Instruments 64*, 7 (Jul 1993), 2008–2012.

[102] Kaplan, R. Surface structure and composition of [beta]- and 6h-sic. *Surf. Sci. 215*, 1-2 (May 1989), 111–134.

[103] Katsnelson, M. I. Scattering of charge carriers by point defects in bilayer graphene. *Physical Review B (Condensed Matter and Materials Physics) 76*, 7 (2007), 073411.

[104] Katsnelson, M. I., Novoselov, K. S., and Geim, A. K. Chiral tunnelling and the klein paradox in graphene. *Nature Physics 2* (Sep 1 2006), 620 – 625.

[105] Kechedzhi, K., Fal'ko, V. I., McCann, E., and Altshuler, B. L. Influence of trigonal warping on interference effects in bilayer graphene. *Phys. Rev. Lett. 98*, 17 (2007), 176806.

[106] Kelly, B. T. *The Physics of Graphite*. Springer, 1981.

[107] Klein, O. Die reflexion von elektronen an einem potentialsprung nach der relativischen dynamik von dirac. *Z. Phys 53* (1929), 157–165.

[108] Knight, D., and White, W. Characterization of diamond films by raman-spectroscopy. *Journal of Materials Research 4*, 2 (Mar-Apr 1989), 385–393.

[109] Kobayashi, Y., ichi Fukui, K., Enoki, T., Kusakabe, K., , and Kaburagi, Y. Observation of zigzag and armchair edges of graphite using scanning tunneling microscopy and spectroscopy. *arXiv:cond-mat/0503472 v2 29 Mar 2005* (2005).

[110] Kobayashi, Y., Kusakabe, K., Fukui, K.-i., and Enoki, T. Stm/sts observation of peculiar electronic states at graphite edges. *Physica E: Low-dimensional Systems and Nanostructures 34*, 1-2 (Aug. 2006), 678–681.

[111] Kobayashi, Y., Takai, K., ichi Fukui, K., Enoki, T., Harigaya, K., Kaburagi, Y., and Hishiyama, Y. Stm observation of electronic wave interference effect in finite-sized graphite with dislocation-network structures. *Phys. Rev. B 69*, 3 (2004), 035418–7.

[112] Kohn, W. Image of the fermi surface in the vibration spectrum of a metal. *Physical Review Letters 2*, 9 (1959), 393–394.

[113] Kubby, J., Wang, Y., and Greene, W. Fabry-perot transmission resonances in tunneling microscopy. *Physical Review B 43*, 11 (Apr 15 1991), 9346–9349.

[114] Kurti, J., Zolyomi, V., Gruneis, A., and Kuzmany, H. Double resonant Raman phenomena enhanced by van Hove singularities in single-wall carbon nanotubes. *Physical Review B 65*, 16 (Apr 15 2002).

[115] Kusunoki, M., Rokkaku, M., and Suzuki, T. Epitaxial carbon nanotube film self-organized by sublimation decomposition of silicon carbide. *APPLIED PHYSICS LETTERS 71*, 18 (NOV 3 1997), 2620–2622.

[116] Kusunoki, M., Suzuki, T., Hirayama, T., Shibata, N., and Kaneko, K. A formation mechanism of carbon nanotube films on sic(0001). *Appl. Phys. Lett. 77*, 4 (July 2000), 531–533.

[117] Kusunoki, M., Suzuki, T., Kaneko, K., and Ito, M. Formation of self-aligned carbon nanotube films by surface decomposition of silicon carbide. *PHILOSOPHICAL MAGAZINE LETTERS 79*, 4 (APR 1999), 153–161.

[118] Landau, L. D., and Lifshitz, E. M. *Statistical Physics*. Pergamon Press Inc., London, 1958.

[119] Latil, S., Meunier, V., and Henrard, L. Massless fermions in multilayer graphitic systems with misoriented layers: Ab initio calculations and experimental fingerprints. *Physical Review B (Condensed Matter and Materials Physics) 76*, 20 (2007), 201402.

[120] Lauffer, P., Emtsev, K. V., Graupner, R., Seyller, T., Ley, L., Reshanov, S. A., and Weber, H. B. Atomic and electronic structure of few-layer graphene on sic(0001) studied with scanning tunneling microscopy and spectroscopy. *Physical Review B (Condensed Matter and Materials Physics) 77*, 15 (2008), 155426.

[121] Lee, C., Wei, X., Kysar, J. W., and Hone, J. Measurement of the elastic properties and intrinsic strength of monolayer graphene. *Science 321*, 5887 (2008), 385–388.

[122] Lee, D. S., Riedl, C., Krauss, B., von Klitzing, K., Starke, U., and Smet, J. H. Raman spectra of epitaxial graphene on sic and of epitaxial graphene transferred to sio2. *Nano Letters 8*, 12 (Dec 2008), 4320–4325.

[123] Lespade, P., Marchand, A., Couzi, M., and Cruege, F. Characterization of Carbon Materials with Raman Microspectrometry. *Carbon 22*, 4-5 (1984), 375–385.

[124] Lezec, H. J., Dionne, J. A., and Atwater, H. A. Negative refraction at visible frequencies. *Science 316*, 5823 (Apr. 2007), 430–432.

[125] Li, L., Hasegawa, Y., and Sakurai, T. Si-and c-rich structure of the 6h-sic(0001) surface. *Journal Of Vacuum Science & Technology B 15*, 4 (July 1997), 1307–1309.

[126] Li, L., and Tsong, I. S. T. Surface structure and morphology induced by ultrathin ti films on 6h-sic(0001) and (000(1)over-bar). *Surf. Sci. 364*, 1 (Aug. 1996), 54–60.

[127] Li, T. *Characteristics of Graphite Films on Silicon- and Carbon- Terminated Faces of Silicon Carbide*. PhD thesis, School of Physics, Georgia Institute of Technology, 2006.

[128] Li, X. *Epitaxial Graphene Films on SiC: Growth, Characterization, and Devices*. PhD thesis, School of Physics, Georgia Institute of Technology, 2008.

[129] Lopes dos Santos, J. M. B., Peres, N. M. R., and Castro Neto, A. H. Graphene bilayer with a twist: electronic structure. *arXiv:0704.2128v1* (2007).

[130] Lu, Z., Chen, C., Schuetz, C. A., Shi, S., Murakowski, J. A., Schneider, G. J., and Prather, D. W. Subwavelength imaging by a flat cylindrical lens using optimized negative refraction. *Appl. Phys. Lett. 87*, 9 (2005), 091907–.

[131] Luo, C., Johnson, S. G., Joannopoulos, J. D., and Pendry, J. B. All-angle negative refraction without negative effective index. *Phys. Rev. B 65*, 20 (2002), 201104–4.

[132] Ma, Y. Simulation of interstitial diffusion in graphite. *PHYSICAL REVIEW B 76*, 7 (AUG 2007).

[133] Mallet, P., Varchon, F., Naud, C., Magaud, L., Berger, C., and Veuillen, J.-Y. Electron states of mono- and bilayer graphene on sic probed by scanning-tunneling microscopy. *Physical Review B (Condensed Matter and Materials Physics) 76*, 4 (2007), 041403.

[134] Marchini, S., Guenther, S., and Wintterlin, J. Scanning tunneling microscopy of graphene on Ru(0001). *PHYSICAL REVIEW B 76*, 7 (AUG 2007).

[135] Martensson, P., Owman, F., and Johansson, L. I. Morphology, atomic and electronic structure of 6h-sic(0001) surfaces. *PHYSICA STATUS SOLIDI B-BASIC RESEARCH 202*, 1 (1997), 501–528.

[136] Martin, J., Akerman, N., Ulbricht, G., Lohmann, T., Smet, J. H., von Klitzing, K., and Yacoby, A. Observation of electron-hole puddles in graphene using a scanning single-electron transistor. *Nature Physics advanced online publication* (Nov 2007).

[137] Maruyama, T., Bang, H. J., Kawamura, Y., Fujita, N., Tanioku, K., Shiraiwa, T., Hozumi, Y., Naritsuka, S., and Kusunoki, M. Scanning-tunneling-microscopy of the formation of carbon nanocaps on sic(000-1). *Chem. Phys. Lett. 423*, 4-6 (June 2006), 317–320.

[138] Matsui, T., Kambara, H., Niimi, Y., Tagami, K., Tsukada, M., and Fukuyama, H. Sts observations of landau levels at graphite surfaces. *Phys. Rev. Lett. 94*, 22 (2005), 226403–4.

[139] Mattausch, A., and Pankratov, O. Ab initio study of graphene on sic. *Physical Review Letters 99*, 7 (2007), 076802.

[140] Maultzsch, J., Reich, S., and Thomsen, C. Double-resonant raman scattering in graphite: Interference effects, selection rules, and phonon dispersion. *Physical Review B (Condensed Matter and Materials Physics) 70*, 15 (2004), 155403.

[141] McBride, J., Van Tassell, B., Jachmann, R., and Beebe, T. Molecule corrals as templates for the formation of metal and silicon nanostructures. *JOURNAL OF PHYSICAL CHEMISTRY B 105*, 18 (MAY 10 2001), 3972–3980.

[142] McCann, E. Asymmetry gap in the electronic band structure of bilayer graphene. *Phys. Rev. B 74*, 16 (2006), 161403.

[143] McCann, E., and Fal'ko, V. I. Landau-level degeneracy and quantum hall effect in a graphite bilayer. *Phys. Rev. Lett. 96*, 8 (2006), 086805.

[144] McCann, E., Kechedzhi, K., Fal'ko, V. I., Suzuura, H., Ando, T., and Altshuler, B. L. Weak-localization magnetoresistance and valley symmetry in graphene. *Phys. Rev. Lett. 97*, 14 (2006), 146805.

[145] McEuen, P. Single-wall carbon nanotubes. *Physics World 13*, 6 (June 2000), 31–6.

[146] McEuen, P. L., Bockrath, M., Cobden, D. H., Yoon, Y. G., and Louie, S. G. Disorder, pseudospins, and backscattering in carbon nanotubes. *Phys. Rev. Lett. 83*, 24 (Dec. 1999), 5098–5101.

[147] Melmed, A. J. The art and science and other aspects of making sharp tips. *Journal of Vacuum Science & Technology B 9*, 2 (1991), 601–608.

[148] Mermin, N. Crystalline order in 2 dimensions. *Physical Review 176*, 1 (1968).

[149] Meyer, J. C., Geim, A. K., Katsnelson, M. I., Novoselov, K. S., Booth, T. J., and Roth, S. The structure of suspended graphene sheets. *Nature 446*, 7131 (Mar. 2007), 60–63.

[150] Meyer, J. C., Geim, A. K., Katsnelson, M. I., Novoselov, K. S., Obergfell, D., Roth, S., Girit, C., and Zettl, A. On the roughness of single- and bi-layer graphene membranes. *Solid State Communications 143*, 1-2 (Jul 2007), 101–109.

[151] Mizes, H. A., and Foster, J. S. Long-range electronic perturbations caused by defects using scanning tunneling microscopy. *Science 244*, 4904 (May 1989), 559–562.

[152] Mohr, M., Maultzsch, J., Dobardzic, E., Reich, S., Milosevic, I., Damnjanovic, M., Bosak, A., Krisch, M., and Thomsen, C. Phonon dispersion of graphite by inelastic x-ray scattering. *Physical Review B (Condensed Matter and Materials Physics) 76*, 3 (2007), 035439.

[153] Moore, G. E. Cramming More Components Onto Integrated Circuits. *Electronics 38*, 8 (Apr 19 1965).

[154] Morozov, S. V., Novoselov, K. S., Katsnelson, M. I., Schedin, F., Elias, D. C., Jaszczak, J. A., and Geim, A. K. Giant intrinsic carrier mobilities in graphene and its bilayer. *Physical Review Letters 100*, 1 (2008), 016602.

[155] Morozov, S. V., Novoselov, K. S., Katsnelson, M. I., Schedin, F., Ponomarenko, L. A., Jiang, D., and Geim, A. K. Strong suppression of weak localization in graphene. *Phys. Rev. Lett. 97* (2006), 016801.

[156] NAGASHIMA, A., NUKA, K., ITOH, H., ICHINOKAWA, T., OSHIMA, C., and OTANI, S. Electronic states of monolayer graphite formed on tic(111) surface. *SURFACE SCIENCE 291*, 1-2 (July 1993), 93–98.

[157] Nair, R. R., Blake, P., Grigorenko, A. N., Novoselov, K. S., Booth, T. J., Stauber, T., Peres, N. M. R., and Geim, A. K. Fine structure constant defines visual transparency of graphene. *Science 320*, 5881 (June 2008), 1308–.

[158] Nakada, K., Fujita, M., Dresselhaus, G., and Dresselhaus, M. S. Edge state in graphene ribbons: Nanometer size effect and edge shape dependence. *Phys. Rev. B 54*, 24 (Dec. 1996), 17954–17961.

[159] Nakada, K., Fujita, M., Wakabayashi, K., and Kusakabe, K. Localized electronic states on graphite edge. *Czechoslovak Journal Of Physics 46* (1996), 2429–2430.

[160] Nemanich, R., and Solin, S. 1st-Order and 2nd-Order Raman-Scattering from Finite-Size Crystals of Graphite. *Physical Review B. 20*, 2 (1979), 392–401.

[161] Neto, A. H. C., Guinea, F., Peres, N. M. R., Novoselov, K. S., and Geim, A. K. The electronic properties of graphene. *Reviews of Modern Physics 81*, 1 (2009), 109.

[162] Ni, Z. H., Chen, W., Fan, X. F., Kuo, J. L., Yu, T., Wee, A. T. S., and Shen, Z. X. Raman spectroscopy of epitaxial graphene on a sic substrate. *Physical Review B 77*, 11 (Mar. 2008), 115416.

[163] Niimi, Y., Kambara, H., Matsui, T., Yoshioka, D., and Fukuyama, H. Real-space imaging of alternate localization and extension of quasi-two-dimensional electronic states at graphite surfaces in magnetic fields. *Physical Review Letters 97*, 23 (Dec. 2006), 236804.

[164] Niimi, Y., Matsui, T., Kambara, H., Tagami, K., Tsukada, M., and Fukuyama, H. Scanning tunneling microscopy and spectroscopy studies of graphite edges. *Appl. Surf. Sci. 241*, 1-2 (Feb. 2005), 43–48.

[165] Niimi, Y., Matsui, T., Kambara, H., Tagami, K., Tsukada, M., and Fukuyama, H. Scanning tunneling microscopy and spectroscopy of the electronic local density of states of graphite surfaces near monoatomic step edges. *Phys. Rev. B 73*, 8 (2006), 085421.

[166] Novoselov, K. S., Geim, A. K., Morozov, S. V., Jiang, D., Katsnelson, M. I., Grigorieva, I. V., Dubonos, S. V., and Firsov, A. A. Two-dimensional gas of massless dirac fermions in graphene. *Nature 438*, 7065 (Nov. 2005), 197–200.

[167] Novoselov, K. S., Geim, A. K., Morozov, S. V., Jiang, D., Zhang, Y., Dubonos, S. V., Grigorieva, I. V., and Firsov, A. A. Electric field effect in atomically thin carbon films. *Science 306*, 5696 (Oct. 2004), 666–669.

[168] Novoselov, K. S., Jiang, D., Schedin, F., Booth, T. J., Khotkevich, V. V., Morozov, S. V., and Geim, A. K. Two-dimensional atomic crystals. *PNAS 102*, 30 (July 2005), 10451–10453.

[169] Novoselov, K. S., McCann, E., Morozov, S. V., Falko, V. I., Katsnelson, M. I., Geim, A. K., Schedin, F., and Jiang, D. Unconventional quantum hall effect and berry's phase of 2π in bilayer graphene. *Nature Physics 2* (2006), 177–180. 1 Manchester Centre for Mesoscience and Nanotechnology, University of Manchester, Manchester, M13 9PL, UK 2 Department of Physics, Lancaster University, Lancaster, LA1 4YB, UK 3 Institute for Microelectronics Technology, 142432, Chernogolovka, Russia 4 Institute for Molecules and Materials, Radboud University of Nijmegen, Toernooiveld 1, 6525 ED Nijmegen, The Netherlands.

[170] Ogbazghi, A. Y. *Conductance through Nanometer-scale Metal-to-Graphite Contacts*. PhD thesis, School of Physics, Georgia Institute of Technology, 2005.

[171] Ohta, T., Bostwick, A., Seyller, T., Horn, K., and Rotenberg, E. Controlling the electronic structure of bilayer graphene. *Science 313*, 5789 (Aug. 2006), 951–954.

[172] Ohta, T., Gabaly, F. E., Bostwick, A., McChesney, J. L., Emtsev, K. V., Schmid, A. K., Seyller, T., Horn, K., and Rotenberg, E. Morphology of graphene thin film growth on sic(0001). *New Journal of Physics 10*, 2 (2008), 023034 (7pp).

[173] Ong, W. J., and Tok, E. S. Role of si clusters in the phase transformation and formation of (6 x 6)-ring structures on 6h-sic(0001) as a function of temperature: An stm and xps study. *Phys. Rev. B 73*, 4 (Jan. 2006), 045330–14.

[174] Owman, F., Hallin, C., Martensson, P., and Janzen, E. Removal of polishing-induced damage from 6H-SiC(0001) substrates by hydrogen etching. *JOURNAL OF CRYSTAL GROWTH 167*, 1-2 (SEP 1996), 391–395.

[175] Owman, F., Johansson, L. I., and Martensson, P. Surface reconstructions of 6h-sic(0001) studied with scanning tunneling microscopy and core-level photoelectron spectroscopy. *Silicon carbide and related materials 1995 142* (1996), 477–480.

[176] Owman, F., and Martensson, P. The sic(0001)6 root x6 root 3 reconstruction studied with stm and leed. *Surf. Sci. 369*, 1-3 (Dec. 1996), 126–136.

[177] Pan, Y., Shi, D.-X., and Gao, H.-J. Formation of graphene on Ru(0001) surface. *CHINESE PHYSICS 16*, 11 (NOV 2007), 3151–3153.

[178] Patrick, D., Cee, V., and Beebe, T. Molecule Corrals for Studies of Monolayer Organic Films. *SCIENCE 265*, 5169 (Jul8 1994), 231–234.

[179] Pendry, J. Pendry replies:. *Phys. Rev. Lett. 87*, 24 (2001), 249704–1.

[180] Pendry, J. B. Negative refraction makes a perfect lens. *Phys. Rev. Lett. 85*, 18 (2000), 3966–3969.

[181] Pendry, J. B. A chiral route to negative refraction. *Science 306*, 5700 (2004), 1353–1355.

[182] Pendry, J. B. Time reversal and negative refraction. *Science* (Aug. 2008), 1162087–.

[183] Pendry, J. B., Schurig, D., and Smith, D. R. Controlling electromagnetic fields. *Science* (May 2006), 1125907–.

[184] Pendry, J. B., and Smith, D. R. Comment on "wave refraction in negative-index media: Always positive and very inhomogeneous". *Phys. Rev. Lett. 90*, 2 (2003), 029703–1.

[185] Pereira, J. M., Vasilopoulos, P., and Peeters, F. M. Tunable quantum dots in bilayer graphene. *Nano Letters 7*, 4 (Apr. 2007), 946–949.

[186] Pimenta, M. A., Dresselhaus, G., Dresselhaus, M. S., Cancado, L. G., Jorio, A., and Saito, R. Studying disorder in graphite-based systems by raman spectroscopy. *Physical Chemistry Chemical Physics 9*, 11 (2007), 1276–1291.

[187] Pisana, S., Lazzeri, M., Casiraghi, C., Novoselov, K. S., Geim, A. K., Ferrari, A. C., and Mauri, F. Breakdown of the adiabatic born-oppenheimer approximation in graphene. *Nat. Mater. 6*, 3 (Mar. 2007), 198–201.

[188] Piscanec, S., Lazzeri, M., Mauri, F., Ferrari, A., and Robertson, J. Kohn anomalies and electron-phonon interactions in graphite. *Phys. Rev. Lett. 93*, 18 (Oct. 2004), 185503–1.

[189] Quesenberry, P. E. *Scanning Tunneling Microscopy Studies of a Reactive Interface: Ni/GaAs*. PhD thesis, School of Physics, Georgia Institute of Technology, 1996.

[190] Raman, C., and Krishnan, K. A new type of secondary radiation. *Nature 121* (Jan-Jun 1928), 501–502.

[191] Riedl, C., Starke, U., Bernhardt, J., Franke, M., and Heinz, K. Structural properties of the graphene-sic(0001) interface as a key for the preparation of homogeneous large-terrace graphene surfaces. *Physical Review B 76*, 24 (Dec. 2007), 245406.

[192] Rohrl, J., Hundhausen, M., Emtsev, K. V., Seyller, T., Graupner, R., and Ley, L. Raman spectra of epitaxial graphene on sic(0001). *Appl. Phys. Lett. 92*, 20 (May 2008), 201918–3.

[193] ROSEI, R., DECRESCENZI, M., SETTE, F., QUARESIMA, C., SAVOIA, A., and PERFETTI, P. STRUCTURE OF GRAPHITIC CARBON ON NI(111) - A SURFACE EXTENDED-ENERGY-LOSS FINE-STRUCTURE STUDY. *PHYSICAL REVIEW B 28*, 2 (1983), 1161–1164.

[194] Rotenberg, E., Bostwick, A., Ohta, T., McChesney, J. L., Seyller, T., and Horn, K. Origin of the energy bandgap in epitaxial graphene. *Nat Mater 7*, 4 (Apr. 2008), 258–259.

[195] Rutter, G. M., Crain, J. N., Guisinger, N. P., First, P. N., and Stroscio, J. A. Structural and electronic properties of bilayer epitaxial graphene. *Journal Of Vacuum Science & Technology A 26*, 4 (July 2008), 938–943.

[196] Rutter, G. M., Crain, J. N., Guisinger, N. P., Li, T., First, P. N., and Stroscio, J. A. Scattering and interference in epitaxial graphene. *Science 317* (2007), 219–22.

[197] Rutter, G. M., Guisinger, N. P., Crain, J. N., Jarvis, E. A. A., Stiles, M. D., Li, T., First, P. N., and Stroscio, J. A. Imaging the interface of epitaxial graphene with silicon carbide via scanning tunneling microscopy. *Phys. Rev. B 76* (2007), 235416.

[198] Sharma, N.and Oh, D., Abernathy, H., Sprinkle, M., Berger, C., de Heer, W. A., Liu, M., First, P. N., and Orlando, T. Layer dependent signatures of epitaxial graphene grown on si-terminated 6h-sic(0001). 2009.

[199] Son, Y.-W., Cohen, M. L., and Louie, S. G. Energy gaps in graphene nanoribbons. *Phys. Rev. Lett. 97*, 21 (2006), 216803.

[200] Sproull, W. A new type of apparatus for experiments in secondary electron diffraction. *Review of Scientific Instruments 4*, 4 (Apr 1933), 193–196.

[201] Starke, U., Schardt, J., Bernhardt, J., and Heinz, K. Reconstructed oxide structures stable in air: Silicate monolayers on hexagonal sic surfaces. *JOURNAL OF VACUUM SCIENCE & TECHNOLOGY A-VACUUM SURFACES AND FILMS 17*, 4 (1999), 1688–1692.

[202] Stroscio, J., Feenstra, R., and Fein, A. Electronic-structure of the si(111)2x1 surface by scanning-tunneling microscopy. *Physical Review Letters 57*, 20 (NOV 17 1986), 2579–2582.

[203] Stroscio, J. A., and Celotta, R. J. Controlling the dynamics of a single atom in lateral atom manipulation. *Science 306*, 5694 (Oct. 2004), 242–247.

[204] Stroscio, J. A., and Eigler, D. M. Atomic and molecular manipulation with the scanning tunneling microscope. *Science 254*, 5036 (Nov. 1991), 1319–1326.

[205] Stroscio, J. A., Tavazza, F., Crain, J. N., Celotta, R. J., and Chaka, A. M. Electronically induced atom motion in engineered cocun nanostructures. *Science 313*, 5789 (Aug. 2006), 948–951.

[206] Sutter, P. W., Flege, J.-I., and Sutter, E. A. Epitaxial graphene on ruthenium. *Nat Mater advanced online publication* (Apr. 2008), –.

[207] Tersoff, J., and Hamann, D. Theory and application for the scanning tunneling microscope. *Physical Review Letters 50*, 25 (1983), 1998–2001.

[208] Thomsen, C., and Reich, S. Doable resonant Raman scattering in graphite. *PHYSICAL REVIEW LETTERS 85*, 24 (DEC 11 2000), 5214–5217.

[209] Tunistra, F., and Koenig, J. Raman spectrum of graphite. *Journal of Chemical Physics 53*, 3 (1970).

[210] van Bommel, A. J., Crombeen, J. E., and van Tooren, A. Leed and auger-electron observations of the sic(0001) surface. *Surf. Sci. 48*, 2 (1975), 463–472.

[211] Varchon, F., Feng, R., Hass, J., Li, X., Nguyen, B. N., Naud, C., Mallet, P., Veuillen, J.-Y., Berger, C., Conrad, E. H., and Magaud, L. Electronic structure of epitaxial graphene layers on sic: Effect of the substrate. *Physical Review Letters 99*, 12 (2007), 126805.

[212] Veselago, V. Electrodynamics of Susbstances with Simultaneously Negative Values of Sigma and Mu. *Soviet Physics Uspekhi-USSR 10*, 4 (1968).

[213] Veselago, V. Some remarks regarding electrodynamics of materials with negative refraction. *Appl. Phys. B 81*, 2-3 (2005), 403–407.

[214] Vidano, R., Fischbach, D., Willis, L., and Loehr, T. Observation of raman band shifting with excitation wavelength for carbons and graphites. *Solid State Communications 39*, 2 (1981), 341–344.

[215] Wallace, P. R. The band theory of graphite. *Phys. Rev. 71*, 9 (may 1947), 622–634.

[216] Wang, B., Bocquet, M. L., Marchini, S., Guenther, S., and Wintterlin, J. Chemical origin of a graphene moire overlayer on Ru(0001). *PHYSICAL CHEMISTRY CHEMICAL PHYSICS 10*, 24 (2008), 3530–3534.

[217] Wang, F., Zhang, Y., Tian, C., Girit, C., Zettl, A., Crommie, M., and Shen, Y. R. Gate-variable optical transitions in graphene. *Science* (Mar. 2008), 1152793–.

[218] Wang, Z. F., Li, Q., Su, H., Wang, X., Shi, Q. W., Chen, J., Yang, J., and Hou, J. G. Electronic structure of bilayer graphene: A real-space green's function study. *Physical Review B (Condensed Matter and Materials Physics) 75*, 8 (2007), 085424.

[219] Wehling, T. O., Balatsky, A. V., Katsnelson, M. I., Lichtenstein, A. I., Scharnberg, K., and Wiesendanger, R. Impurity states in graphene. *arXiv:cond-mat/0609503 v1* (20 sep 2006).

[220] Whitman, L. J., Stroscio, J. A., Dragoset, R. A., and Celotta, R. J. Manipulation of adsorbed atoms and creation of new structures on room-temperature surfaces with a scanning tunneling microscope. *Science 251*, 4998 (Mar. 1991), 1206–1210.

[221] Widenkvist, E., Quinlan, R. A., Akthar, S., Rubino, S., Bukhvalov, Q. W., Katsnelson, M. I., Sanyal, B., Eriksson, O., Leifer, K., Grennberg, H., and Jansson, U. Intercalation and Ultrasonic Treatment of Graphite-a New Synthetic Route to Graphene. In *American Vacuum Society* (2008).

[222] Williams, J. M. Some problems with negative refraction. *Phys. Rev. Lett. 87*, 24 (2001), 249703–1.

[223] Wulfhekel, W., Sander, D., Nitsche, S., Dulot, F., Leycuras, A., and Hanbucken, M. Structural reorganisation of vicinal surfaces on 6h-sic(0001) induced by hot hydrogen etching. *Appl. Surf. Sci. 234*, 1-4 (July 2004), 251–255.

[224] Xie, Z. Y., Wei, C. H., Li, L. Y., Yu, Q. M., and Edgar, J. H. Gaseous etching of 6h-sic at relatively low temperatures. *J. Cryst. Growth 217*, 1-2 (July 2000), 115–124.

[225] Yao, Z., Kane, C., and Dekker, C. High-field electrical transport in single-wall carbon nanotubes. *Physical Review Letters 84*, 13 (MAR 27 2000), 2941–2944.

[226] Zhang, Y., Brar, V. W., Wang, F., Girit, C., Yayon, Y., Panlasigui, M., Zettl, A., and Crommie, M. F. Giant phonon-induced conductance in scanning tunnelling spectroscopy of gate-tunable graphene. *Nature Physics 4*, 8 (Aug 2008), 627–630.

[227] Zhang, Y., Tan, Y.-W., Stormer, H. L., and Kim, P. Experimental observation of the quantum hall effect and berry's phase in graphene. *Nature 438*, 7065 (Nov. 2005), 201–204.

[228] Zhou, S. Y., Gweon, G.-H., Fedorov, A. V., First, P. N., de Heer, W. A., Lee, D.-H., Guinea, F., Castro Neto, A. H., and Lanzara, A. Substrate-induced bandgap opening in epitaxial graphene. *Nature Materials 6*, 10 (Oct. 2007), 770–775.

[229] Zhou, S. Y., Gweon, G.-H., Rollings, E., Fedorov, A. V., First, P. N., de Heer, W. A., Castro Neto, A. H., and Lanzara, A. One two three...infinity: From epitaxial graphene to graphite. *preprint* (2006).

VITA

Nikhil Sharma was born to Sneh Prabha and Pradeep Sharma on August 4, 1979 in New Delhi, India. A first-born in his family, he received doting attention from his grandparents, uncles and aunts gathering enormous confidence and a positive attitude in his childhood. The loving and encouraging atmosphere at home nurtured a sense of curiosity, innovation, as well as strong ethics and independent thinking in Nikhil, which later would become handy tools throughout his academic career. Nikhil excelled at both sports and academics, playing cricket and badminton though college and also standing First in the experimental branch in Physics at the Master's level in University of Delhi in 2002. After graduating Magna Cum Laude from the University of Delhi, Nikhil went on to acquire another Master's in Physics at Georgia Tech in fall of 2004. An accomplished actor, singer and artist, Nikhil met his intellectual match and soul mate, Malika Sachdeva while performing a lead theatrical role in Atlanta, Georgia in May 2004. In July 2005, Nikhil married Malika in a traditional Indian ceremony in Delhi with his friends and family, and in January 2008, they wre blessed with a son, Shaurya Kartikaye. Nikhil continued to pursue his his Ph.D under the guidance of Dr. Phillip N. First at the School of Physics between 2004 and 2008. For his doctoate work, Nikhil worked with growth and characterization of Epitaxial Graphene exploring it as a potential substitute for the aging silicon based technology. After graduating in 2009, Nikhil will join Intel Corp. at Hillsboro, Oregon as a Process Technology Development (PTD) Engineer.